A Thesis for the Degree of Ph.D. in Engineering

Fabrication of Paper-Based Analytical Devices by Chemometrical Approach

August 2018

Graduate School of Science and Technology

Keio University

HAMEDPOUR, Vahid

Table of Contents

Chapter 1 General introduction to paper-based analytical devices and chemometrics

1.1. History of paper-based analytical devices

The oldest application of paper as a platform was investigated by the Roman natural philosopher Pliny the Elder which demonstrates a spot test for iron (II) sulfate on papyrus sheet and a procedure, similar to modern paper chromatography, for evaluation of Tyrian purple dye's quality [1]. The second application was performed by the Irish chemist Robert Boyle in 1664 [2]. In this work, the water-soluble mixture of litmus was absorbed onto the filter paper, and a colorimetric pH indicator for checking the acidity or alkalinity of the solutions was fabricated (Fig. 1-1). In spite of the simplicity of this device, it is still commonly used in rapid pH tests and experimental science classes.

Figure 1-1. The colorimetric behavior of pH indicators in different conditions.

In 1850, a simple strip for diagnosis of urinary sugar based on absorption of stannous chloride solution onto the sheep's wool was proposed by the French chemist Edme-Jules Maumené [3]. Then, the Italian chemist Hugo Schiff developed a spot test for uric acid which addition of uric acid on a paper containing silver carbonate leads to a gray precipitate [4]. In 1883, the first marketed room temperature stable paper-based device for the diagnosis of urinary glucose and protein was fabricated by the English physiologist George Oliver [5]. Since the 20th century, application of paper as a substrate gained more attention, and the number of reports started to increase. For example, in 1906, Janos Plesch described a chromatography-based spot test for urinary bilirubin, and in 1937, Yagoda presented a colorimetric spot test sensor for detection of metal ions (Cu^{2+} and Ni^{2+}) which was patterned by paraffin embossing (Fig. 1-2) [6].

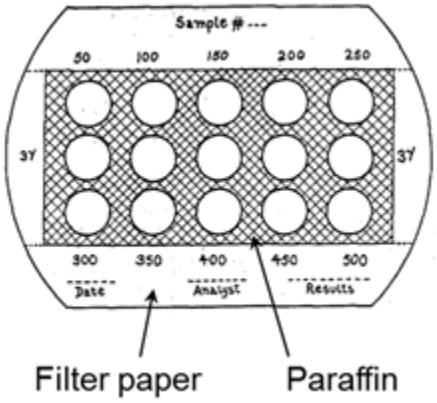

Figure 1-2. Fabricated spot test sensor for detection of Cu^{2+} and Ni^{2+}. Adapted with permission from Ref [6]. Copyright 1937American Chemical Society.

The culmination of this process was in 1952 where the Nobel Prize in Chemistry was awarded to the Richard Laurence Millington Synge and Archer John Porter Martin because of the invention of paper chromatography [7]. First, this technique was employed to separate some organic compounds including lipids, carbohydrates, and amino acids but later, it was utilized for inorganic substances such as cations and anions as well [8]. The possibility of proteins separation by paper chromatography caused endeavor to apply this method for separation of

peptides and amino acids, but it led to unsuccessful results. This problem was overcome by the development of paper-electrophoresis, and nowadays, it is known as a useful tool in the separation of proteins [9].

After this, the paper substrate became more common than before, and several interesting reports were published. The following works are some examples of reported researches. For instance, in 1956, A. Keston developed a paper-based colorimetric glucose assay using an enzymatic reaction, or in 1957, J. Kohn applied the previously reported urinary glucose device for blood samples [9].

Reported progresses encouraged companies to invest in this field, and in this regard, Ames Company introduced a commercialized portable reflectance meter in 1964 and "Dextrostix" as an enzymatic dipstick for blood glucose in 1970 [10]. After a while, in 1988, the first commercialized pregnancy kit for detection of human chorionic gonadotropin was brought to the market by Unipath Ltd samples [11].

As mentioned before, paper as a substrate has assisted chemists for centuries in various forms, but in 2007, paper as a modern and valuable platform was rediscovered by George Whitesides's group [12]. This report demonstrates a patterned paper-platform with multiple channels enabling quantification of total protein concentration and glucose in artificial urine sample. After this report, scientists have invested time in fabrication of low-cost user-friendly paper-based analytical devices (PADs). Fig. 1-3 demonstrates a great breakthrough in application of PADs in various fields such as diagnostic tests, food safety control, drug analysis, cell assay, and environment monitoring.

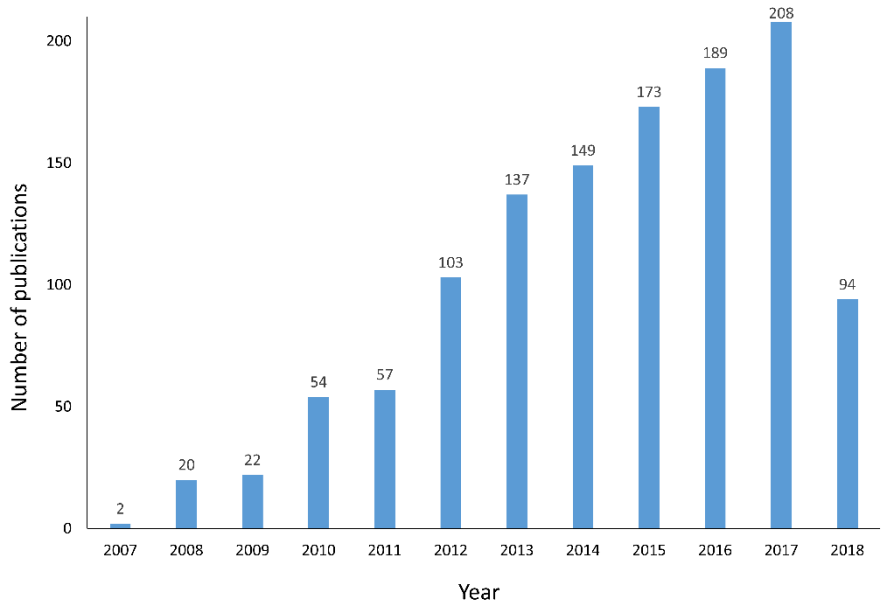

Figure 1-3. Breakthrough in fabrication of PADs (analyzed by citation number of Whitesides report [12] on the Web of Science^{TM} on June 10, 2018).

1.2. Structure and composition of paper

Cellulose fibers with a hierarchical structure are the dominant component of paper. Cellulose is known as the most abundant biopolymer in the world. A huge amount of β-glucose elements construct chains with the maximum length of 5 μm. These chains by forming hydrogen bonds between hydroxyl groups can sustain together. Partially crystallized chains organized into microfibrils and microfibrils form fibrils. Depending on the origin of fibrils, they can have an approximate length ranged between 2–5 mm and the width varies from 20 to 40 μm. The amorphous parts among fibrils mostly contain lignin, a three-dimensional hydrophobic polymer, and hemicellulose, a hydrophilic carbohydrate polymer (Fig. 1-4) [13, 14].

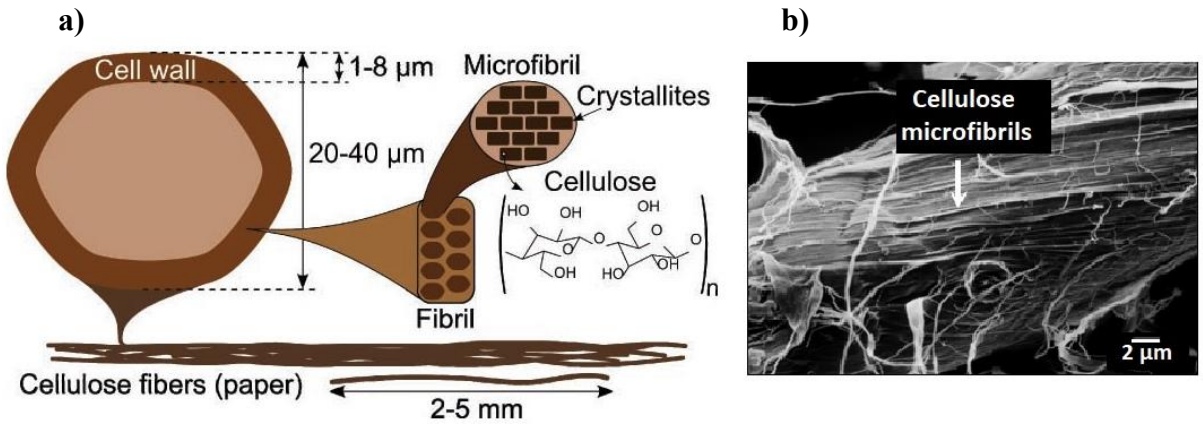

Figure 1-4. a) A graphical representation of cellulose fibers in paper, demonstrating the length ranged between 2–5 mm and width 20–40 µm relying on the origin. The cellulose cell wall contains fibrils, and fibrils are made of microfibrils with a diameter ranged between 3–20 nm. The amorphous substance of cellulose fibrils mostly consists of lignin and hemicellulose, and the microfibrils contain cellulose chains that form crystalline parts of cellulose and are sustain together by hydrogen bonds. Adapted with permission from Ref [14]. Copyright© 2011 WILEY-VCH Verlag GmbH & Co. KGaA, Weinheim, and b) representative scanning electron microscopy (SEM) image showing exposed cellulose microfibrils. Adapted from Ref [15].

Features of paper such as fiber length and content of hemicellulose and lignin rely on the type of plant and alga and pulping techniques. In all cases, cellulose pulp is the main raw material but the preparation method, which can be a mechanical or chemical process, can result in different products. In mechanical pulping, logs were forced against water lubricated revolving stone, which grinds the logs into pulp by abrasive action. The resulted paper in this method has shorter cellulose fibers with lower porosity. This type of pulp also consists of hemicellulose and lignin which is causing paper aging (fragile and yellowing), and also pitch (fatty acids and resin) [16, 17]. In chemical pulp preparation, fibers are separated after decomposition of lignin through pH value. This procedure leads to partial removal of lignin, longer cellulose fibers, and highly hygroscopic paper. Compared to previous techniques, bacterial cellulose is less popular, and it results in products free of hemicellulose and lignin, higher crystallinity, molecular weight, and mechanical strength [16].

In order to fabricate papers, additives and diluted pulp are mixed in an appropriate ratio, and the prepared solution is filtered before appliction. The most common additives are mineral compounds like calcium carbonate that not only raises the brightness but also decreases the

cost and roughness of the paper. Additives may consist maximum 30% of the product but some of them, such as calcium carbonate with buffering ability, may affect the efficiency of the fabricated paper device [17, 18]. Therefore, in some cases, a chemical modification process including carboxymethylation or acetylation, and polymeric treatment such as polyvinyl acetate, cellulose acetate, carboxymethyl cellulose, and starch are used to intensify the mechanical strength of paper. Other frequently used compounds are dyes, brighteners, pH controllers and adhesives. Hence, physical and chemical features of papers can differ based on the type of production method and applied additives [14, 17].

Papers along the z-axis, indicating the thickness of the product, show non-uniform mass distribution. Therefore, central parts of most of the papers are thicker and less compact than the other sections. The swelling rate in each direction also shows different behavior. For example, if the paper subjected to humidity, it can show only up to 1 % rise in the longitudinal axis and maximum 20 % increase in z-axis [14]. Based on the paper production and cutting procedures, fibers direction and as a result sample transportation can be easily affected [17]. Due to this reason, sometimes irregular wicking rates can be seen within a paper sheet.

1.3. Paper as an experimental platform

As mentioned before, application of paper as a substrate has a long history in analytical chemistry and is not a new application in this field. PADs benefiting from the inherent features of paper such as lightweight, portable, low-cost, safely disposable, and flexibility (ability of bending and constructing 3D structures), and potential properties including low sample and reagents consumption, simple fabrication, easy usage, ability to use in remote locations, pump-free (because of capillary effect), and providing rapid detection without requirement of trained personnel. Therefore, they have a great potential to be utilized as convenient devices for

biological, clinical, chemical and environmental analysis in inaccessible areas or undeveloped countries [19].

In spite of mentioned advantages, paper also has some disadvantages. For instance, the chemical composition of papers may vary even if they provided from same the supplier or impurities in paper with higher absorbing capacity may remain, even after performing several elimination steps [20]. Phosphorescent residues can cause high background noises in some cases, therefore storing at a specific temperature (37°C) [21] or subjecting to polychromatic UV light irradiation [20] can prevent such problems. Steadiness of the response is also one of the challenges ahead. For example, liquid sample can be easily washed and moved the non-immobilized sensing molecules toward the edges of the sensing area. This phenomenon can affect the uniformity of the obtained signal. For overcoming these problem, various pretreatment methods by utilizing of polymers such as poly(ethylene glycol) [22], poly(acrylic acid), gelatin [23], and poly(vinylamine) [24] has been reported.

The other feature is that structure of paper which can be easily changed by the heating. Thus, for microfabrication systems which require high temperature (over 200°C), paper is not a suitable substrate because ignition point of paper is around 200°C. Effect of the humidity on paper thickness is another point that should be paid attention since it can reduce the tensile strength of paper. Assay reagents deposition step or paper storing condition are the origins of this problem and can be easily avoided [14, 25–28].

Table 1-1 represents a comparison between features of common substrates such as glass, silicon, polydimethylsiloxane (PDMS), and paper.

Table 1-1. Comparison of paper with other substrates. Adapted with permission from [4]. Copyright© 2013, Springer.

Features	Paper	PDMS*	Silicon	Glass
Initial investment	Low	Moderate	High	Moderate
Price	Low	Moderate	High	Moderate
Uniformity of the substance	No	Yes	Yes	Yes
Spatial resolution	Low to moderate	High	Very high	High
Functionalization	Easy	Difficult	Moderate	Difficult
High-throughput fabrication	Yes	No	Yes	Yes
Biodegradability	Yes	To some extent	No	No
Disposability	Yes	No	No	No
Biocompatibility	Yes	Yes	Yes	Yes
Sensitivity to humidity	Yes	No	No	No
Fluid flow	Capillary action	Forced	Forced	Forced
Surface-to-volume ratio	High	Low	Low	Low
Structure	Fibrous	Solid, gas, permeable	Solid	Solid
Flexibility	Yes	Yes	No	No
Surface profile	Moderate	Very low	Very low	Very low

*Polydimethylsiloxane

Each substance as a platform has its specific benefits and deficiencies. Paper in comparison with other substrates (0.1 cents/dm^2) is 1000 times than glass and 200 times than PET (polyethylene terephthalate) cheaper and abundantly available [14, 29]. Besides the lower price of the paper, the fabrication process of paper-based devices is also not costly. Therefore, a moderate investment can lead to sensitive prototype devices with the ability of practical application in real-life [30, 31].

1.4. Fabricating techniques

The selection of fabrication method mainly depends on the price, application and desired resolution. Depending on the type of the PAD (2D or 3D), several fabrication techniques have been developed (Fig. 1-5). Type of the PADs mainly depends on fluid transportation direction, vertical and/or horizontal dimensions, and complexity of the diagnostic application [32].

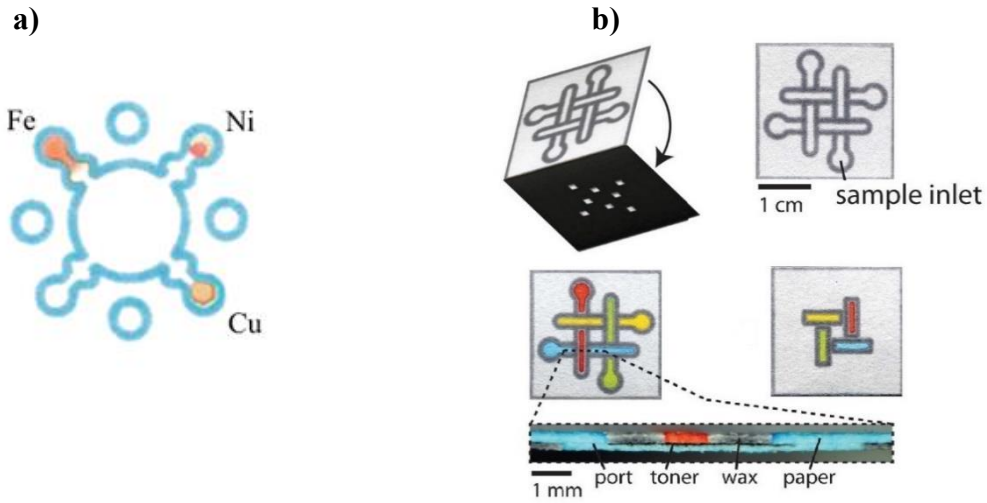

Figure 1-5. a) A 2D device as a platform for multianalyte detection [22], and b) a 3D-PAD with multichannel feasibility (ports in the toner layer allow samples to flow between adjacent layers of paper. The toner also fixes the paper layers together and avoids interfering of the solutions in adjacent channels) [33]. Adapted with permission from [22] Copyright 2012 American Chemical Society, and [33] with permission from The Royal Society of Chemistry.

Most common fabrication methods such as laser treatment [34], plasma treatment [35], flexographic printing [36], wax printing [37,38], plotting [39], photolithography [40,41], inkjet printing [42], wax screen printing [43], and wax dipping [44,45] have been reported for fabrication of PADs [25]. Table 1-2 demonstrates a brief comparison of reported techniques. These techniques can be applied to change the hydrophilic property of specific sections of paper to hydrophobic. Therefore, the remained hydrophilic spaces act as a channel, and due to capillary effect, aqueous solution flows through the channel and not able to penetrate the hydrophobic barrier. In the following sections, two popular techniques including wax printing and inkjet printing techniques will be briefly described.

Table 1-2. Comparison of common patterning methods. Adapted with permission from Ref [33]. Rights-managed by Taylor & Francis.

Fabrication technique	Equipment	Advantage	Disadvantage	Ref.
Plasma treatment	Heating equipment, inkjet printer,	Printing of various patterns and functional compounds	Time-consuming (> 45 min), uses volatile organic compounds	[35]
Laser printing	Heating equipment, laser printer	Fabrication of multiple devices on a single sheet	Requires heating equipment	[34]
Flexography	Flexographic press	High throughput (60 m min^{-1})	Uses volatile organic solvent; requires two printing cycles	[36]
Wax printing	Heating equipment, wax printer	Hydrophilic section not subjected to solvents and polymers; quick (< 5 min)	Requires heating equipment	[37, 38]
Plotting	Customized plotter	Hydrophilic section not subjected to solvents and polymers	Uses volatile organic solvent; requires a modified plotter	[39]
Photolithography	Heating equipment, UV light source	High resolution of the created pattern	Hydrophilic section subjected to solvents and polymers; uses volatile organic solvent; high cost of photoresist	[40, 41]
Inkjet printing	UV light source, inkjet printer	Hydrophilic section not subjected to solvents and polymers; applicable to assay reagent deposition	Requires intense UV irradiation	[42]
Screen printing	Heating equipment wax printer,	Simple and low-cost process, suitable for bulk production	Each pattern requires an individual screen, low resolution	[43]
Wax dipping	Melted wax, iron mold, heating equipment	Rapid (< 1 min), low-cost, simple and reproducible, suitable for bulk production	Low resolution, requires heating equipment	[44, 45]

1.4.1. Wax printing

This technique is mostly used for patterning the substrate. Utilization of this technology for patterning of PADs has some advantages, e.g. ease of fabrication (printing and baking), non-toxicity (organic solvents not required), disposability (wax and paper can be burnt), lower cost (both paper and wax are inexpensive and easily accessible), rapid (5-10 min), and few steps are needed for mass production. Hence, the wax printing technology is a convenient way for patterning PADs and developing of inexpensive bioassays for out of access locations [38].

Fig. 1-6 shows the patterning process of the nitrocellulose by wax printing technique [46]. For this purpose, after preparation of appropriate patterns on the computer, they are printed on the nitrocellulose membrane. Since these wax barriers are only on the surface of the substrate and have not penetrated till the bottom of the membrane, therefore a further step, heating or baking, is required. Heating process (typically 2-5 min at 100 - 150°C) allows the wax to melt and diffuse till bottom of paper substrate and therefore hydrophobic barriers are created. The specific properties of nitrocellulose, like uniform and small pore size, causes slow, controllable and precise wax penetration process during the baking step. Compared to photolithography technique, this method does not require any harmful organic solvents and enables the creation of microchannels with a width of 100 μm.

Up to date, three methods such as I) pattern printing by a wax-printer, II) painting with a wax pen, III) deposition of wax by an office inkjet-printer and tracing by painting with a wax pen, have been utilized as wax patterning technique [37]. This technique is rapid and easy to operate and does not require UV lamp, clean room, or additional equipment.

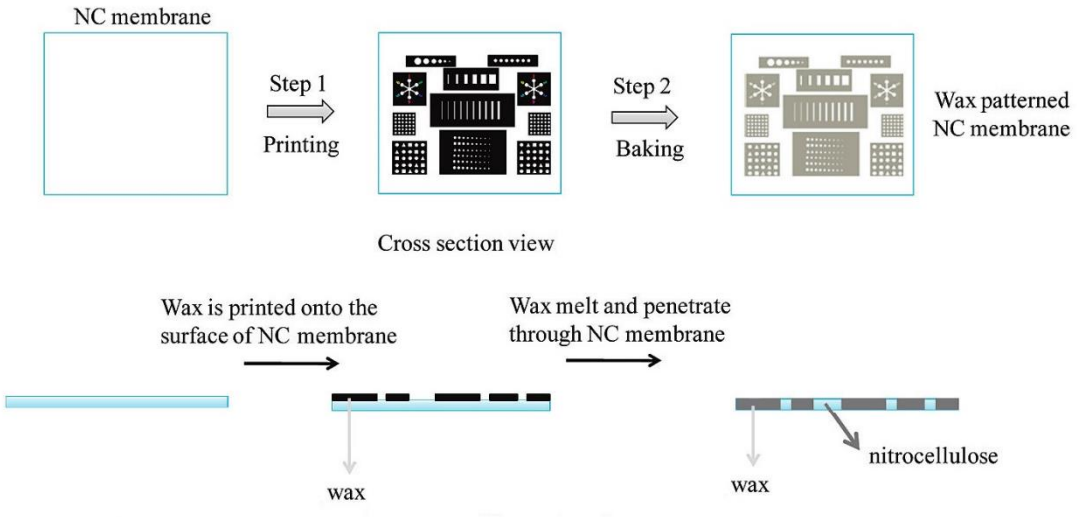

Figure 1-6. Graphically representation of patterning of nitrocellulose (NC) membrane by wax printing. This process includes two steps: printing the wax pattern onto the surface of the NC; and baking (5 min in an oven with a temperature of 125°C) for letting the wax to melt and diffuse till the bottom of the substrate. Adapted with permission from Ref [46] Copyright 2010 American Chemical Society.

1.4.2. Inkjet-printing

1.4.2.1. Patterning by inkjet-printing

This technique is a new way of patterning of paper substrate, and it combines the inkjet printing technology with paper sizing chemistry [47]. This procedure can be applied in two ways: I) in first approach, paper is entirely soaked in a hydrophobic solution such as polystyrene, then dried paper exposed to inkjet printing of organic solvent (toluene). In this way, channels can be created by washing the hydrophobic solution. This method is known as inkjet Etching [48], II) in the second method, a UV-curable ink, which is a pre-polymer, is printed to the paper, then by using UV light polymerization within the cellulose network starts and hydrophobic barrier forms. This method is called direct inkjet printing of hydrophobic barrier [42]. Patterning by inkjet printing can be used in bulk production because of lower cost and higher volume and speed [49].

1.4.2.2. Deposition of assay reagent by inkjet printing

Inkjet printers not only can be utilized for substrate patterning but also be employed for deposition of assay reagents. Although manual pipetting can be performed for deposition of the assay reagents, it cannot be a good option for bulk production because of poor reproducibility, high amount of labor and limiting the production volume to several million tests per year [50]. Compared to manual deposition method, inkjet printing technique is automated and flexible, and these user-friendly features make it widely used.

General classification of types of printers including continuous inkjet (CIJ) and drop-on-demand (DOD), and their properties have been already described in several reports [51]. Among the utilized printers, two types of drop-on-demand inkjet printers consisting thermal and piezoelectric types are routinely employed. Thermal inkjet printers are suitable for deposition of solutions with a viscosity in the range 1-5 cP, and piezoelectric types are suitable for solutions with viscosity ranged from 5 to 50 cP. In the latter type, to change the viscosity of the solution, some modifying agents such as ethylene glycol or glycerol has to be used. It is worth mentioning that the nozzle orifice diameter should be one hundred times bigger than the particle size of the solution; otherwise, they cannot be printed [52].

The three common analytical assays including classical color indicators, immunoassay techniques, and enzyme assay methods have been benefited from inkjet printing method. Hence, this deposition technique can be applied to print the required reagents for optical signal detection in ultra-small volumes with accurate, reproducible, and high-resolution liquid placement [51]. A schematic illustration of assay reagents deposition by inkjet printing technique is shown in Fig. 1-7.

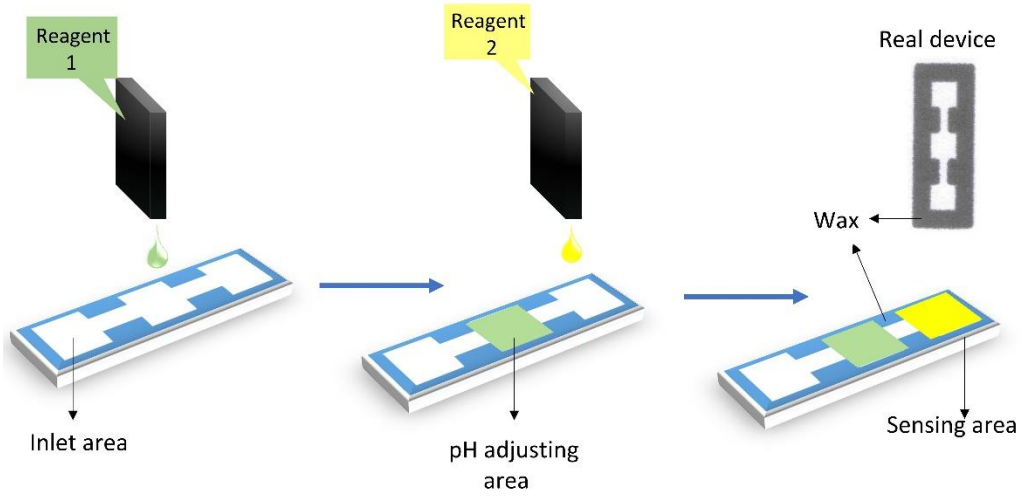

Figure 1-7. Schematic representation of assay reagents deposition by inkjet printing technique. The blue area represents the wax barrier.

1.5. Detection methods

Until now, several detection methods have been reported, and in general, sensing assays can be classified into two main groups including colorimetric or electrochemical assay methods. The colorimetric techniques consist of redox indicators, nanoparticles-based assays, chemiluminescent, and fluorescent [53], and electrochemical methods include amperometry, voltammetry, potentiometry, and electrochemical impedance spectroscopy [54]. Fig. 1-8 represents percentages of various methods such as electrochemistry (EC), chemiluminescence (CL), electrochemiluminescence (ECL), colorimetry, and fluorescence in fabrication of PADs.

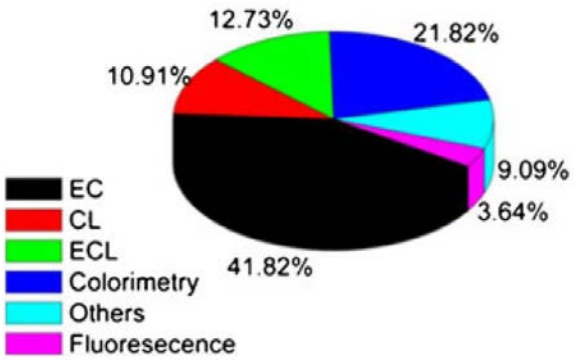

Figure 1-8. Percentage of each detection technique in fabrication of PADs. Adapted with permission from [55]. Copyright© 2016, Springer.

Colorimetric assays are the most commonly utilized method in both academic studies and industrial projects [56]. In the case of combing redox indicators with PADs, the utilized indicator should include some features such as I) showing significant color change between reduced and oxidized form, II) having a suitable color change based on the targets concentration, III) having a stable color during the analysis, and IV) having lower or no toxicity. Since finding an indicator consisting all of the mentioned features is difficult [53], thus other alternative colorimetric approaches like nanoparticle-based assay can be utilized. Metal nanostructures, particularly gold and silver nanoparticles, have unique and favorable properties, such as the unique optical behavior used in localized surface plasmon resonance (LSPR) [57,58]. The particular wavelength of the LSPR depends on size, shape, and agglomeration state of the nanoparticles [59]. Therefore, in this detection method if the presence of the analyte can cause a change in the aggregation state of the nanoparticles, color change will occur. In this regard, the easiest way to take advantages of nanoparticles is the in-situ formation on the paper substrate. In this approach, instead of beforehand synthesizing of the nanoparticles, they are formed on the substrate. Therefore, a long process of synthesizing can be avoided, and due to acceleration in the device fabrication process, it is suitable for mass production [60, 61] (Fig. 1-9).

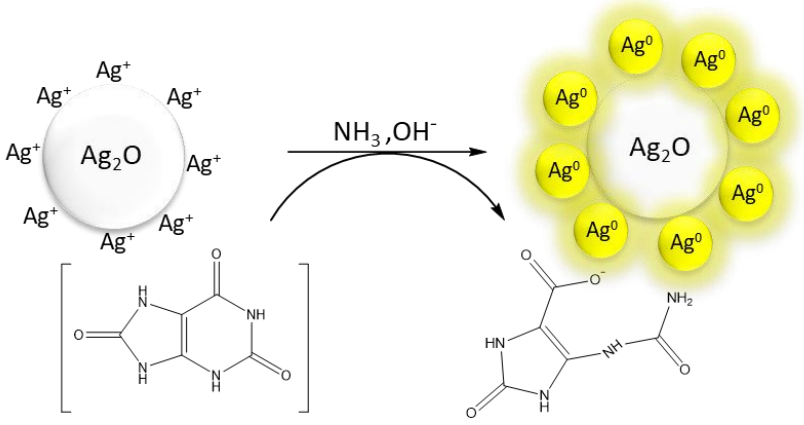

Figure 1-9. Schematic illustration of in-situ formation of silver nanoparticles after addition of uric acid to the mixture solution of $AgNO_3$, NH_3, and polyvinylalcohol.

Although the colorimetric technique has some shortcomings such as low selectivity, low sensitivity, and in some cases releasing toxic gases during operation [62], it is still promising and has great potential for improvement in near future. In chapter 3 and 4 of this thesis, the benefit of inkjet-printer as a powerful tool for precise deposition of assay reagents onto paper structure was demonstrated.

Till this section, all the required steps for fabrication of a paper-based device have been described. In the following sections, the potential of chemometrics for emboldening the fabrication of PADs will be discussed.

1.6. Chemometrics

The notation chemometrics in analytical chemistry was introduced in 1972 by the Svante Wold and Bruce R. Kowalski. In this definition, chemometrics is the application of mathematical and statistical methods to improve the understanding of chemical information. In other words, this discipline provides maximum information from a chemical system by data processing. In general, chemometrics can be considered as a wider field "chemoinformatics" which has been defined as the utilization of informatic techniques to solve the chemical problems including DoE, data analysis & mining, digital image processing (DIP) and programming skill [63].

Till now, although in several reports high-content and high-throughput (bio)chemical assays have been demonstrated, their wholesale application in point-of-care diagnosis has been slow. This problem originates from regulatory obstacles, analytical property concerns, problems with biological samples, lag in microfluidic technology, economics, and lack of chemometrical approaches [64].

Despite the necessity of using this approach in device development, only a few cases have been utilized it. This approach has the potential to cover all aspects of PADs development, e.g. DoE

can investigate the impact of all factors on the response intensity [60, 64], data analysis can be employed in data classification [65–68], and signal processing can be useful for extracting further information or improvement of the obtained data [60, 68, 69]. Fig. 1-10 represents the applicable chemomerical techniques in the development of PADs from device optimization to signal readout.

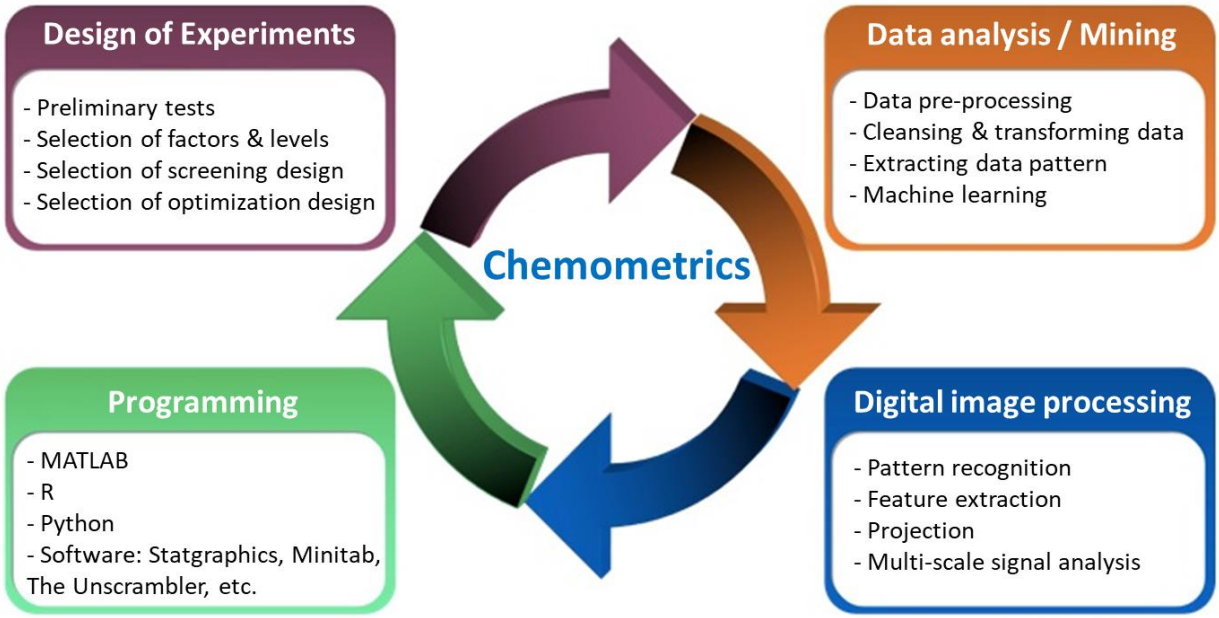

Figure 1-10. Applicable chemometrical techniques in the development of PADs.

1.6.1. Design of Experiments (DoE)

1.6.1.1. Brief history of statistical design

The first report of design of experiments (DoE) backs to a systematic clinical trial for comparing of remedies for scurvy which was carried out by the Scottish physician James Lind in 1747 [70]. In that study, Lind selected 12 men and divided them into six pairs. Then, he gave different diet to each pair for two weeks, and in this way, he could study the effect of food diet on the treatment of scurvy. The first theory of statistical inference “Illustrations of the logic of

science," which mainly emphasized on the importance of randomization-based inference in statistics, was reported by Charles S. Peirce in 1877-1878 [71].

The modern development of statistical experimental design can be classified into four eras including agricultural era, first industrial era, second industrial era, and modern era. The first era (1918–1940s), which is called agricultural era, was pioneered by a work of the British statistician and geneticist Sir Ronald Aylmer Fisher in 1918 [72]. During that time, Fisher was working in Rothamsted Agricultural Experimental Station (London, England) as a statistician and data analyst. Fisher methodically introduced the basics of statistical concepts consisting of analysis of variance (ANOVA) and factorial design into DoE. Although the application of statistical design in chemical processes began in the 1930s, during the second era (1951–late 1970s), which is known as first industrial era, the application of DoE attracted more attention. In 1951, introduction of response surface methodology (RSM) by George Edward Pelham Box and Kevin B. Wilson accelerated the procedure. They noticed that most industrial experiments are basically different from agricultural projects in two ways: I) in most of the cases, the response can be obtained immediately (immediacy factor), and II) vital and initial information can be extracted from a limited number of experiments which can be useful in planning of the following runs (sequentiality factor). Box can be counted as the intellectual leader of the move toward the application of RSM and other techniques in research and development works [73]. The third era (late 1970s–1990) or second industrial era was the result of attracting attention to quality improvement of Western industries in the late 1970s. The work of Genichi Taguchi had a remarkable effect on expending usage of DoE. One of the positive outcomes of the Taguchi's attitude to industrialized DoE was the nascent fourth era (beginning circa 1990) or the modern era. This era has consisted revived interests in DoE and the evolution of applicable approaches to experimental difficulties in the industrial projects. Therefore, the modern generation can be an appropriate alternative to Taguchi design that enables his theory to be performed effectively

and efficiently in practice [73].

In spite of the long history of this approach, the application of statistical design at industrial and educational projects is still not extremely common. This is because of inadequate knowledge in fundamental of statistical concept and methods. Fig. 1-11 demonstrates the application of DoE in whole chemistry disciplines. It is worth mentioning that according to the Web of Science™ database, only 3.32% of the analytical chemistry reports (total number of 54,634 reports in 2017) were employed DoE methodology in their optimization process.

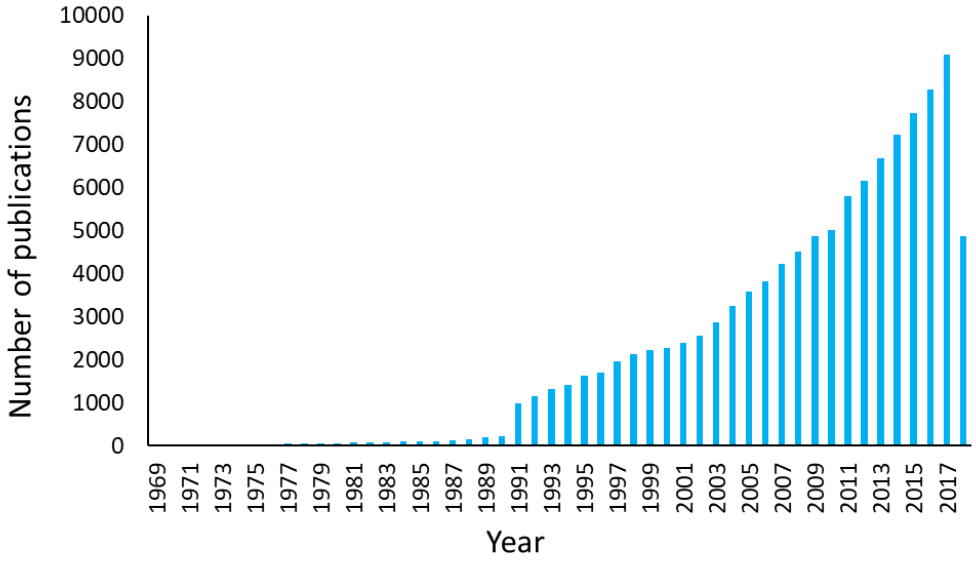

Figure 1-11. Applicable of DoE in whole chemistry disciplines (searched on the Web of Science™ on June 10, 2018).

1.6.1.2. Necessity of DoE

Since in most practical cases, several parameters can simultaneously affect the competent result, therefore recognition and optimization of effective factors are the most important part of the work. For this purpose, DoE approach is mainly applied to obtain the optimum experimental condition because it provides maximum information of the system with a lower required amount of time, resources, and materials. It has been proved that PADs highly depend on the

device geometry, variation, and type of factors [60, 64]. Thus, optimization step plays an important role in the development and commercialization of the device performance.

Over the last years, all the attention focused on developing sensing mechanisms [62], patterning and assay reagent deposition techniques [32, 51], response signal interpretation methods [74], investigation of impact of printing techniques (ink heating or shear force) on the assay reagent's properties [75–77], ejectable liquid volume from cartridges [78] and types of filter paper, but DoE approach is often disregarded. Although in some reports the importance of the device geometry was partially investigated, the investigation of all probable factors has not been done [60]. For example, by one-factor-at-time approach, the effect of the channel length and width [79], and device shape [53], and by a simplified DoE approach for optimization of some effective factors have been reported but sill the DoE needs to be paid more attention. A workflow and involved steps in the DoE approach is shown in Fig. 1-12.

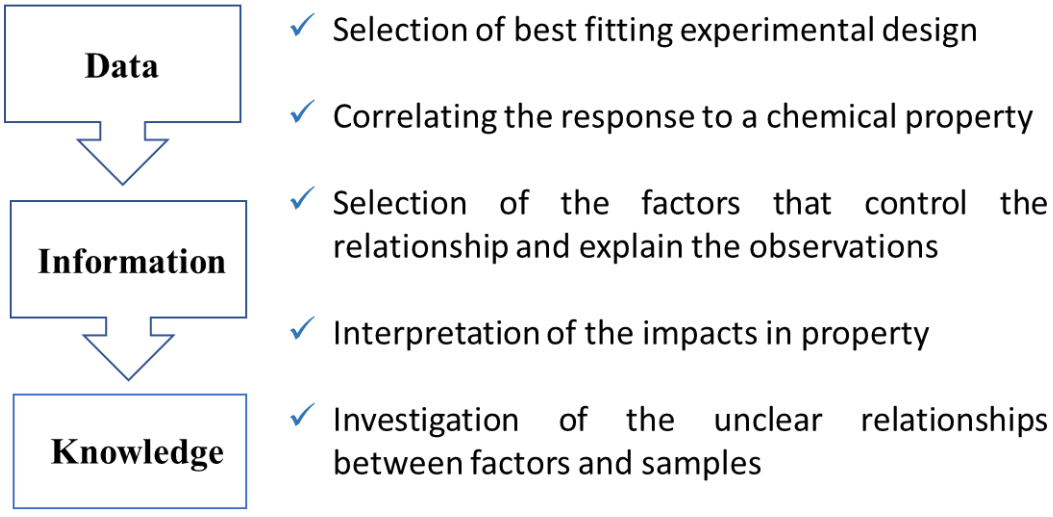

Figure 1-12. Workflow and involved steps in a DoE approach.

1.6.1.3. Terminology of design of experiments

Since the origin of the DoE traces back to operations research and sociological, the commonly used terminologies are not understandable for chemists. The following denotations are adapted from International Vocabulary of Metrology (VIM), and explained in a chemistry viewpoint [80]:

- **Design of experiments (DoE)**: a statistical approach for analyzing, conducting, planning, and extracting data from a limited number of experiments.
- **Response**: an observed or measured parameter that is the main goal in the optimization process. For example, color intensity value in colorimetric-based PADs and retention time in HPLC are some of the common examples.
- **Factor (also known as parameter, variable, and predictor)**: parameters that can affect the response are counted as factors. Depending on the levels of factors, the factors can be controlled or uncontrolled type. Therefore, randomization is the most reliable way to create homogeneous treatment groups, without involving any potential biases, and minimizes the impacts of uncontrollable factors on the response. Factors can be continuous or discrete values, e.g. catalyzer type (A or B) is a discrete value, and concentration is a continuous value.
- **Level**: values of a factor which are defined in the DoE process. Number of the levels are mainly used in the description of designs such as three-level factorial design. This terminology shows that the effective factors have three levels per factor. For example, box length: 2, 4, 6 mm; box width: 5, 7, 9 mm; and sampling volume: 10, 12, 18 µL.
- **Response surface**: a two or three-dimensional plot showing the predicted response for any combination of the two factors under examination (all the other factors being kept at a constant predefined level) [81].
- **Model**: a mathematical equation which correlates factors (independent variables) to a response. This equation can be based on experimental data (empirical) or theoretical estimation

of factors impact performance (theoretical). Each model consists of several terms, and the terms are given in order, e.g., first order, second order. The following equations are examples which displaying the relationship between a response and factors:

$$Y= b_0 + b_1X_1 + b_2X_2 \quad \text{Eq. 1-1}$$

$$Y= b_0 + b_1X_1 + b_2X_2 + b_{12}X_1X_2 \quad \text{Eq. 1-2}$$

$$Y= b_0 + b_1X_1 + b_2X_2 + b_{12}X_1X_2 + b_{11}X_1^2 + b_{22}X_2^2 \quad \text{Eq. 1-3}$$

where, Y demonstrates the response, b_0 is the intercept, b_1, and b_2 are first-order coefficients, b_{12} is an interaction coefficient, b_{11} and b_{22} are second-order coefficients (quadratic terms), and X_1 and X_2 are the effective factors, respectively. Coefficients can be calculated by multiple linear regression analysis. Factors in equations 1-1 and 1-2 are linear, and their 3D response plots are a flat and a twisted plane, respectively. Equation 1-3 shows a second-order model which represents a twisted surface with curvature, originating from the quadratic terms [82]. 3D response surface plots are the contribution of two factors and facilitate understanding of the main and interaction effects. Furthermore, these plots can be useful in the investigation of the experimental factors impacts on the response [83]. The contour plots demonstrate the sections of the response surface.

- **Coded levels:** matrix of each design is often written in the coded levels. For instance, a two-level design is coded a series of +1 and −1 indicating +1 for the higher and −1 for the lower level. In this way, design can be prepared independent of the individual factors.

1.6.1.4. Advantages over one-factor-at-time

It has been proven that in the optimization of a response, a DoE methodology is superior to the traditional one-factor-at-time (OFAT) method. One of the incentives for analysts is that if the interactions among factors are discarded, changing one factor at a time can cause an inaccurate

optimal condition. For instance, if a system is influenced by both temperature (T) and pH, by keeping first the pH fixed and changing the temperature, then using this optimum temperature and change the pH, may not lead to the optima. The reason is that the pH-dependent behavior varies according to temperature and they cannot be investigated separately. Fig. 1-13a demonstrates the OFAT approach which does not lead to the true optimal condition. Nevertheless, in the case of DoE methodology, the interactions are included, and experimental space is covered by design (Fig. 1-13b). Additionally, the obtained information about the system will be more than the OFAT methodology [80]. Compared to the other techniques like Simplex, in DoE, the required number of experiments can be determined in advance. Therefore, the required time for the whole experimental process can be estimated.

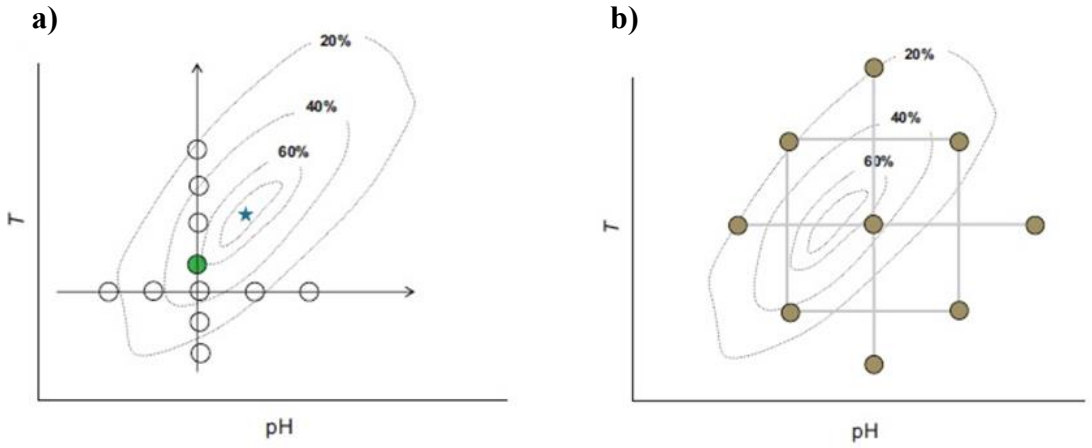

Figure 1-13. a) One-factor-at-time approach with the selected best condition (green point) and accurate point (star) on a theoretical response surface, and b) a DoE approach (central composite design) for the same condition. As can be seen, DoE requires less number of the experiments than OFAT approach and able to cover whole experimental space with better prediction of the optimal condition. Adapted from Ref [80] Copyright 2012, with permission from Elsevier.

In conclusion, DoE has several benefits over OFAT approach. Some examples of these advantages are: I) multivariate methodology supplies overall information inside the experimental domain while univariate approach provides local information where experiments are conducted; II) the study of interactions and quadratic effects is possible, III) required number of experiments are considerably smaller than univariate case; and IV) quality of the

information inside the experimental domain are higher and can be assessed before conducting the experiments by means of the leverage [84].

1.6.1.5. Types of DoE

1.6.1.5.1. Screening

If the response is influenced by a large number of the factors, a screening step is required for elimination of non-significant factors. Screening is an important part of complex systems such as chromatographic methods. The aim of screening is the investigation of the effective factors and their interactions, along with an investigation on their levels. This step is useful in the examination of quantitative, qualitative and mixer-related factors concurrently [85]. The most commonly used screening designs are Plackett-Burman designs (PBD), Full Factorial designs (FFD), and Fractional Factorial designs (FrFD) [86–88] because they are cost-effective and efficient. Regression analysis or analysis of variance (ANOVA) is utilized for computing the impact of each factor (coefficient) on the response. These techniques are regularly used for the study of robustness (small changes introduced deliberately) [89] and ruggedness (different normal conditions) [90]. Comparison of screening designs are summarized in Table 1-3.

Table 1-3. Comparison of common screening designs. Adapted from Ref [91] Copyright 2014, with permission from Elsevier.

Design	Type of factors	Number of factors	Number of required experiments
Plackett–Burman	Numerical Categorical	$N - 1$	N (multiple of 4)
Two-level full factorial	Numerical Categorical	$2 \leq k^* \leq 5$	2^k
Two-level fractional factorial	Numerical Categorical	> 4	2^{k-p}

*k is the number of the factors and p is the number for reduction of full design.

1.6.1.5.1.1. Plackett-Burman design (PBD)

This design was reported by Plackett and Burman in 1946 [92]. A PBD can investigate $N-1$ factors ($k \leq N-1$) with N experiments, which N should be a multiple of 4 up to 36. For instance, systems with 7 and 11 factors need 8 and 12 runs, respectively. Since the required number of experiments in PBD is small, thus the linear terms and two-factor interactions are heavily confounded and cannot be distinguished. Hence, PBD is only suitable for screening and detection of large main effects. The structure of PBD has been already extensively explained in some references [93]. If the required number of factors is smaller than $N-1$, by adding dummy factors design can be completed. Dummy factors are imaginary factors such as color of door which practically do not have any impact on the response, but they can be used for estimation of experimental error [89, 94]. Since PBD cannot be demonstrated as cubes, they are often called nongeometric designs [73]. The experimental matrix of PBD can be easily obtained by writing the first row of the design table. The next rows can be generated by shifting the elements of the previous row to the right. The last raw will be a row with minus levels. The experimental matrix of an 8-factor PBD is shown in Table 1-4.

Table 1-4. Experimental matrix of PBD for an 8-factor system.

	Factors						
Runs	A	B	C	D	E	F	G
1	+	–	–	+	–	+	+
2	+	+	–	–	+	–	+
3	+	+	+	–	–	+	–
4	–	+	+	+	–	–	+
5	+	–	+	+	+	–	–
6	–	+	–	+	+	+	–
7	–	–	+	–	+	+	+
8	–	–	–	–	–	–	–

It is worth mentioning that besides the screening purpose, PB designs are commonly used for robustness evaluations in method validation [95].

1.6.1.5.1.2. Factorial design

Two-level factorial designs are mostly employed in early stages of systems involving several factors and can investigate the impact of the factors and their joint effect on a response. FD cannot discover higher orders such as quadratic effects. Since these designs have only two levels per factor (−1 and +1), it seems that the response is linear over the selected range for each factor [73]. If the required number of experiments in an FFD is too high to be practically feasible, a FrFD which requires less number of the experiments can be employed. However, FrFD cannot estimate all of the main and interaction effects separately because some of them are confounded and evaluated together. Therefore, FrFD calculates the certain coefficients of the model. For FrFD, the number of experiments is reduced by a number of *p* according to 2^{k-p} design. In the case of $p = 1$, the design is called half fractional design [96]. A schematic illustration of factorial design in various condition is shown in Fig. 1-14.

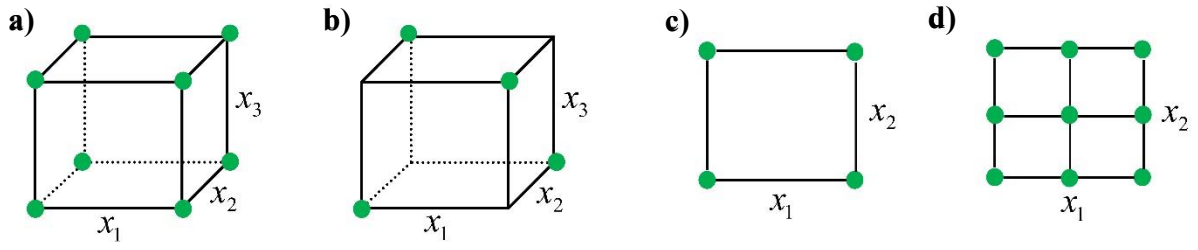

Figure 1-14. a) Full factorial design including three factors at two levels, b) half-fractional factorial design consisting of three factors at two levels; c) full factorial design for two factors at two levels; and d) full factorial design for two factors at three levels (which is the same as a faced-centred central composite design with one center point).

1.6.1.5.2. Response surface design

As mentioned before, optimization is the process of discovering the best optimum experimental condition or in other words, finds the best value for each factor. In order to select the potential factors, a screening step may be performed in advance [91], then optimization process can be employed. Fig. 1-15 demonstrates a general classification of a DoE approach.

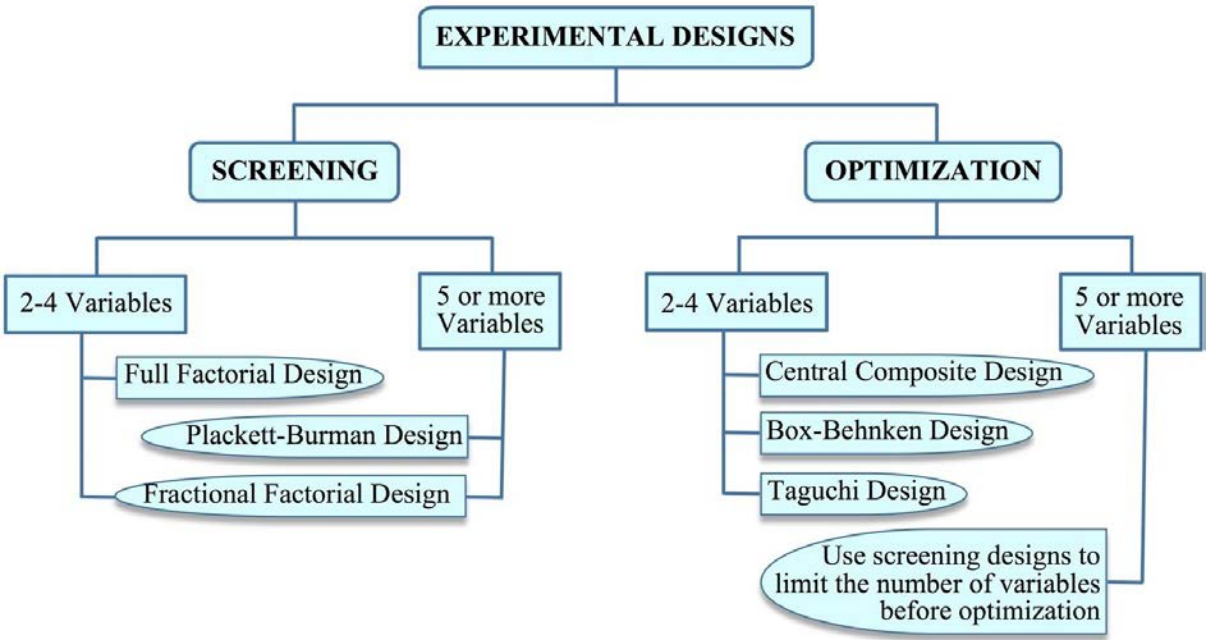

Figure 1-15. General classification of a DoE approach. Adapted from Ref [82] Copyright 2018, with permission from Elsevier.

Employed designs for optimization are classified into two groups: symmetrical and asymmetrical designs. FFD (three-level type), Doehlert design, Taguchi design (TD), Box-Behnken design (BBD), and Central Composite design (CCD) contain a symmetrical domain with center points (n_0) for prediction of exploratory error [82]. In addition to these models, D-optimal design is able to form an asymmetrical shape for investigation of asymmetrical experimental domain, and a symmetrical shape for symmetrical domain is much more useful. Mixture design can be also employed to examine mixture factors only such as the constitution of a mixture. ANOVA, which analyzes the data by an F-test, can be used for the statistical

analysis of response surface designs. The F-value of factors indicates the proportion of variance to the experimental error [82]. Table 1-5 depicts a summarized comparison of optimization designs.

Table 1-5. Comparison of common screening designs. Adapted from Ref [91] Copyright 2014, with permission from Elsevier.

Design	Type of factors	Factor levels	Number of experiments
3 levels Full Factorial Design (3-FFD)	Numerical Categorical	3	3^{k*}
Box-Behnken Design (BBD)	Numerical Categorical	3	$2k\ (k–1) + n_0$
Central Composite Design (CCD)	Numerical Categorical	5	$2^{k-p} + 2k + n_0$
Doehlert Matrics (DMX)	Numerical Categorical	Different for each factor	$k^2 + k + n_0$
D-Optimal	Numerical Categorical	Different for each model. Irregular experimental domains	Selected subset of all possible combinations

*k is the number of the factors, p is the number for reduction of the full design, and n_0 the number of center points.

1.6.1.5.2.1. Central composite design (CCD)

CCD is an efficient design for fitting the second-order model [73], and consists of an embedded combination of an FFD or FrFD, a star design (α) and n replicates of central point (n_0). The factorial design has two levels for each factor (−1, +1), the star design three levels (−α, 0, +α), and the center point at the factor levels 0 (Fig. 1-16).

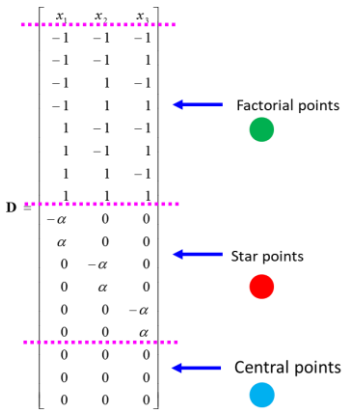

Figure 1-16. The experimental matrix of CCD representing the factorial points, Star points and central points.

In CCD, the total number of required experiments is determined by the following equation [96]:

$$N = 2^{k-p} + 2k + n_0 \qquad \text{Eq. 1-4}$$

where *k* is the number of factors, *p* is the number for reduction of the full factorial design, and n_0 is the number of center points. Based on the type of the CCD, the distance of the star points from the center can be different. In the case of uniformly rotatable design, it can be calculated from [63]:

$$\alpha = 2^{(k-p)/4} \qquad \text{Eq. 1-5}$$

Star points have a distance α from the center point, and their values determine the type of design, make it flexible, and allow estimation of curvature. Depending on the value of α, CCD can be classified into three types: circumscribed, face-centered, and inscribed (Fig. 1-17).

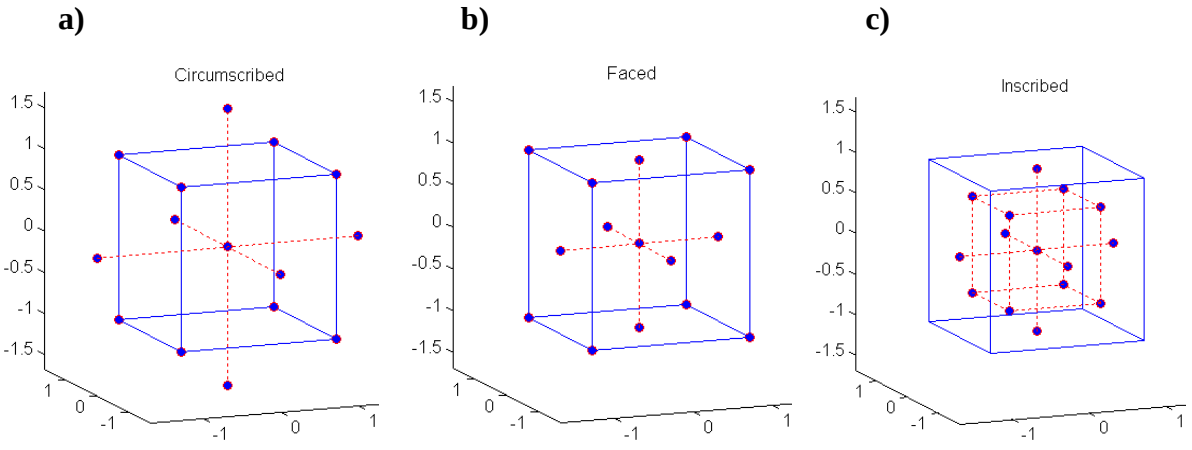

Figure 1-17. Three types of central composite design: a) circumscribed, b) face-centered, and c) inscribed.

In circumscribed CCD (Fig. 1-17a), star points have a distance α from the center point (Eq. 1-6), and their values determine the type of design, make it flexible, and allow estimation of curvature. Since the star points (α) represent new extreme values (low and high) for each factor in the design, all factors will be studied in five levels (−α, −1, 0, +1, + α) [61]. It is important for a second-order model to have good estimations over the region of interest. Good estimation

can be provided by rotatability which is providing a reasonably consistent and stable variance of the predicted response at points of interests. In other words, rotatability is a spherical property and puts all the factorial and axial design points on the surface of a sphere with a radius of $2^{(k-p)/4}$. It has to be noticed that sometimes the five levels are not equally spaced, hence it makes this type of design quite impractical. However, for having a good design, it is not necessary to have exact rotatability [66].

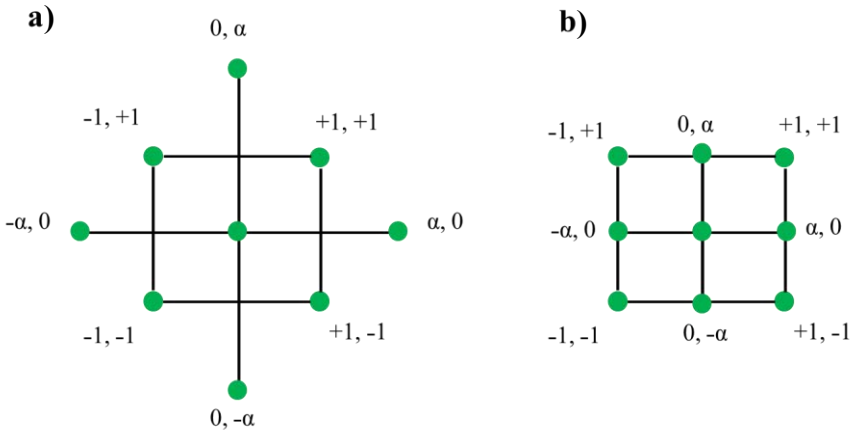

Figure 1-18. a) Circumscribed central composite design (CCCD), and b) face-centered central composite design (FCCD).

If the cuboidal region of interest is preferred to spherical, a face-centered central composite design in which $\alpha = 1$ (Fig. 1-18b) can be employed. In this design, the star points are located at the middles of the cube faces (Fig. 1-17b). In practice, it is frequently difficult to adjust the axial points, and since this design requires only three levels per factor, therefore it can be a good alternative of circumscribed type [66]. Faced-centered designs are not rotatable but provide relatively high-quality estimations over the experimental domain. It should be mentioned that precision for predicting of quadratic coefficients is not as good as with the circumscribed design.

Inscribed designs require five levels per factor and select points inside the defined ranges, but cannot represent the same prediction quality of the circumscribed design. In other words, in

this case, the alpha value is set to 1 and factorial corner points are inside the levels of the axial points (Fig. 1-17c). These designs are rotatable and well suited for estimating the coefficients in a second order model.

1.6.1.5.2.2. D-optimal designs

D-optimal designs can find the best subset of experiments (of predefined numerosity) minimizing the variance of the model regression coefficient. The *D* terminology is used because this design maximizes the determinant of the information matrix (X^TX), where X is the model matrix, and T denotes the transpose.

In order to construct a D-optimal design, first, the number of the probable effective factors and their levels are defined. Then, the total number of the possible experiments is calculated ($N= Level^{Factor}$), and in complex cases, it can be made by a huge number of experiments. The next step is finding a way allowing detection of the best possible subset of *n* experiments (N_{grid}) from the list of all the possible experiments (N).

The point selection process is mainly done by Fedorov exchange algorithm. For this purpose, the determinant of the information matrix and leverages of the *n* points were computed. Then, the leverages of remained points were computed ($N-N_{grid}$). At the next step, it detects the points of N_{grid} with the lowest leverage (these points are predicted as the best, and adding more points, will not provide further accessible information), and points of $N-N_{grid}$ with highest leverage meaning that these points were predicted as worst, and therefore by adding even one more points, a great improvement will occur. Finally, it exchanges some points of N_{grid} with $N-N_{grid}$ and tries to improve the quality of the selected points as much as possible. Due to this reason, the utilized algorithm is known as exchange algorithm. Since the algorithm starts with a random selection, and there is a possibility to face with a local maximum, whole procedure is repeated

several times (usually 10) and each time starts from a new and independent random selection. The solution with the highest determinant found during these repetitions will be retained as the final solution.

In all cases, the minimum required number of the experiments consists of main effects, interactions, quadratic terms, and an intercept. It is also obvious that a subset with *n* experiments provides better results than the *n-1* experiments but doing more experiments can increase the cost. Therefore, selection of appropriate number of the experiments is a challenge that can be solved by paying attention to normalized determinant M (Eq. 1-6):

$$M=\det(X'X)/n^{p} \qquad \text{Eq. 1-6}$$

where n is the number of experiments and p is the number of coefficients in the model. In this equation, by increasing the number of experiments, the numerator and denominator will increase, but M will decrease or increase accordingly to which one increases most. The computation of M for subsets made by an increasing number of experiments will allow detecting the best subset of experiments not only according to the value of the determinant of the dispersion matrix but also looking for the best compromise with the number of experiments to be performed.

From practical viewpoint, the sequence of operations that have been described in the previous step will be performed for all the possible subset sizes between a predefined minimum and maximum (usually the highest possible number of experiments that can be actually performed). Finally, the decision on how many experiments will be performed will be taken by looking at the corresponding plot of the variation of M versus the number of experiments (Fig. 1-19a) and inflation factor versos number of the experiments (Fig. 1-19b).

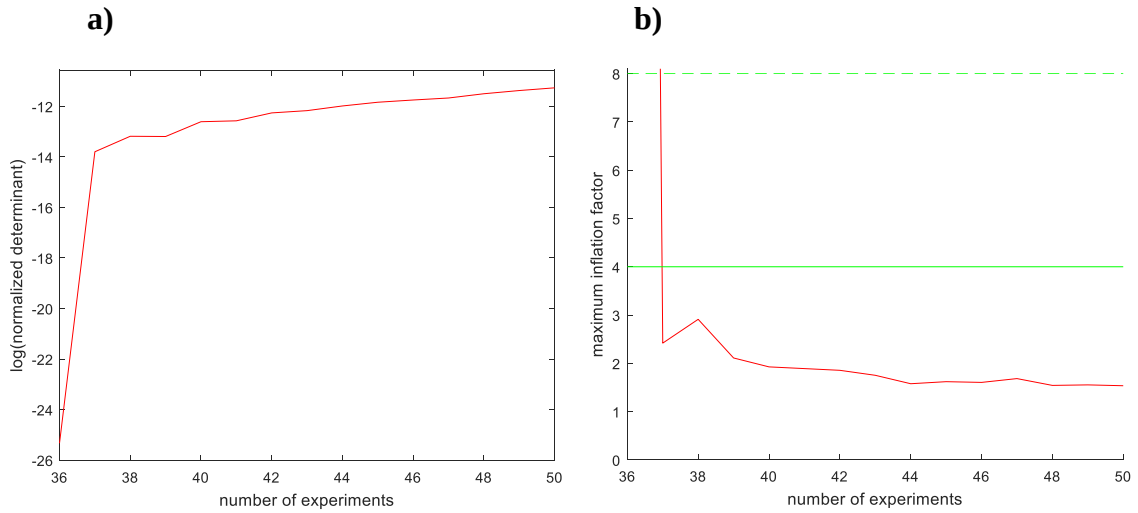

Figure 1-19. a) Logarithm of the normalized determinant vs. number of experiments; and b) highest inflation factor vs. number of experiments.

Compared to the other designs, D-optimal design calculates the coefficients requires with a minimum number of the experiments [80]. One of the advantages of D-optimal is that the optimum designs for quantitative factors do not depend on the scale of the variables [97]. A graphical illustration of D-optimal solutions is shown in Fig. 1-20.

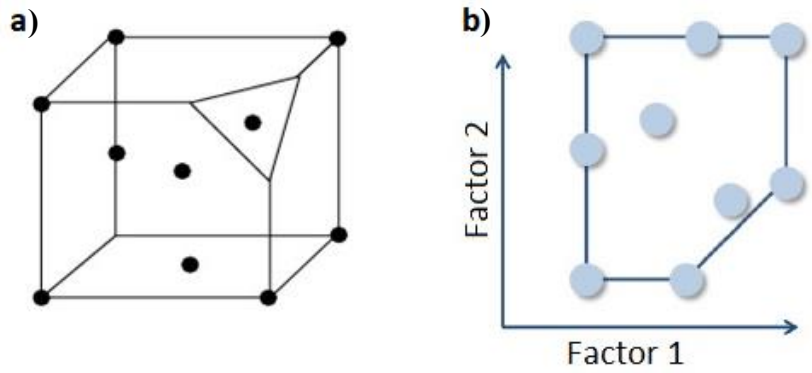

Figure 1-20. a) A graphical representation of D-optimal design, and b) a two-factor D-optimal with nine experiments, where the lower right part of the design due to experimental constraint is not accessible. Adapted from Ref [80] Copyright 2012, with permission from Elsevier.

D-optimal design can also be utilized for "repairing" the data matrix of previously performed inappropriate designs. For this purpose, the algorithm looks for those experiments that added to the already performed ones and increases extractable information of the system. In this way,

which called “D-optimal addition,” the quality of the information can be increased. It is surprising when one realizes how much the addition of a few ‘well-selected’ experiments will improve the quality of a ‘non-designed’ dataset [98]. D-optimal addition is another advantage of this design.

1.6.1.5.2.3. Box-Behnken design (BBD)

Box and Behnken (1960) have proposed three-level design (Fig. 1-21) for fitting response surfaces [68]. This design is a second-order rotatable (or near rotatable) incomplete factorial design [99]. In BBD, all points are located on a sphere of radius $\sqrt{2}$. According to a theoretical comparison, a BBD is more efficient than a central composite design (CCD) and requires a smaller number of the experiments [100]. Compared to CCD, points in BBD are located at the middle of the cube’s edges, not at the corners of the cube [101]. This feature can be beneficial when due to experimental constraints or cost it is not possible to check the points on the corners [100].

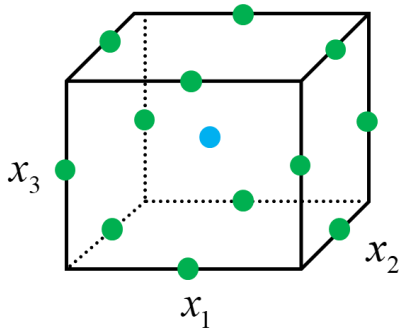

Figure 1-21. A three-factor Box-Behnken design with 13 runs.

In BBD, runs in which all factors are simultaneously at their lowest or highest levels are not included. Therefore, BBD is suitable for preventing experiments that would be performed under extreme conditions, which can lead to unsatisfactory results.

A shortcoming of this design is the representation of responses in dependence on a single factor. The reason is that the corner points of the cube are not quantified and have to be calculated by a proper response surface model [96].

1.6.1.5.2.4. Doehlert design

Doehlert design is not rotatable, but it can provide different qualities of predictions for each factor. Compared to the other designs, this design is more efficient and different numbers of levels can be defined for each factor [80]. Therefore, important factors can be investigated at more levels. The levels are equally spaced, which is suitable from a practical viewpoint because some factors can only differ with discrete steps (Fig. 1-22). Addition of a new factor after performing a first experimental design is also possible [98]. The geometric shape of this design is polyhedronic based on hyper-triangles (simplexes).

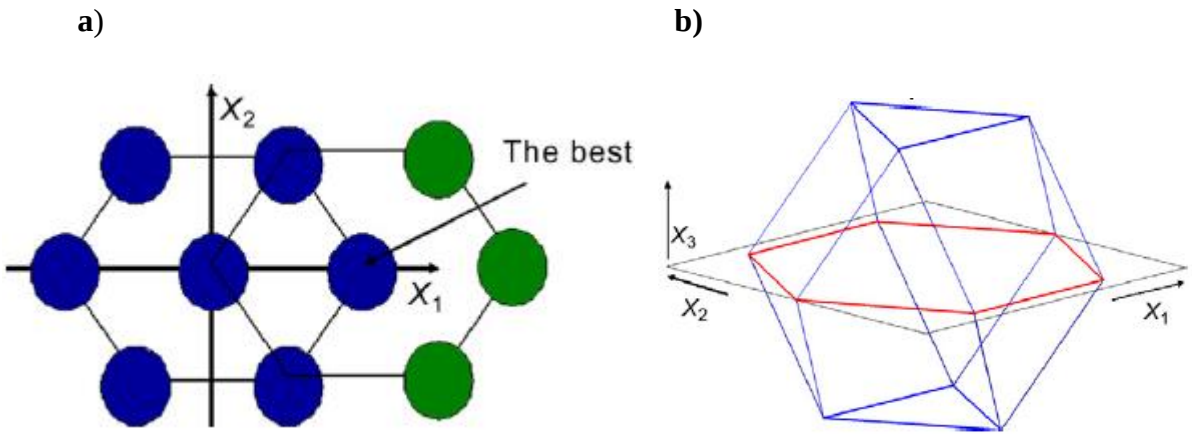

Figure 1-22. a) Sequential steps of a two-factor Doehlert design, and b) a Doehlert design for three factors. Adapted from Ref [98] Copyright 2013, with permission from Elsevier.

1.6.2. Data analysis

Data analysis includes the classification of data comprising various variables obtained from a number of samples. The goal of this approach is determination of all variations in the data matrix study. In other words, it tries to realize the correlations among variables and samples in a dataset and convert it into new latent variables [102]. Since classification problems are ubiquitous in all chemical fields [103], therefore various techniques have been reported.

Pattern recognition methods are classified into two main groups: supervised classification and unsupervised classification techniques. In the first group or discrimination, the class memberships are used to build a model. This method also contains quantitative prediction methods adapted to qualitative issues. The second category or clustering aims to classify the similar samples without using prior knowledge [104].

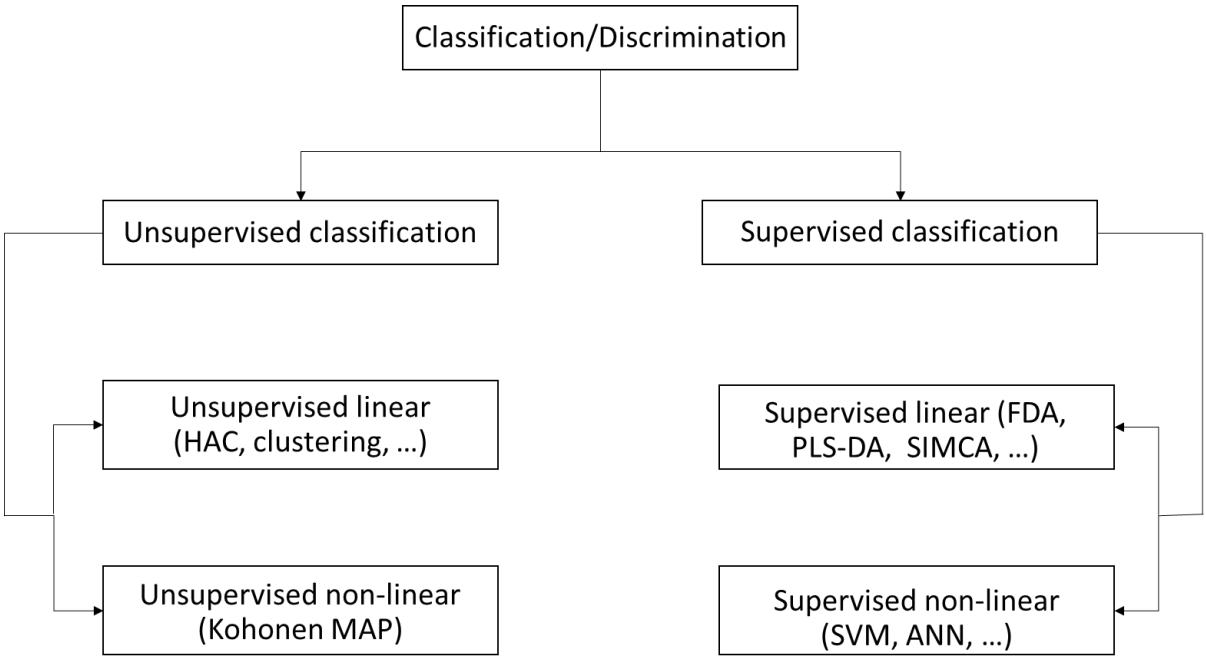

Figure 1-23. Classification methods in data analysis. Adapted with permission from Ref [104] Copyright 2014, Springer.

In discrimination technique, the sample classes of the calibration set are known and used. The aim of this technique is the creation of a discriminant model which enables classification of the unknown sample. A confusion matrix determines the model capability, showing the number of misclassified samples.

As it is shown in Fig. 1-23, several classification methods such as K-means, hierarchical ascendant clustering (HAC), artificial neural network (ANN), functional data analysis (FDA), partial least squares discriminant analysis (PLS-DA), support vector machines (SVM), and soft independent modeling of class analogy (SIMCA) have been utilized. Compared to the other methods, the PLS-DA is a commonly used classification technique, and most of the applications are in field of metabolomics. This method is based on the PLS technique in which the dependent variable is selected to depict the class integration. In this model, samples and variables have an exponential relationship, and the required number of samples is usually much smaller than variables [105]. In PLS-DA, class labels can be defined in two values for the dependent y vector; for instance 1 can be given to one of the classes and 0 or -1 for the other class. In the case of higher number of classes, a PLS2 algorithm with dummy variables are used. A much-used variant of PLS-DA is orthogonal PLS-DA (OPLS-DA) where the first components orthogonal to the dependent variable are eliminated from the dataset [106]. The resulting model has a single classification component, and the remained components represent the other variation which is orthogonal to the class information. OPLS by forcing all classification information into a single component can increase the interpretation of PLS. The estimation accuracy of both models is almost identical [107].

1.6.3. Image analysis

As mentioned in previous sections, colorimetric assays are the most commonly used detection methods. These techniques are suitable for diagnostic purposes because the required materials are inexpensive than antibodies, and the signal can be easily visualized [106]. In some cases, the prepared devices with this approach do not require any external instrument for signal readout. Distance-based [108] or text displaying devices [109] are frequent examples of these devices (Fig. 1-24).

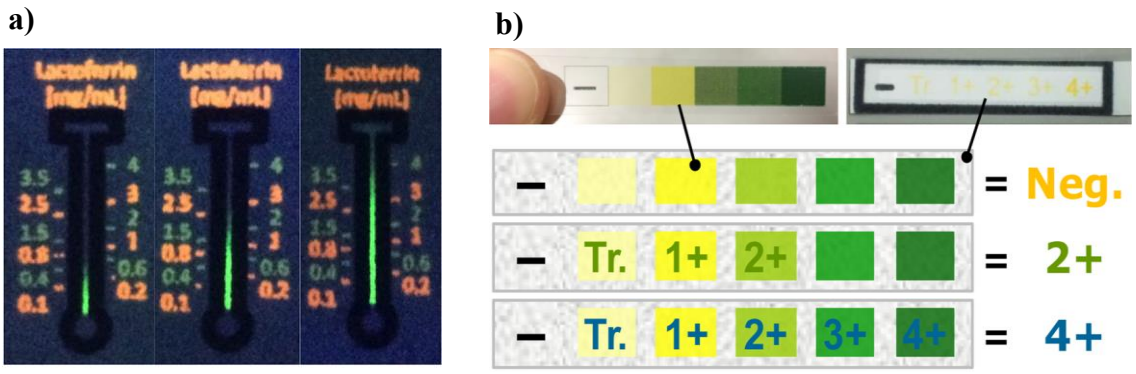

Figure 1-24. a) A distance-based device for the determination of tear lactoferrin, and b) a text-displaying device for the semiquantitative determination of urinary protein. Adapted with permission from Ref [108] Copyright 2015 American Chemical Society and [109] 2017 American Chemical Society, respectively.

In most cases, a digitizing step for the semiquantitative determination of analytical target is required. A flat-bed scanner or camera can perform the digitizing procedure. The advantages and disadvantages of scanner and camera have been already investigated [53, 107], but the simplicity of signal readout step is still a challenge. Since the inception of PADs, scanners have been utilized as an inexpensive detection system. The principle of scanners is similar to diffuse reflectance spectroscopy but in scanners filters rather than monochromator or prism are used to bin light into 3 or 4 wavelength ranges before recognition by charge-coupled device [110]. Compared to scanners, smartphone and digital cameras can be easily influenced by lighting condition of environment and image focus reliability is lower. Although digital cameras have

advantages such as automatic white balance correction, elimination of shutter speeds, and ISO settings but smartphone cameras are more user-friendly for signal interpretation. Thus, some attempts such as white balance adjusting [111, 112], have been taken to improve the weak points of this system. It is worth mentioning that preprocessing should be avoided in all digitizing systems. Otherwise, results will not be device-independent, and the colorimetric assay can be easily influenced by the type of device [53].

After taking the device image, the color analysis becomes an important step. This process can be performed by commercially available softwares such as Image J, Corel PhotoPaint, DigitalColor Meter, GenePix, Adobe Photoshop, Adobe Illustrator, MATLAB, and Python.

Depending on demand, various color spaces including L*a*b*, CIE, HSV, grayscale, RGB, or CMYK can be utilized for better analysis of the images [113]. For quantification or semi-quantitative purposes, a suitable channel of the color value or total space is selected, and the mean value of the selected color space within sensing area is reported as the response. Generally, the quantitative response is the mean value of the color intensity within the detection zone after correction for the blank sample. Since image processing can affect the sensitivity and precision of the device, therefore this procedure also plays an important role in device efficiency.

In traditional methods, checking the color values should be performed manually, and it is mostly limited to the analyzing of the three main color values (Red, Green, and Blue). Hence, it can be a risky and hard task to leave out inappropriate data with this procedure. In the case of image analsis by MATLAB, all the procedure from subtracting the blank value to extracting the related matrix and mean color value is done by software. Also, other color spaces such as ycbcr (y is luminance, cb blue-difference, and cr red-difference Chroma components), NTSC (National Television System Committee), and HSV (hue, saturation and value) can be performed by the developed algorithm. In this case, outlier detection will be based on the

profile of the image and not on the specific color intensity. For instance, in fabricated PAD for the determination of isoniazid, a square detection algorithm was used, and the developed method could detect all the sensing area appropriately. The only required thing is the image name and the total number of rectangles *N*, including blanks and samples that should be detected in the image. For example, in the Fig. 1-25, *N* is 16.

Color intensity = sqdetect ('imagefile.jpg', *N*) Eq. 1-7

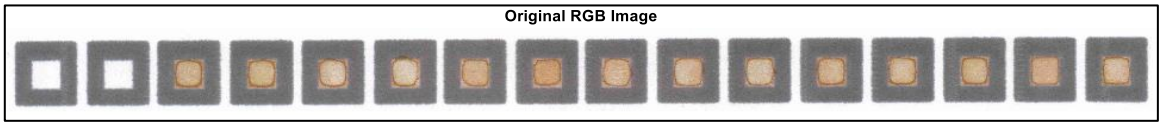

Figure 1-25. Original RGB image of isoniazid device including 2 blanks and 14 samples.

The first step involves segmentation of the RGB image, which is performed by setting a cut-off (160) of the intensity of the red channel of the image (Fig. 1-26):

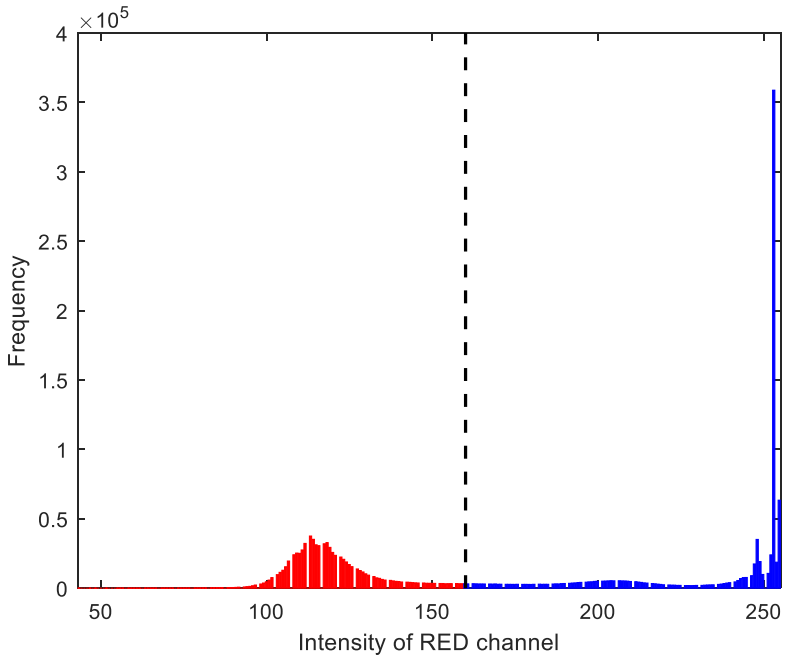

Figure 1-26. Selection of appropriate threshold for color analysis.

Then, the first two rectangles from the left side of the image are considered as blanks, and the remained squares recognized as samples (Fig. 1-27).

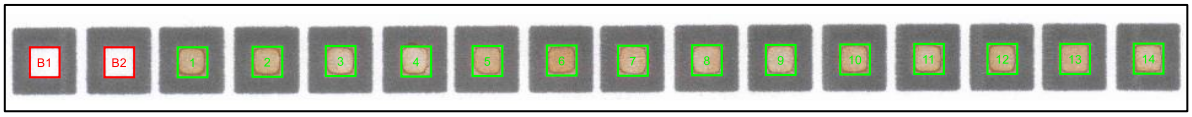

Figure 1-27. The automatically selected area by rectangle detection algorithm.

Finally, mean values of subtracted images for R, G, and B channels are reported. This digitizing step is important because not only minimizes the errors of manual detection zone selection, but also by having the data matrix of each image, outlier detection can be easily performed. In other words, by comparing the image profile or comparing the R, G, and B values of each image with other images at the same conditions detection of outliers will not be a difficult task. This simple but important step can also lead to a sensitive device, and worth to be paid more attention.

1.7. Objective of the research

As reviewed in this chapter, since the rediscovery of PADs in 2007, a wide range of studies has been carried out to improve the fabrication of PADs. In these studies, a great deal of attention focused on the investigation of fabrication techniques, modification of the printers, sensing mechanisms, selection of filter paper, paper modification, etc. In spite of such detailed investigations, researchers rarely paid attention to the capability of chemometrics. In other words, selection criteria or objective guidelines have not been reported for selection of appropriate experimental design models. Also researchers do not exactly know how to apply the models properly. This thesis is aiming to address the potential of chemometrics in the fabrication of reliable and sensitive PADs for point-of-care diagnosis. Beside the DoE approach, image analysis and data analysis are less paid attention parts of the reported works which seems to be crucial in this field. Hence, depending on condition, utilization of all chemometrical approaches will be described in the following chapters. Fig. 1-28 summarizes the outline of current thesis.

In **chapter 1**, introduces a brief review of paper-based analytical devices and chemometrical techniques.

Chapter 2 describes a comparative study of three common statistical designs including Box-Behnken design, central composite design, and D-optimal design in the optimization of paper-based analytical devices. Factors including device geometry and assay reagent amounts were optimized by the designs, and advantages and disadvantages of each design have been practically investigated. For this purpose, a simple colorimetric method using methyl orange as an indicator and isoniazid as an analytical target has been developed. In this work, to avoid human error during image analysis and increase the reproducibility of the process, an automatic algorithm for signal analysis was developed.

Chapter 3 describes chemometrics-assisted colorimetric uric acid assay on the inkjet-printed microfluidic paper-based analytical devices (µPADs). For this purpose, development of µPADs was assisted by experimental design, data analysis, and image processing. In optimization step, due to experimental constraints, Box–Behnken design was utilized for the optimization of the µPAD. Since the number of effective factors was quite high (9 factors), and none of them were neglectable, the optimization procedure was performed in two steps. Device geometry and assay reagent amounts were optimized separately, and the interaction between them assumed to be small. The validity of assumption was proved by performing verification experiments. In the data analysis step, a partial least squares discriminant analysis (PLS-DA) based on image profiles was successfully implemented as an automatic procedure for outlier classification. Measurement outliers were detected in real time by PLS-DA of scanned images. It should be mentioned that the colorimetric assay mechanism is based on the in-situ formation of AgNPs and yellow color of nanoparticles enables the semiquantitative determination of uric acid.

Chapter 4 describes fabrication of a paper-based isoniazid assaying analytical device optimized by central composite design. The DoE approach contributed to reduce the total amount of required experiments and therefore saves the time and cost. For this purpose, a seven-factor experimental design consisting of a total of 46 experiments was used for investigation of the impact of all probable factors on the device efficiency. The factors of interest were area length, area width, and sampling volume as factors related to device geometry, and amounts of the assay reagents polyvinyl alcohol (PVA), NH_3, and $AgNO_3$. Due to accurate deposition of the assay reagents, they were deposited by a thermal inkjet printer. The colorimetric assay mechanism of the proposed device is based on the formation of yellow silver nanoparticles (AgNPs). The in situ-formed AgNPs can be easily detected by the naked eye or with a simple flatbed scanner.

Chapter 5 is the summary of the results of this thesis and outlook on future developments.

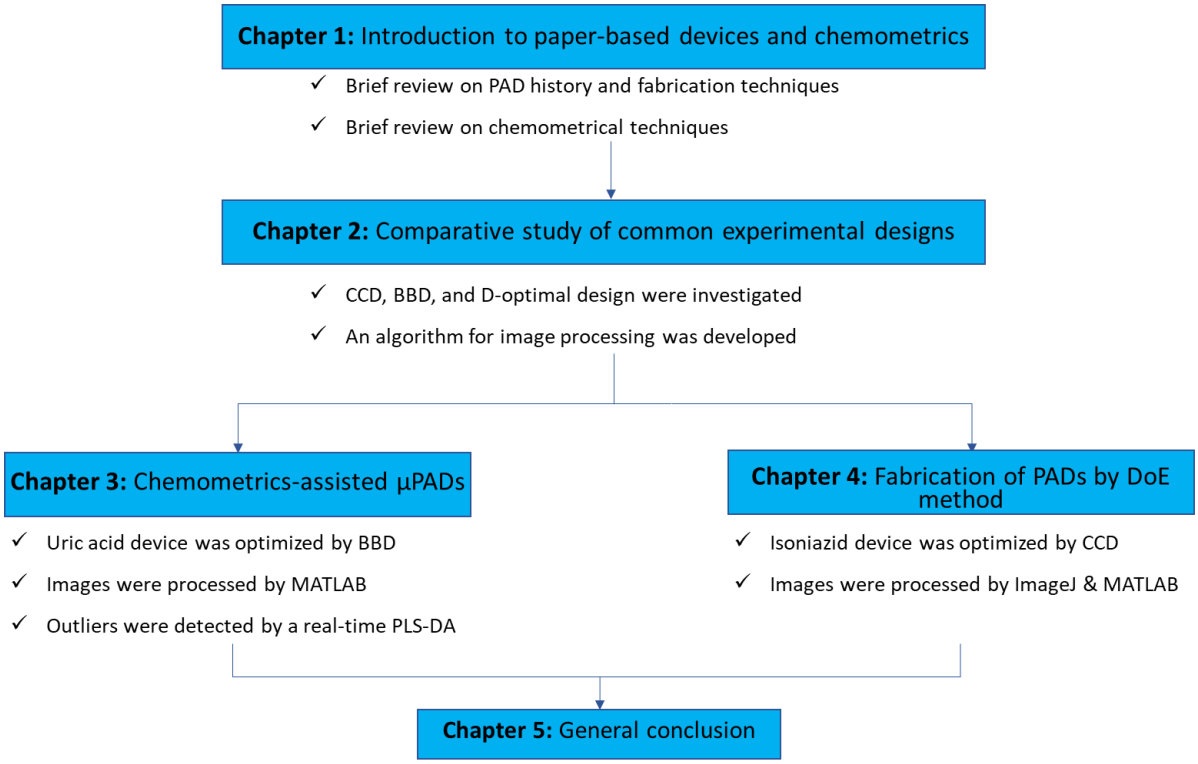

Figure 1-28. Outline of this thesis.

References

1. Morgan ED, Wilson ID (2004) An Early Description of Paper Chromatography? Chromatographia 60:135–136.

2. Rodney C (2005) Scientific American inventions and discoveries. John Wiley & Sons, Inc., New Jersey, US.

3. Maumené M (1850) On a new reagent for ascertaining the presence of sugar in certain liquids. The London, Edinburgh, and Dublin Philosophical Magazine and Journal of Science 36:482–482.

4. Nery EW, Kubota LT (2013) Sensing approaches on paper-based devices: a review. Anal Bioanal Chem. 405:7573–7595.

5. Oliver GA (1884) On Bedside Urine Testing, 2nd ed. H.K. Lewis, London, England

6. Yagoda H (1937) Applications of Confined Spot Tests in Analytical Chemistry: Preliminary Paper. Ind Eng Chem Anal Ed. 9:79–82.

7. Nobelprize.org The Nobel Prize in Chemistry 1952. In: Nobel Media AB 2014. https://www.nobelprize.org/nobel_prizes/chemistry/laureates/1952/. Accessed 1 Apr 2018

8. Stock R, Rice C (1974) Chromatographic methods, 3rd ed. Chapman & Hall, London, England.

9. Kunkel HG (1951) Electrophoresis of proteins on filter paper. J Gen Physiol. 35:89–118.

10. Rocco R (2006) Landmark Papers in Clinical Chemistry. Elsevier, San Diego, USA.

11. Liu H, Xiang Y, Lu Y, Crooks RM (2012) Aptamer-Based Origami Paper Analytical Device for Electrochemical Detection of Adenosine. Angew Chem Int Ed. 124:7031–7034.

12. Martinez AW, Phillips ST, Butte MJ, Whitesides GM (2007) Patterned Paper as a Platform for Inexpensive, Low-Volume, Portable Bioassays. Angew Chem Int Ed. 46:1318–1320.

13. Spence KL, Venditti RA, Rojas OJ, Habibi Y, Pawlak JJ (2010) The effect of chemical composition on microfibrillar cellulose films from wood pulps: water interactions and physical properties for packaging applications. Cellulose 17:835–848.

14. Tobjörk D, Österbacka R (2011) Paper Electronics. Adv Mater. 23:1935–1961.

15. Weigel G (2005) A strategic planning model for maximizing value creation in pulp and paper mills. Universite LAVAL. (http://hdl.handle.net/20.500.11794/18846).

16. Legnani C, Vilani C, Calil VL, Barud HS, Quirino WG, Achete CA, Ribeiro SJL, Cremona M (2008) Bacterial cellulose membrane as flexible substrate for organic light emitting devices. Thin Solid Films 517:1016–1020.

17. Pelton R (2009) Bioactive paper provides a low-cost platform for diagnostics. TrAC Trend Anal Chem. 28:925–942.

18. Lackinger E, Schmid L, Sartori J, Isogai A, Potthast A, Rosenau T (2011) Novel paper sizing agents from renewables. Part 1: Preparation of a paper sizing agent derived from natural plant oils. Holzforschung 65:3-11.

19. de Oliveira RAG, Camargo F, Pesquero NC, Faria RC (2017) A simple method to produce 2D and 3D microfluidic paper-based analytical devices for clinical analysis. Anal Chim Acta. 957:40–46.

20. Ramasamy S (1998) Oxygen sensor via the quenching of room-temperature phosphorescence of perdeuterated phenanthrene adsorbed on Whatman 1PS filter paper. Talanta 47:971–979.

21. Chen X, Chen J, Wang F, Xiang X, Luo M, Ji X, He Z (2012) Determination of glucose and uric acid with bienzyme colorimetry on microfluidic paper-based analysis devices. Biosens Bioelectron. 35:363–368.

22. Mentele MM, Cunningham J, Koehler K, Volckens J, Henry CS (2012) Microfluidic Paper-Based Analytical Device for Particulate Metals. Anal Chem. 84:4474–4480.

23. Cha R, Wang D, He Z, Ni Y (2012) Development of cellulose paper testing strips for quick measurement of glucose using chromogen agent. Carbohyd Polym. 88:1414–1419.

24. Hossain SMZ, Luckham RE, McFadden MJ, Brennan JD (2009) Reagentless Bidirectional Lateral Flow Bioactive Paper Sensors for Detection of Pesticides in Beverage and Food Samples. Anal Chem. 81:9055–9064.

25. Bracher PJ, Gupta M, Mack ET, Whitesides GM (2009) Heterogeneous Films of Ionotropic Hydrogels Fabricated from Delivery Templates of Patterned Paper. ACS Appl Mater Inter. 1:1807–1812 . doi: 10.1021/am900340m

26. Bracher PJ, Gupta M, Whitesides GM (2009) Shaped Films of Ionotropic Hydrogels Fabricated Using Templates of Patterned Paper. Adv Mater. 21:445–450.

27. Werner O, Quan C, Turner C, Pettersson B, Wågberg L (2010) Properties of superhydrophobic paper treated with rapid expansion of supercritical CO2 containing a crystallizing wax. Cellulose 17:187–198.

28. Peng P, Summers L, Rodriguez A, Garnier G (2011) Colloids engineering and filtration to enhance the sensitivity of paper-based biosensors. Colloid Surface B. 88:271–278.

29. Barr MC, Rowehl JA, Lunt RR, Xu J, Wang A, Boyce CM, Im SG, Bulović V, Gleason KK (2011) Direct Monolithic Integration of Organic Photovoltaic Circuits on Unmodified Paper. Adv Mater. 23:3500–3505.

30. Zhao W, van den Berg A (2008) Lab on paper. Lab on a Chip 8:1988-1991.

31. Martinez AW (2011) Microfluidic paper-based analytical devices: from POCKET to paper-based ELISA. Bioanalysis. 3:2589–2592.

32. Xia Y, Si J, Li Z (2016) Fabrication techniques for microfluidic paper-based analytical devices and their applications for biological testing: A review. Biosens Bioelectron. 77:774–789.

33. Schilling KM, Jauregui D, Martinez AW (2013) Paper and toner three-dimensional fluidic devices: programming fluid flow to improve point-of-care diagnostics. Lab Chip 13:628.

34. Sher M, Zhuang R, Demirci U, Asghar W (2017) Paper-based analytical devices for clinical diagnosis: recent advances in the fabrication techniques and sensing mechanisms. Expert Rev Mol Diagn. 17:351–366.

35. Li X, Tian J, Nguyen T, Shen W (2008) Paper-Based Microfluidic Devices by Plasma Treatment. Anal Chem. 80:9131–9134.

36. Olkkonen J, Lehtinen K, Erho T (2010) Flexographically Printed Fluidic Structures in Paper. Anal Chem. 82:10246–10250.

37. Lu Y, Shi W, Jiang L, Qin J, Lin B (2009) Rapid prototyping of paper-based microfluidics with wax for low-cost, portable bioassay. Electrophoreisis. 30:1497–1500.

38. Carrilho E, Martinez AW, Whitesides GM (2009) Understanding Wax Printing: A Simple Micropatterning Process for Paper-Based Microfluidics. Anal Chem. 81:7091–7095.

39. Bruzewicz DA, Reches M, Whitesides GM (2008) Low-Cost Printing of Poly(dimethylsiloxane) Barriers To Define Microchannels in Paper. Anal Chem. 80:3387–3392.

40. Martinez AW, Phillips ST, Butte MJ, Whitesides GM (2007) Patterned Paper as a Platform for Inexpensive, Low-Volume, Portable Bioassays. Angew Chem Int Ed. 46:1318–1320.

41. Martinez AW, Phillips ST, Wiley BJ, Gupta M, Whitesides GM (2008) FLASH: A rapid method for prototyping paper-based microfluidic devices. Lab Chip 8:2146.

42. Maejima K, Tomikawa S, Suzuki K, Citterio D (2013) Inkjet printing: an integrated and green chemical approach to microfluidic paper-based analytical devices. RSC Adv 3:9258–9263.

43. Kong F-Y, Gu S-X, Li W-W, Chen T-T, Xu Q, Wang W (2014) A paper disk equipped with graphene/polyaniline/Au nanoparticles/glucose oxidase biocomposite modified screen-printed electrode: Toward whole blood glucose determination. Biosens Bioelectron. 56:77–82.

44. Songjaroen T, Dungchai W, Chailapakul O, Laiwattanapaisal W (2011) Novel, simple and low-cost alternative method for fabrication of paper-based microfluidics by wax dipping. Talanta. 85:2587–2593.

45. He Y, Wu Y, Fu J-Z, Wu W-B (2015) Fabrication of paper-based microfluidic analysis devices: a review. RSC Adv. 5:78109–78127.

46. Lu Y, Shi W, Qin J, Lin B (2010) Fabrication and Characterization of Paper-Based Microfluidics Prepared in Nitrocellulose Membrane By Wax Printing. Anal Chem. 82:329–335.

47. Li X, Tian J, Garnier G, Shen W (2010) Fabrication of paper-based microfluidic sensors by printing. Colloid Surface B. 76:564–570.

48. Abe K, Suzuki K, Citterio D (2008) Inkjet-Printed Microfluidic Multianalyte Chemical Sensing Paper. Anal Chem. 80:6928–6934.

49. Li X, Tian J, Shen W (2010) Progress in patterned paper sizing for fabrication of paper-based microfluidic sensors. Cellulose 17:649–659.

50. Tisone TC, O'Farrell B (2009) Manufacturing the Next Generation of Highly Sensitive and Reproducible Lateral Flow Immunoassay. In: Wong R, Tse H (eds) Lateral Flow Immunoassay. Humana Press, Totowa, NJ, pp 1–26

51. Yamada K, Henares TG, Suzuki K, Citterio D (2015) Paper-Based Inkjet-Printed Microfluidic Analytical Devices. Angew Chem Int Ed. 54:5294–5310.

52. Magdassi S (2009) Ink Requirements and Formulations Guidelines. In: The Chemistry of Inkjet Inks. WORLD SCIENTIFIC, pp 19–41

53. Morbioli GG, Mazzu-Nascimento T, Stockton AM, Carrilho E (2017) Technical aspects and challenges of colorimetric detection with microfluidic paper-based analytical devices (μPADs) - A review. Analy Chim Acta. 970:1–22.

54. Ruecha N, Yamada K, Suzuki K, Citterio D (2017) (Bio)Chemical Sensors Based on Paper. In: Cesar Paixão TRL, Reddy SM (eds) Materials for Chemical Sensing. Springer International Publishing, Cham, pp 29–74.

55. Xu Y, Liu M, Kong N, Liu J (2016) Lab-on-paper micro- and nano-analytical devices: Fabrication, modification, detection and emerging applications. Microchim Acta. 183:1521–1542.

56. Awual MR, Hasan MM (2015) Colorimetric detection and removal of copper(II) ions from wastewater samples using tailor-made composite adsorbent. Sensor Actuat B Chem. 206:692–700.

57. Jain PK, Huang X, El-Sayed IH, El-Sayed MA (2008) Noble Metals on the Nanoscale: Optical and Photothermal Properties and Some Applications in Imaging, Sensing, Biology, and Medicine. Acc Chem Res. 41:1578–1586.

58. Cobley CM, Skrabalak SE, Campbell DJ, Xia Y (2009) Shape-Controlled Synthesis of Silver Nanoparticles for Plasmonic and Sensing Applications. Plasmonics. 4:171–179.

59. Mock JJ, Barbic M, Smith DR, Schultz DA, Schultz S (2002) Shape effects in plasmon resonance of individual colloidal silver nanoparticles. J Chem Phys. 116:6755–6759.

60. Hamedpour V, Postma GJ, van den Heuvel E, Jansen JJ, Suzuki K, Citterio D (2018) Chemometrics-assisted microfluidic paper-based analytical device for the determination of uric acid by silver nanoparticle plasmon resonance. Anal Bioanal Chem. 410:2305–2313.

61. Hamedpour V, Leardi R, Suzuki K, Citterio D (2018) Fabrication of paper-based analytical devices optimized by central composite design. Analyst. 143:2102-2108.

62. Lin Y, Gritsenko D, Feng S, Teh YC, Lu X, Xu J (2016) Detection of heavy metal by paper-based microfluidics. Biosens Bioelectron. 83:256–266.

63. Varmuza K, Filzmoser P (2009) Introduction to Multivariate Statistical Analysis in Chemometrics. CRC Press, Taylor & Francis Group.

64. Avoundjian A, Jalali-Heravi M, Gomez FA (2017) Use of chemometrics to optimize a glucose assay on a paper microfluidic platform. Anal Bioanal Chem. 409:2697–2703.

65. Pumtang S, Siripornnoppakhun W, Sukwattanasinitt M, Ajavakom A (2011) Solvent colorimetric paper-based polydiacetylene sensors from diacetylene lipids. J Colloid Interf Sci. 364:366–372.

66. Salles MO, Meloni GN, de Araujo WR, Paixão TRLC (2014) Explosive colorimetric discrimination using a smartphone, paper device and chemometrical approach. Anal Methods. 6:2047–2052.

67. Villa JEL, Poppi RJ (2016) A portable SERS method for the determination of uric acid using a paper-based substrate and multivariate curve resolution. Analyst 141:1966–1972.

68. Shariati-Rad M, Irandoust M, Mohammadi S (2016) Multivariate analysis of digital images of a paper sensor by partial least squares for determination of nitrite. Chemometr Intell Lab. 158:48–53.

69. Komatsu T, Mohammadi S, Busa LSA, Maeki M, Ishida A, Tani H, Tokeshi M (2016) Image analysis for a microfluidic paper-based analytical device using the CIE L*a*b* color system. Analyst 141:6507–6509.

70. James Lind. In: Wikipedia. https://en.wikipedia.org/wiki/James_Lind. Accessed 1 Apr 2018

71. Charles Sanders Peirce. In: Wikipedia. https://en.wikipedia.org/wiki/Charles_Sanders_Peirce. Accessed 1 Apr 2018

72. Sir Ronald Aylmer Fisher. In: Encyclopaedia Britannica. https://www.britannica.com/biography/Ronald-Aylmer-Fisher. Accessed 1 Apr 2018

73. Montgomery DC (2012) Design and Analysis of Experiments, 8th edition. John Wiley & Sons, Inc., New Jersey, US.

74. Sharma N, Barstis T, Giri B (2018) Advances in paper-analytical methods for pharmaceutical analysis. Eur J Pharm Sci. 111:46–56.

75. Setti L, Fraleonimorgera A, Mencarelli I, Filippini A, Ballarin B, Dibiase M (2007) An HRP-based amperometric biosensor fabricated by thermal inkjet printing. Sens Actuat B Chem. 126:252–257.

76. Khan MS, Fon D, Li X, Tian J, Forsythe J, Garnier G, Shen W (2010) Biosurface engineering through ink jet printing. Colloid Surface B. 75:441–447.

77. Nishioka GM, Markey AA, Holloway CK (2004) Protein Damage in Drop-on-Demand Printers. J Am Chem Soc. 126:16320–16321.

78. Kuwahara K, Yamada K, Suzuki K, Citterio D (2018) Simplified determination of complex stoichiometry for colorimetric metal indicators by inkjet printing. Analyst. 143:1234–1241.

79. Ota R, Yamada K, Suzuki K, Citterio D (2018) Quantitative evaluation of analyte transport on microfluidic paper-based analytical devices (μPADs). Analyst 143:643–653.

80. Hibbert DB (2012) Experimental design in chromatography: A tutorial review. J Chromatogr B. 910:2–13.

81. Skartland LK, Mjøs SA, Grung B (2011) Experimental designs for modeling retention patterns and separation efficiency in analysis of fatty acid methyl esters by gas chromatography–mass spectrometry. J Chromatogr A. 1218:6823–6831.

82. Sahu PK, Ramisetti NR, Cecchi T, Swain S, Patro CS, Panda J (2018) An overview of experimental designs in HPLC method development and validation. J Pharm Biomed Anal. 147:590–611.

83. Yetilmezsoy K, Demirel S, Vanderbei RJ (2009) Response surface modeling of Pb(II) removal from aqueous solution by Pistacia vera L.: Box–Behnken experimental design. J Hazard Mater. 171:551–562.

84. Asghar A, Abdul Raman AA, Daud WMAW (2014) A Comparison of Central Composite Design and Taguchi Method for Optimizing Fenton Process. Sci World J. 2014:1–14.

85. Dejaegher B, Vander Heyden Y (2011) Experimental designs and their recent advances in set-up, data interpretation, and analytical applications. J Pharm Biomed Anal. 56:141–158.

86. Dejaegher B, Heyden YV (2007) Ruggedness and robustness testing. J Chromatogr A. 1158:138–157.

87. Dejaegher B, Vander Heyden Y (2008) 9 Robustness testing of CE methods. In: Separation Science and Technology. Elsevier, pp 185–224.

88. Dejaegher B, Vander Heyden Y (2009) The use of experimental design in separation science. Acta Chromatogr. 21:161–201.

89. Vander Heyden Y, Nijhuis A, Smeyers-Verbeke J, Vandeginste BG., Massart D. (2001) Guidance for robustness/ruggedness tests in method validation. J Pharm Biomed Anal. 24:723–753.

90. Sibinovic P, Smelcerovic A, Palic R, Djordjevic S, Marinkovic V (2005) Ruggedness testing of an HPLC method for the determination of ciprofloxacin. J Serb Chem Soc. 70:979–986.

91. Vera Candioti L, De Zan MM, Cámara MS, Goicoechea HC (2014) Experimental design and multiple response optimization. Using the desirability function in analytical methods development. Talanta 124:123–138.

92. Vander Heyden Y, Khots MS, Massart DL (1993) Three-level screening designs for the optimisation or the ruggedness testing of analytical procedures. Anal Chim Acta. 276:189–195.

93. Cavazzuti M (2013) Design of Experiments. In: Optimization Methods. Springer Berlin Heidelberg, Berlin, Heidelberg, pp 13–42.

94. Vander Heyden Y, Massart DL (1996) Chapter 3 Review of the use of robustness and ruggedness in analytical chemistry. In: Data Handling in Science and Technology. Elsevier, pp 79–147.

95. Dejaegher B, Dumarey M, Capron X, Bloomfield MS, Vander Heyden Y (2007) Comparison of Plackett–Burman and supersaturated designs in robustness testing. Anal Chim Acta. 595:59–71.

96. Otto M (2016) Chemometrics: Statistics and Computer Application in Analytical Chemistry, 3rd Edition. John Wiley & Sons, Inc, New Jersey, US.

97. Sarabia LA, Ortiz MC (2009) Response Surface Methodology. In: Comprehensive Chemometrics. Elsevier, pp 345–390.

98. Leardi R (2013) Experimental Design. In: Data Handling in Science and Technology. Elsevier, pp 9–53.

99. Box GEP, Behnken DW (1960) Some New Three Level Designs for the Study of Quantitative Variables. Technometrics. 2:455–475.

100. Zolgharnein J, Shahmoradi A, Ghasemi JB (2013) Comparative study of Box-Behnken, central composite, and Doehlert matrix for multivariate optimization of Pb (II) adsorption onto *Robinia* tree leaves: Multivariate optimization. J Chemometr. 27:12–20.

101. Bezerra MA, Santelli RE, Oliveira EP, Villar LS, Escaleira LA (2008) Response surface methodology (RSM) as a tool for optimization in analytical chemistry. Talanta. 76:965–977.

102. Kumar N, Bansal A, Sarma GS, Rawal RK (2014) Chemometrics tools used in analytical chemistry: An overview. Talanta. 123:186–199.

103. Marini F (2010) Classification Methods in Chemometrics. Curr Analy Chem. 6:72–79.

104. O'Donnell CP, Fagan C, Cullen PJ (2014) Process Analytical Technology for the Food Industry. Springer New York, New York, NY.

105. Westerhuis JA, Hoefsloot HCJ, Smit S, Vis DJ, Smilde AK, van Velzen EJJ, van Duijnhoven JPM, van Dorsten FA (2008) Assessment of PLSDA cross validation. Metabolomics. 4:81–89.

106. Martinez AW, Phillips ST, Carrilho E, Thomas SW, Sindi H, Whitesides GM (2008) Simple Telemedicine for Developing Regions: Camera Phones and Paper-Based Microfluidic Devices for Real-Time, Off-Site Diagnosis. Anal Chem. 80:3699–3707.

107. Trygg J, Wold S (2002) Orthogonal projections to latent structures (O-PLS). J Chemometr. 16:119–128.

108. Yamada K, Henares TG, Suzuki K, Citterio D (2015) Distance-Based Tear Lactoferrin Assay on Microfluidic Paper Device Using Interfacial Interactions on Surface-Modified Cellulose. ACS Appl Mater Inter. 7:24864–24875.

109. Yamada K, Suzuki K, Citterio D (2017) Text-Displaying Colorimetric Paper-Based Analytical Device. ACS Sensor. 2:1247–1254.

110. Poce-Fatou JA, Bethencourt M, Moreno-Dorado FJ, Palacios-Santander JM (2011) Using a Flatbed Scanner To Measure Detergency: A Cost-Effective Undergraduate Laboratory. J Chem Educ. 88:1314–1317.

111. Hong JI, Chang B-Y (2014) Development of the smartphone-based colorimetry for multi-analyte sensing arrays. Lab Chip 14:1725–1732.

112. Vashist SK, van Oordt T, Schneider EM, Zengerle R, von Stetten F, Luong JHT (2015) A smartphone-based colorimetric reader for bioanalytical applications using the screen-based bottom illumination provided by gadgets. Biosens Bioelectron. 67:248–255.

113. Coltro WKT, de Jesus DP, da Silva JAF, do Lago CL, Carrilho E (2010) Toner and paper-based fabrication techniques for microfluidic applications. Electrophoreisis. 31:2487–2498.

Chapter 2 Comparative study of CCD, BBD, and D-optimal design in fabrication of PADs

Summary

The current work presents a comparative study of Central Composite Design (CCD), Box-Behnken Design (BBD), and D-optimal design (Dopt) in the optimization of an isoniazid assay on a microfluidic paper-based analytical device (μPAD). A colorimetric method for the detection of isoniazid using methyl orange as an indicator was developed. Since this system requires time to complete the reaction, thus thin wax barrier used to delay the fluid delivery and provide enough reaction time. Seven factors of interest including areas of sensing zone and channel, diameters of inlet and indicator areas, and volumes of isoniazid, methyl orange, and phosphate buffer were selected and optimized. The limitations and strength of these designs have been experimentally examined. The results of three designs show similar statistical predictability of optimal conditions, and the highest predicted response belongs to D-optimal design. The optimum predicted response for CCD (90 experiments), BBD (62 experiments) and D-optimal (44 experiments) are 39.7, 38.0, and 45.0, respectively.

2.1. Introduction

Since the rediscovery of microfluidic paper-based analytical devices (µPADs) in 2007 [1], several attempts have been made to improve and facilitate the fabrication process of µPADs. In this regard, attention mainly focused on developing sensing mechanisms, substrate patterning techniques, and reagent deposition methods. Despite the strong potential of these devices, which is originating from intrinsic properties of paper and ideology of µPADs, they can rarely introduce themselves to the commercial markets. This problem is because of regulatory obstacles, analytical property concerns, problems with biological samples, lag in microfluidic technology, economics, and lack of appropriate optimization methods [2].

Optimization as a frequently used term in analytical chemistry demonstrates the experimental conditions which can lead to the best possible response [3]. Generally, optimization techniques can be categorized into two groups: univariate (one-factor-at-time) and multivariate (design of experiments). In the meantime, design of experiments (DoE) approach has several benefits over one-factor-at-time (OFAT) and is therefore preferable to it. Some remarkable advantages of DoE approach are: supplying overall information within the experimental domain, possibility of investigation of interactions and quadratic effects, requiring a small number of experiments, and providing maximum amount of information about experimental domain, which are not possible in OFAT [4].

The main goal of application of DoE approach is maximizing the desired response with a lower required amount of time, resources and materials, which is in agreement with µPADs principals. Although this technique as a statistical tool can be utilized for solving or addressing the problems, only a few µPADs have been developed by this approach. The reason is that the selection criteria or objective guidelines have not been reported for application of appropriate experimental model in optimization of µPADs, also because researchers do not know how to choose and apply the designs properly.

At the present work, a simple colorimetric method using methyl orange as an indicator and isoniazid as an analytical target is utilized. Isoniazid, which is also known as pyridine-4-carboxylic acid hydrazide or isonicotinic acid hydrazide, is one of the common medicines for the treatment of tuberculosis, is able to change the system color by deprotonation of the methyl orange. In other words, in acidic medium, protonated methyl orange species (red color) were deprotonated by isoniazid (orange color), and color change occurs.

Among optimization techniques, it was found that D-optimal design (Dopt), Box-Behnken design (BBD), and central composite design (CCD) are commonly used statistical designs [4, 2, 5–11]. This is because of their advantages in optimization of multivariate systems with an optimum number of the experiments [4]. Among the mentioned models, CCD is an efficient design for fitting the second-order model [12]. The term "composite" refers to the fact that such a design is composed of a full factorial or fractional factorial design and a star design, plus some replicates of the center point. The factorial design has two levels for each factor (−1 and +1), the star design three levels (−α, 0, +α), and the center point at the factor levels 0. Based on the α value, CCD can be a circumscribed CCD (CCCD) with $|\alpha| > 1$ investigating the factors at five levels (−α, −1, 0, +1, + α), or a face-centered CCD (FCCD) with $|\alpha| = 1$ examining the factors at three levels (−1, 0, +1) [13]. BBD is a three-level incomplete factorial design [14] and all points are located on a sphere with a radius of $\sqrt{2}$. The BBD is composed of a center point, and the points at the middle of the cube's edges [15], therefore it can be an advantage when experimental constraints or cost does not allow to check the points on the corners [16]. Dopt is generated by a computer algorithm and particularly useful when classical designs are not utilized. Dopt is able to minimize the variance of the model regression coefficient with the specified number of experiments, and the design is not relying on the scale of the factors [17]. Dopt design is becoming more useful when the factor space is not equally accessible, or the design-space is constrained.

BBD, and CCD contain a symmetrical domain with center points for prediction of exploratory error while Dopt has an asymmetrical shape for investigation of asymmetrical experimental domain, and a symmetrical shape for symmetrical domain [18]. Apart from these, the required number of experiments in each design is different. For example, for a seven-factor system, BBD needs 62 runs, CCD, and Dopt suggests 90 and 44 experiments, respectively. Therefore, a cost-effective strategy which provides maximum information with lower effort is preferred.

Herein, we demonstrate the application of DoE to optimize an isoniazid assay on a μPAD, relying on protonation and deprotonation of methyl orange. The first goal of this work is to show the potential of DoE approach in emboldening of μPADs. The second goal is to investigate a comprehensive understanding of possible effective factors on a μPAD and their optimization. The third goal is to compare the advantages and disadvantages of three common experimental design in the optimization of a seven-factor system. To the best of our knowledge, this is the first comparative study on development of a μPAD by three statistical models. We believe that this research will facilitate future studies by providing a guide for the selection of possible factors and suitable model.

2.2. Experimental section

2.2.1. Standard solutions and reagents

All chemicals were used without any further purification. A stock standard solution of isoniazid (0.01 mol L^{-1}) was prepared by dissolving of the appropriate amount of isoniazid (Sigma Aldrich) in ultra-pure water. A stock solution of methyl orange (4.0 g L^{-1}) was prepared by dissolving 0.4 g of methyl orange (Wako, Osaka, Japan) in ultra-pure water and diluting to 100 mL. The pH of the samples was adjusted to 3.1 with phosphate buffer (0.1 mol L^{-1}).

2.2.2. Instrumentation

Microfluidic patterns were printed by a ColorQube 8570 wax printer (Xerox, Norwalk, CT, USA). Post-print heating of the wax was performed by a QHE325 hot laminator (Meikoshokaiko Co., Ltd., Tokyo, Japan). The images of the device were scanned by a commercially available office scanner (CanoScan 9000F MARK II color scanner, Canon, Tokyo, Japan).

2.2.3. Software

The experimental designs were set up and analyzed using Statgraphics centurion XVII Package (ver. 17.2.00) and R based chemometric software developed by the Group of Chemometrics of the Italian Chemical Society (http://gruppochemiometria.it/index.php/software). Images were processed by a developed algorithm in MATLAB environment (MATLAB 9.3, The Mathworks Inc., Natick).

2.2.4. Image processing

First of all, the total number of squares (N) including blanks and samples, in the image is indicated (Eq. 2-1).

Color intensity = sqdetect('imagefile.jpg',N) Eq. 2-1

For instance, the total number of the squares to be detected in Fig. 2-1 is 12 (N = 12).

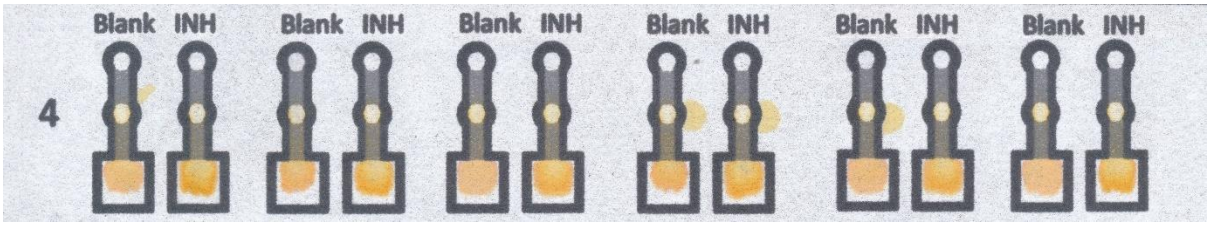

Figure 2-1. Fabricated μPADs by D-optimal design for detection of the isoniazid. This picture demonstrates an original RGB image including 6 pairs of devices with total number of the 12 squares.

The next step involves segmentation of the RGB image, which is performed by setting a cut-off of the intensity of each channel of the image. In more detail, the intensity histogram of each channel is built (Fig. 2-2) and the suitable cut-off level is selected for segmentation (Fig. 2-3). At the current work, due to appropriate detection of the outliers, all R, G, and B channels were obtained.

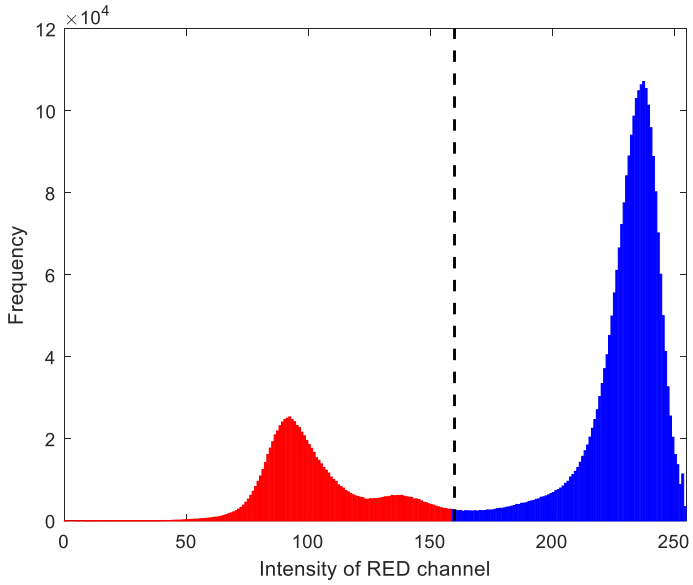

Figure 2-2. The intensity histogram of red channel. The cut-off level is adjusted to 160.

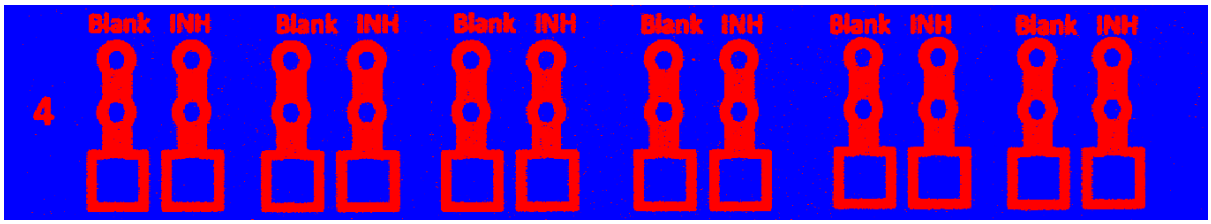

Figure 2-3. Segmented image of the device after adjusting the threshold.

Pixels with an intensity of the red channel lower than 160 (corresponding to black-ink areas) are coded as 0, while other pixels (with an intensity of the red channel equal or higher than 160, corresponding to red and white areas) are coded as 1. Furthermore, the half-upper part of the

image is blinded (all of the pixels are coded as 0), mainly to avoid interferences arising from the written text (Fig. 2-4).

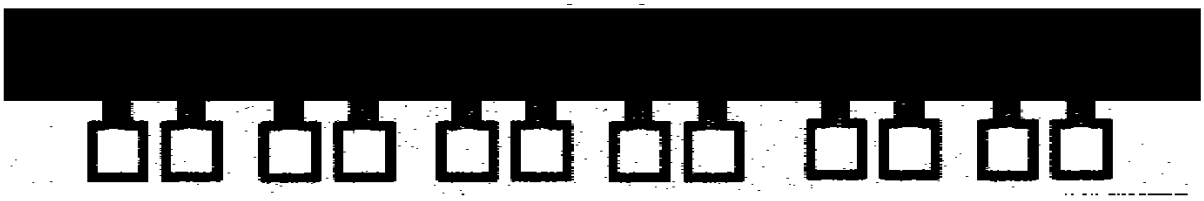

Figure 2-4. Logical image of the device after blinding the upper part of the device.

Such a logical binary image is then submitted to morphological analysis. The recognition algorithm automatically recognizes inside the image all the portions that contain pixels with coded value of 1 and can be modeled with a rectangular shape (Fig 2-5).

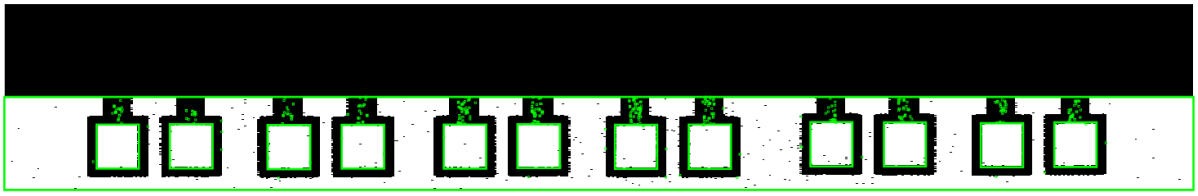

Figure 2-5. Complete detection of the rectangles after blinding the upper part of the image.

Area of each rectangle is evaluated, and rectangles are then sorted from the biggest to the lowest one (descending order). The biggest rectangle always corresponds to the external boundaries of the image, and it is not of interest. The subsequent N rectangles correspond to the areas to be detected, are retained by the algorithm. Further rectangles identified corresponding to very small defects in the edges of black squares and, being of null interest, they are deleted. At the end of this sorting procedure, only N rectangles of interest, corresponding to the inner parts of black-ink squares, are retained (Fig 2-6).

By default, the left side rectangles of pairs are considered as blank spots and marked with odd numbers. Further rectangles towards the right side of pairs are sample spots and marked with even numbers. Rectangular areas detected and coded as described are then used for

computations of descriptive parameters on samples. It should be mentioned that the subtracted mean R, G, and B values of each pair image in this study were utilized.

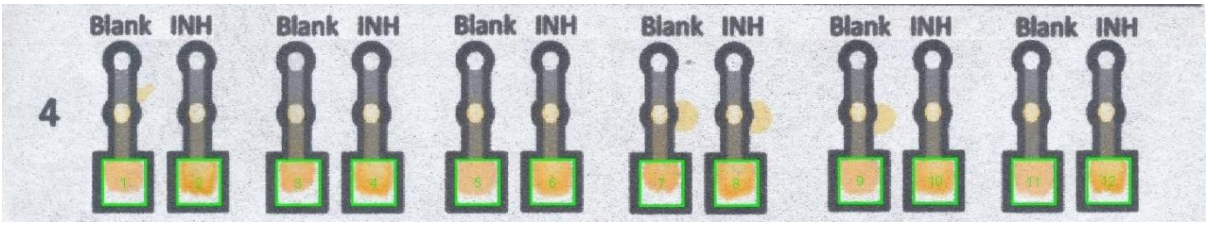

Figure 2-6. Complete detection of the rectangles after blinding the upper part of the image.

2.2.5. Device fabrication

First, Whatman No. 4 filter paper was cut and adjusted to A4 size; then the prepared pattern was printed on the top side of the filter paper by the wax printer. In order to avoid the sample leakage to the outside of the device, a gray scale cover was printed on the back side of the paper. Fig. 2-7 shows a real device with utilized dimensions and the corresponding color adjustments. In all cases, the pattern was printed in Black & White mode of the printer.

The printed wax was let to diffuse into the thickness of the paper by passing the sheet through the hot laminator. Finally, the assay reagents were deposited on the specified area by pipetting. It is worth mentioning that since the deposition of a large amount of the assay reagents in one step was not possible, thus for deposition of, e.g. 20 µL of methyl orange, a volume of 1 µL of the solution was 20 times pipetted. The similar approach was used for deposition of the phosphate buffer.

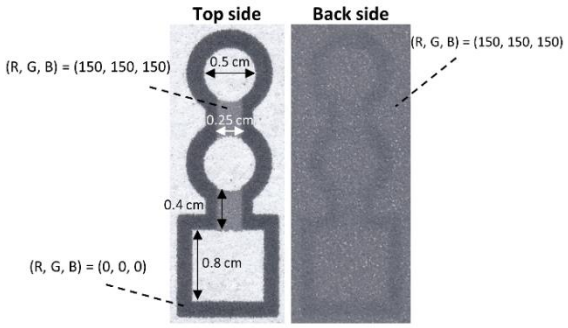

Figure 2-7. Images of top and back side of a µPAD representing the dimensions and wax printing adjustment.

As can be seen in Fig. 2-8, each device consists of three areas: inlet, indicator (central circle), and sensing. The inlet area was used for adding the sample, the central circle for deposition of the indicator, and the sensing area for pH adjustment of the mixture and detection purpose.

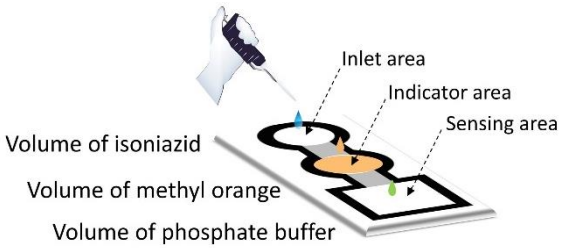

Figure 2-8. Graphical representation of a µPAD demonstrating the three areas and deposited assay reagents.

These three areas were connected through thin wax printed channels. Thin wax barriers were printed on a part of substrate thickness for enabling the delay of the fluid delivery, and therefore they provide enough time to complete the reaction. Fig. 2-9 demonstrates a graphical representation of thin wax barrier assisted sample delivery system.

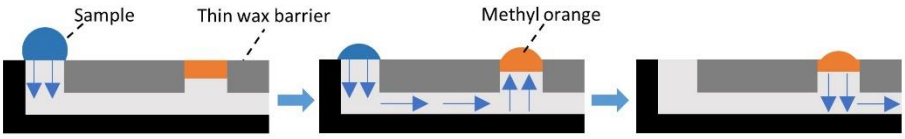

Figure 2-9. Schematic illustration of a thin wax printed channels sample flow process.

2.3. Results and discussion

2.3.1. Sensing mechanism

Methyl orange is frequently used in titrations as an indicator because of its distinct color changes. This indicator as an anionic terminated compound mediates the proton and electron transfer reactions through the amino groups (Fig. 2-10) [19]. Methyl orange shows red color in acidic medium, and by increasing the pH, the color changes to orange and yellow color.

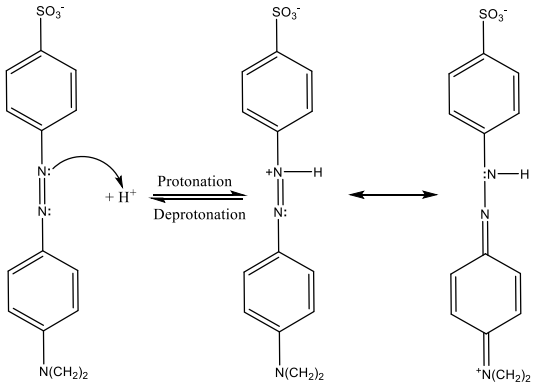

Figure 2-10. The protonation mechanism of methyl orange.

It has been already reported that in acidic medium, pyridine nitrogen group (pK 1.8) the NH_2 group of hydrazide (pK 3.5) has the potential for protonation. The examined UV-vis spectra of isoniazid solution in neutral condition shows a peak at 264 nm but in the acidic medium, the peak shifts to 268 nm and intensity increases which depicts the protonation of isoniazid [20]. In normal acidic condition, NH_2 can be easily protonated because of lower pK value (Fig. 2-11), but in strongly acidic medium, the isoniazid can be completely converted to deprotonated form [21].

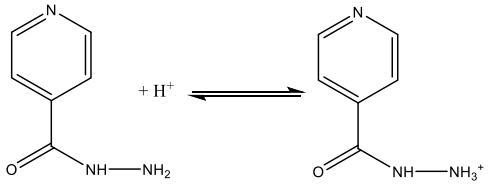

Figure 2-11. The protonation mechanism of hydrazide group in isoniazid

According to these, it is easily understandable that in a blank sample protonation of methyl orange occurs (MO), and color changes to red (Eq. 2-2).

$MO + H^+$ (Yellow) $\longrightarrow$ $MO(H^+)$ (Red) Eq. 2-2

In the presence of isoniazid, protonation of the isoniazid (INH) occurs, thus pH of the solution increases and color changes to yellow (Eq. 2-3). The color change from red to yellow is associated with the presence and concentration of isoniazid.

$INH + MO(H^+)$ (Red) $\longrightarrow$ $INH(H^+) + MO$ (Yellow) Eq. 2-3

Fig. 2-12 represents a pair of the fabricated µPADs after exposure to ultra-pure water (blank) and isoniazid (INH). The color difference between blank and sample can be easily detected by naked eye.

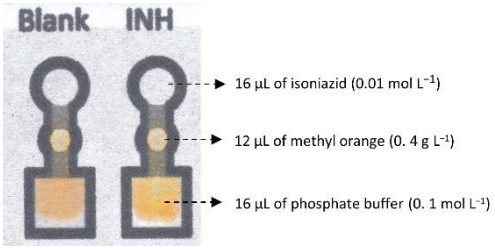

Figure 2-12. The µPAD after exposure to ultra-pure water (blank) and isoniazid (INH) sample.

2.3.2. Structure of the experimental designs

Since the type and variation of factors influencing the efficiency of µPADs are broad, the selection of an appropriate optimization technique with limited experimental effort can lead to high-performance devices. At the present work, central composite design (CCD), Box–Behnken design (BBD), and D-optimal design were applied for optimization of the device geometry and the assay reagent amounts. On the basis of preliminary test results, seven factors including areas of sensing zone and channel, diameters of inlet and indicator areas, and

volumes of isoniazid, methyl orange, and phosphate buffer were selected and optimized. Table 2-1 displays the factors and their levels.

Table 2-1. Experimental factors and levels of the CCD, BBD, and D-optimal for optimizing the µPAD.

Factor	Symbols	Level		
		-1	0	+1
Diameter of inlet area (cm)	A	0.3	0.5	0.7
Area of sensing zone (cm^2)	B	0.16	0.4	0.64
Diameter of indicator area (cm)	C	0.3	0.5	0.7
Area of channel (cm^2)	D	0.05	0.1	0.15
Sampling volume (µL)	E	12.0	16.0	20.0
Volume of methyl orange (µL)	F	12.0	16.0	20.0
Volume of buffer (µL)	G	12.0	16.0	20.0

It should be mentioned that during these preliminary tests, some factors such as types of filter paper and signal readout methods were investigated, and the best possible condition with lowest error was chosen. Due to this reason, these factors were not included in optimization step. In the case of filter paper selection, properties such as thickness, pore size, and sample flow speed (Table 2-2) were considered and the type with the quickest flow was selected (Fig. 2-13). The rapid device not only displays the results faster but also is less exposed by environmental conditions such as temperature and humidity.

Table 2-2. Properties of different filter papers.

Filter paper	Whatman grade 1	Whatman grade 4	ADVANTEC 5C
Particle retention size (µm)	11	25	1
Thickness (µm)	180	210	220
Density (g m^{-2})	87	92	118
Flow speed (second/ 100 ml)	150	37	570

In the case of signal readout techniques, since the evaluation of non-intensive color values/changes by naked eye because of the personal subjectivity leads to uncertainties, digital

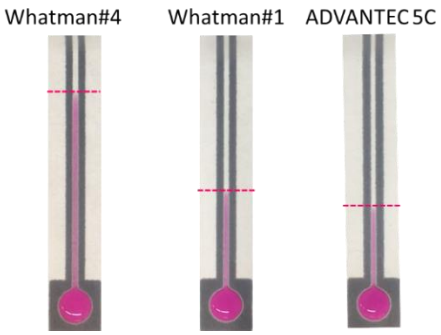

Figure 2-13. The transported distance during 5 min and under similar conditions (channel width= 0.25 mm, and sample volume= 50 µL) was investigated for three types of filter papers.

images were utilized instead. Digital images can be obtained by scanners, digital and smartphone camera. The previous studies investigated the effect of indoor fluorescent light, outdoor sunlight and indoor low light intensity on blue color value [22] (Fig. 2-14). Since this phenomenon is common in digital and smartphone cameras, the scanner was utilized to overcome these problems. In scanners, the scanning condition including distance and light source is fixed all the time, and high-resolution images with minimal impact of environmental condition lead to reproducible results.

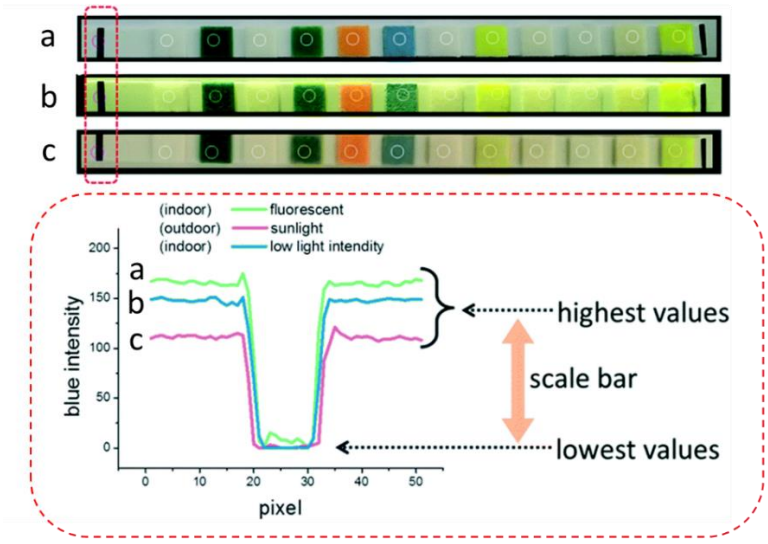

Figure 2-14. Investigation of the effect of various light condition on the blue color intensity. Adapted with permission from Ref [22] The Royal Society of Chemistry.

In this work, due to experimental limitations in device fabrication, a circumscribed central composite design which investigates new extreme values (α) for each factor, was not employed.

Fig. 2-15 shows an example of experimental constraint which leads to an inefficient device. In this device, the size of sensing area was not big enough, and therefore the sample could not reach to the specified zone. Hence, color changes did not occur. In addition, the appropriate deposition of the buffer on the specified area was a difficult task. In order to overcome these limitations, a face-centered central composite design was utilized.

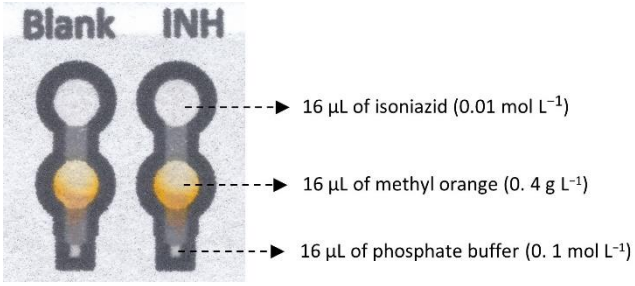

Figure 2-15. An example of experimental restriction in utilization of circumscribed central composite design. The obtained sensing area is too small, and the sample cannot flow till specified area.

Since FCCD does not require any other levels except (-1, 0, 1), star points are no longer problematic, and the stability of the design is quite good. In CCD, the number of the required runs (N) is calculated by the following equation:

$$N = 2^{k-p} + 2k + n_0 \qquad \text{Eq. 2-4}$$

where, k and n_0 represent the number of factors and center points (k = 7, n_0 = 12), respectively. In this equation, p is the number for reduction of the full design. In other words, instead of full factorial design, a half fractional factorial design (p = 1) will be embedded, and the number of the experiments will decrease [23]. Accordingly, a 6-block FCCD (2^{7-1} + 14 star points + 12 center points) with 90 experiments which enabled the estimation of the linear terms, the interactions, and the quadratic effects, was employed. The relationship between the response (blue color intensity) and the coded factors is in Eq. 2-5, in which the factors are coded according to Table 2-1. The standardized effects are also shown in Fig. 2-16. The adjusted-R^2 is 0.80, and the standard deviation of the residuals is 3.9. In this work, the equation together

with the Pareto chart (Fig. 2-16) is used to find the effective factors. In Fig. 2-16, the Pareto chart shows the absolute values of the standardized effects from the largest effect to the smallest effect. The length of each bar is proportional to the value of a t-statistic calculated for the corresponding effect. Any bars beyond the vertical line are statistically significant at the selected significance level, set by default at 5%.

$$\text{Color intensity} = 28.72 - 1.11A + 3.09B - 2.80C - 2.62D + 2.43E + 1.14F - 0.07G + 0.18A^2 + 0.03AB + 0.06AC - 0.77AD - 1.01AE - 1.14AF + 0.08AG - 5.62B^2 - 1.42BC - 1.78BD + 0.36BE + 1.64BF + 1.67BG - 5.07C^2 - 0.017CD + 0.83CE + 0.80CF - 0.90CG + 0.01D^2 + 0.08DE - 0.72DF + 0.98DG - 1.01E^2 - 0.23EF - 0.36EG - 0.82F^2 - 1.19FG - 0.19G^2 \quad \text{Eq. 2-5}$$

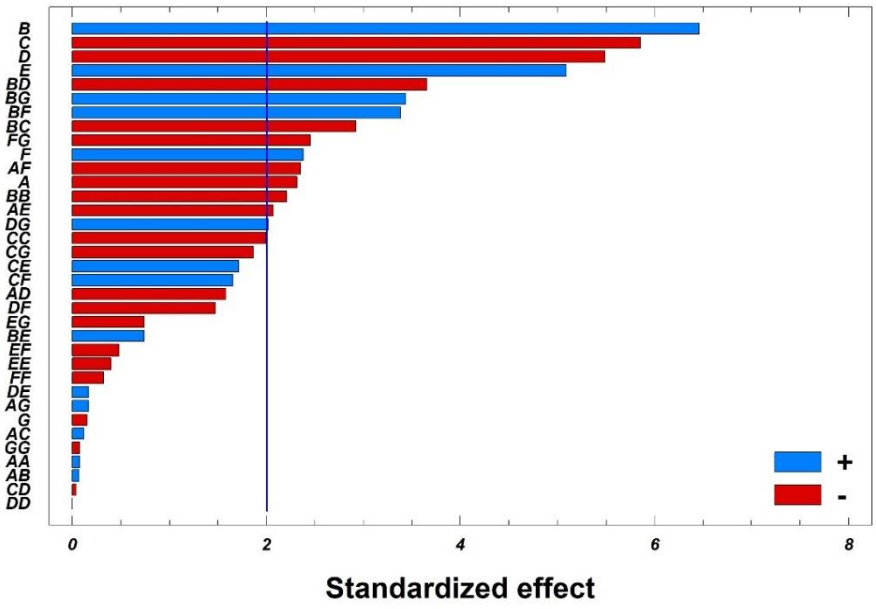

Figure 2-16. Pareto chart of the main effects obtained from the face-centered central composite design (FCCD). The factors were coded according to the Table 2-1. AA, BB, CC, DD, EE and FF are the quadratic terms of diameter of inlet area, area of sensing zone, diameter of indicator area, area of channel, sampling volume, and volumes of methyl orange, and phosphate buffer. AB, AC, AD, and AE are the interactions between pairs of factors.

The significant coefficients (P-values less than 0.05) are the all main factors except G, plus the interactions AE, AF, BC, BD, BF, BG, DG and FG, and the quadratic term for B. This means that all factors have significant impacts on the response. Three factors—area of sensing zone (coded as B), diameter of indicator area (C), and area of channel (D)—are by far the most

relevant, with the largest linear effects and highly significant interactions (BC, and BD). Factor B also shows a small quadratic effect (BB). Other factors such as diameter of inlet area (A), sampling volume (E), and volume of methyl orange (F) have significant linear effects. The volume of phosphate buffer (G) does not have a significant linear effect; however, its interactions are significant (BG, DG, and FG).

Since all the factors are involved in significant interactions or quadratic effect, thus, response surfaces can be used for better understanding of the phenomenon (Fig. 2-17a-h). In each plot, the effect of two factors can be studied while the remained factors were kept at the center levels.

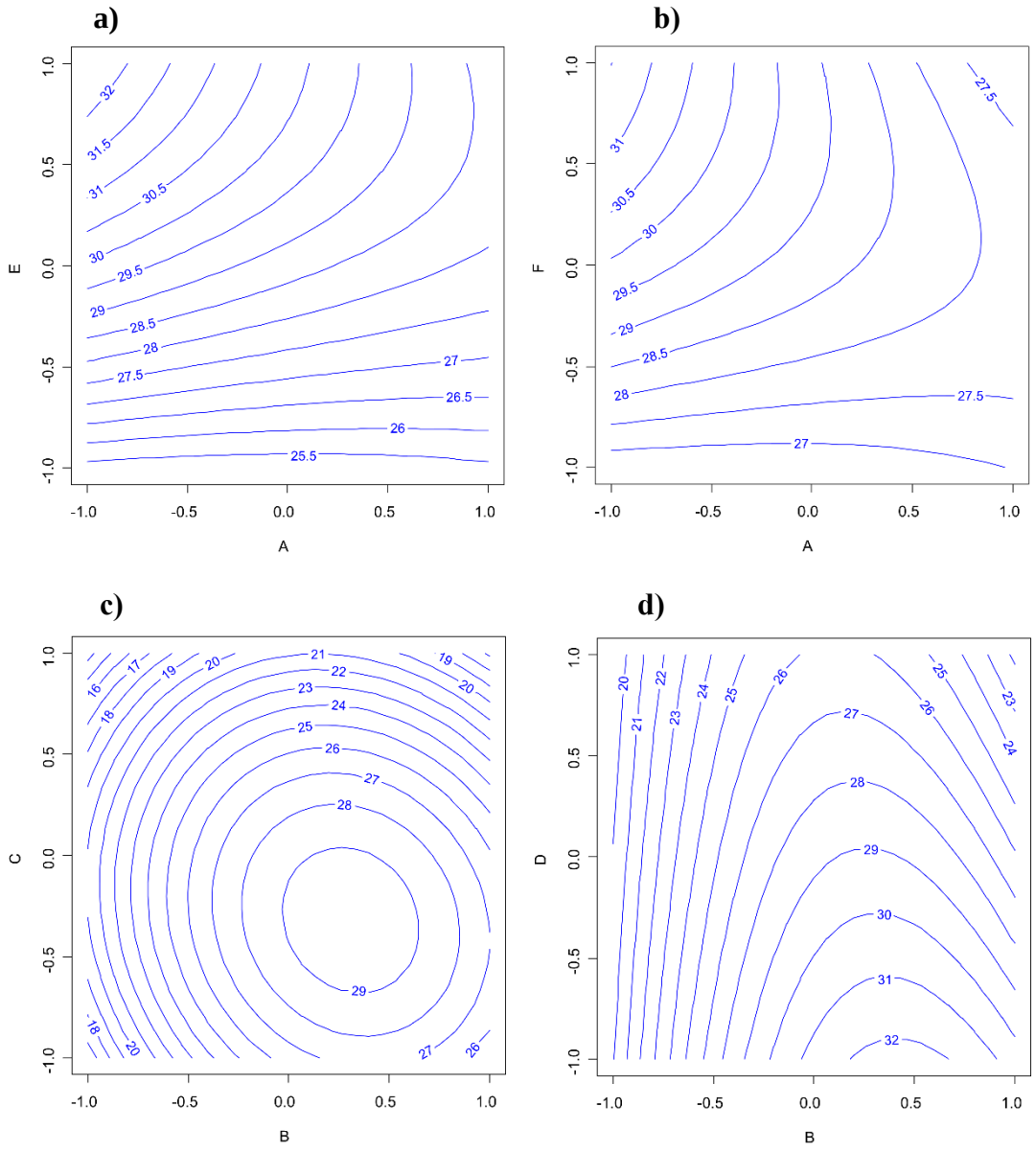

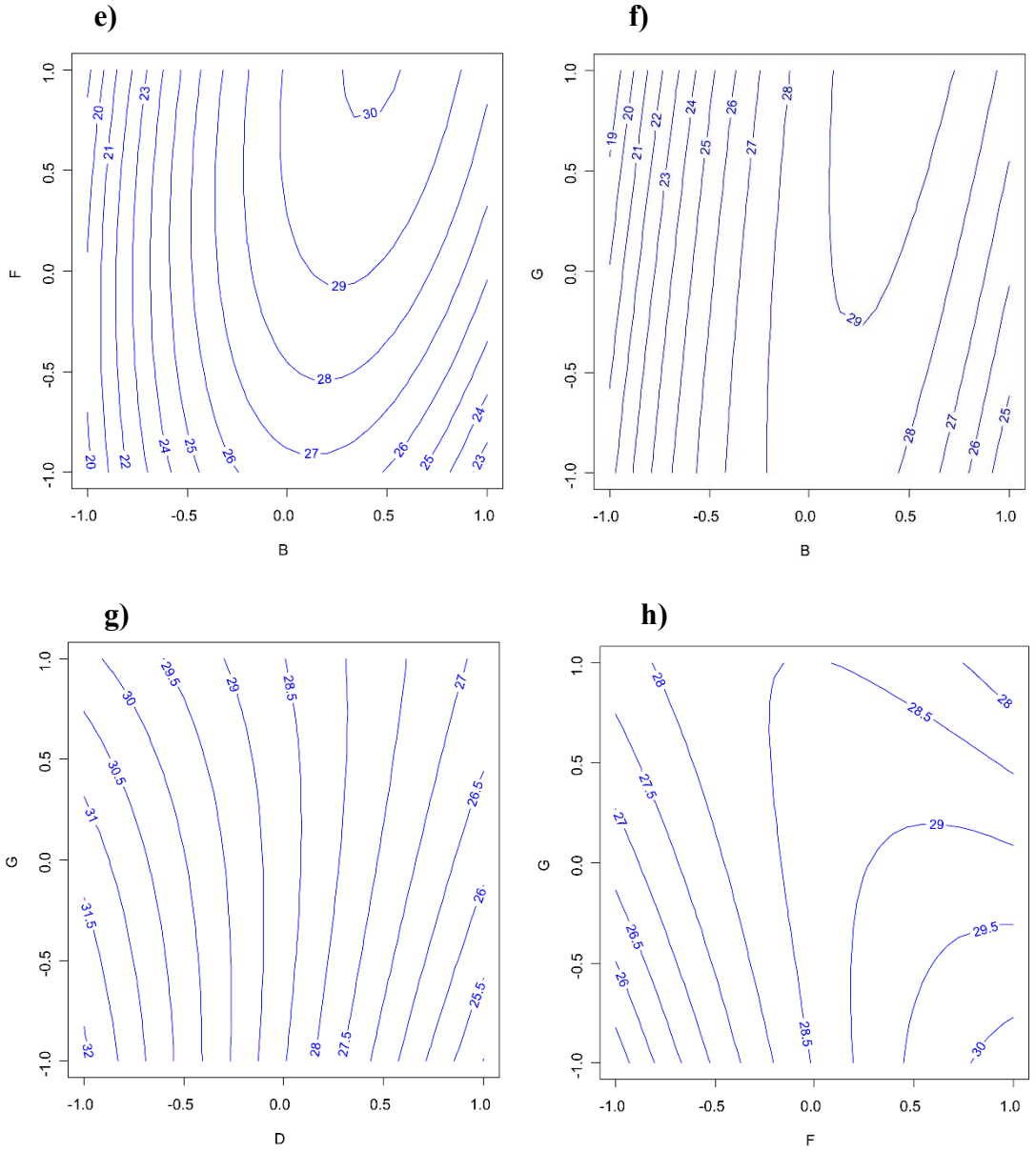

Figure 2-17. a) Response surface on the plane A–E (diameter of inlet area vs. sampling volume), b) response surface on the plane A–F (diameter of inlet area vs. volume of methyl orange), c) response surface on the plane B–C (area of sensing zone vs. diameter of indicator area), d) response surface on the plane B–D (area of sensing zone vs. area of channel), e) response surface on the plane B–F (area of sensing zone vs. volume of methyl orange), f) response surface on the plane B–G (area of sensing zone vs. volume of phosphate buffer), g) response surface on the plane D–G (area of channel vs. volume of phosphate buffer), and h) response surface on the plane F–G (volume of methyl orange vs. volume of phosphate buffer).

Fig. 2-17a displays the effect of diameter of inlet area and sampling volume (A–E) on the obtained response. According to this plot, by increasing the sampling volume while the size of the inlet area decreases, a significant increase in response can be observed. The reason for obtaining a better response is that the dead volume of sample in smaller sizes of inlet area will not be significant. Besides, by increasing the sampling amount, the achievable volume of

sample to the sensing area will increase, and therefore the obtained blue color intensity improves.

The response surface on the plane A–F (Fig. 2-17b) shows a similar correlation between the diameter of inlet area and volume of methyl orange. It means that when the size of inlet area is smaller and the amount of methyl orange is higher, the washed and transported amount of indicator to sensing zone will increase. Therefore, the response will become higher.

According to Fig. 2-17c, it can be seen that middle values of both areas of sensing zone (B) and diameter of indicator area (C) should be selected. Bigger indicator area can lead to a higher dead volume of the methyl orange, and smaller size can cause a higher error of assay reagent deposition. In the case of sensing zone, as mentioned before smaller sizes are not suitable and the bigger sizes can lead to color spread and lower response.

The response surface on the plane B–D (Fig. 2-17d) shows the response can be improved if at a middle level of factor B (area of sensing zone), area of channel (D) becomes smaller. It means that when the area of the channel is smaller, the dead volume of the sample will be lower. Therefore, transported amount of sample to the sensing zone and as a result response will be intensified.

Fig. 2-17e demonstrates the impact of area of sensing zone and volume of buffer (B–F) on the obtained color intensity. Similar to the previous cases, at a middle level of factor B, increasing the amount of methyl orange can culminate in the response.

From the plot 2-17f, it can be seen that lower value of phosphate buffer (B–G) should be selected. According to the Pareto chart (Fig. 2-16), factor G has a negative impact on the obtained response, and therefore higher values of this factor should be avoided. In other words, in a higher amount of buffer, protonation-deprotonation hardly occurs, and sensing mechanism does not work well.

Similar to the previous explanations, both factors (D–G) should be set to their lower values (Fig. 2-17g). In the case of plane F–G, a higher amount of indicator and lower amount of buffer can cause a better response. Since in this case, the transported amount of methyl orange increases, obtained color intensity will be raised.

Finally, based on the experimental design and the resulting equation, the optimal settings of the factors were chosen as diameter of inlet area 0.3 cm (coded as -1), area of sensing zone 0.52 cm^2 (0.5), diameter of indicator area 0.5 cm (0), area of channel 0.05 cm^2 (-1), sampling volume 20.0 μL (1), volume of methyl orange 20.0 μL (1), and volume of phosphate buffer 12.0 μL (-1). In this optimal condition, the predicted color intensity is 39.7.

Compared to CCD, points in BBD are not located at the corner of the cube, and it is an advantage when cost and experimental limitations do not allow to perform check those points. In other words, BBD is a spherical design and all points are located on a sphere of radius $\sqrt{2}$. Theoretical comparisons showed that a BBD is more efficient than a CCD and a small number of the experiments is required [16]. In BBD, runs which all factors are simultaneously at their lowest or highest levels are not included. Therefore, BBD is suitable for preventing experiments that would be performed under extreme conditions, which can lead to unsatisfactory results. In BBD, the number of the required runs is determined by the following equation [24, 25]:

$$N = k^2 + k + n_0 \qquad \text{Eq. 2-6}$$

Therefore, for a seven-factor system with 6 center points, 62 runs were required. It is worth mentioning that in BBD, 62 experiments were divided into 6 blocks and each block contained one center point. The resulting model, with an adjusted-R^2 of 0.90 and a standard deviation of the residuals of 2.1, is reported in Eq. 2-7. The Pareto chart of BBD is also shown in Fig. 2-18.

Color intensity = 28.25 - 1.27A + 5.16B - 5.39C - 2.61D + 1.66E + 1.42F - 2.21G + 0.25A^2 - 1.33 AB - 1.09AC - 1.44AD + 1.33AE - 0.87AF + 1.44AG - 5.23B^2 - 1.10BC - 0.96BD + 0.69BE + 0.21BF + 0.77BG - 4.04C^2 - 1.02CD + 1.17CE - 0.16CF - 1.63CG - 0.25D^2 + 2.28DE + 0.19DF - 0.96DG - 0.68E^2 + 0.93EF + 0.85EG - 0.60F^2 - 0.57FG - 0.03G^2 Eq. 2-7

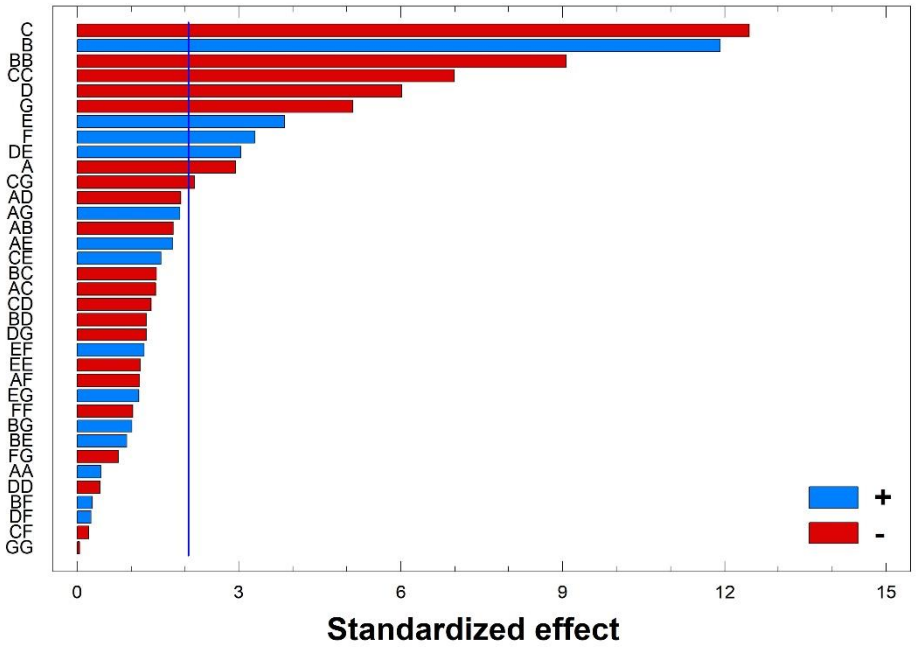

Figure 2-18. Pareto chart of the main effects obtained from the Box-Behnken design (BBD).

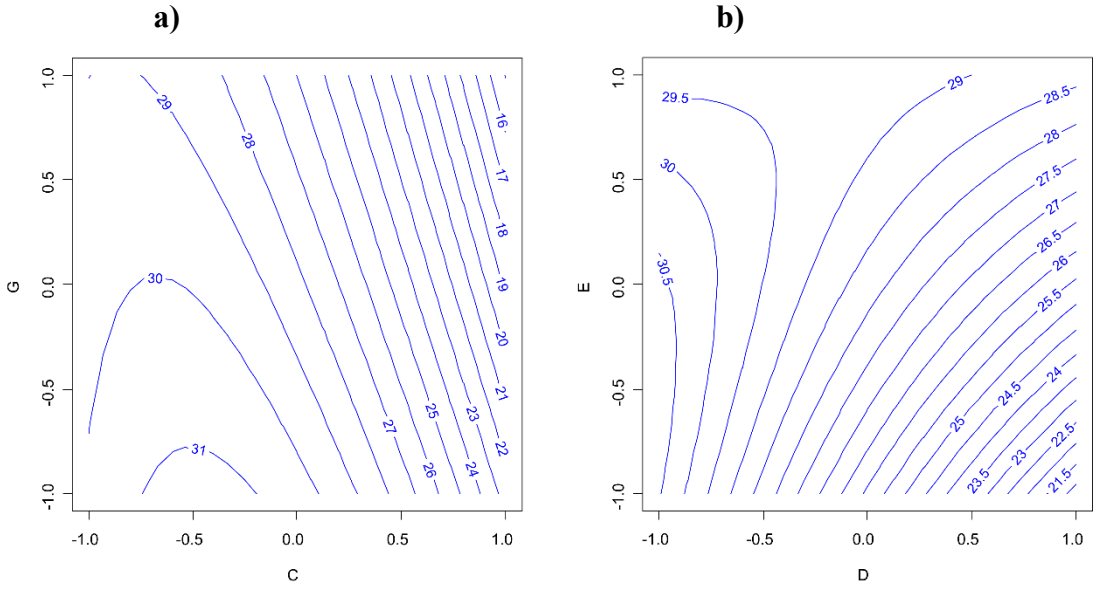

Figure 2-19. a) Response surface on the plane C–G (diameter of indicator area vs. volume of phosphate buffer), and b) response surface on the plane D–E (area of channel vs. sampling volume).

Fig. 2-19a depicts the effect of diameter of indicator area and volume of buffer (C–G) on the obtained response. According to this plot, at the middle level of indicator area, by increasing the volume of the buffer the color intensity decreases. Similar to the case of CCD, bigger size of indicator area has higher dead volume and smaller size has higher deposition error. Also, according to the Pareto chart (Fig. 2-18), the volume of buffer has a negative impact on the response and working at high levels is not recommended.

The plane D–E (Fig. 2-19b) shows the interactions between the area of channel and sampling volume. This interaction notifies that by increasing the area of channel, the dead volume of the sample raises. Hence, the amount of sample achieved to the sensing zone and as a result, response decreases. Also, increasing the sampling volume can transport more sample to the sensing zone, and therefore color intensity will be increased.

In summary, after the evaluation of the factors and their interactions, the following levels were chosen as optimum conditions: diameter of inlet area 0.3 cm (-1), area of sensing zone 0.56 cm^2 (0.7), diameter of indicator area 0.44 cm (-0.3), area of channel 0.04 cm^2 (-0.3), sampling volume 16.0 μL (0), volume of methyl orange 20.0 μL (1), and volume of phosphate buffer 12.0 μL (-1). The predicted color intensity for BBD is 38.0.

Unlike classical models, Dopt matrices are usually not orthogonal, and prediction of impacts are correlated. This design can be a good choice when the other models may fail because of the experimental constraints on the design space [26]. Dopt is an iterative technique which implies a great deal of computations and may need much time to be completed. The minimum number of the required experiments consists of main effects (7 experiments), interactions (21 experiments), quadratic terms (7 experiments), and an intercept. Therefore, at least 36 experiments are required. The computations show that performing 41 experiments is the best

choice and it is not worthwhile to perform extra experiments for trivial increasing of the matrix determinant (Fig. 2-20).

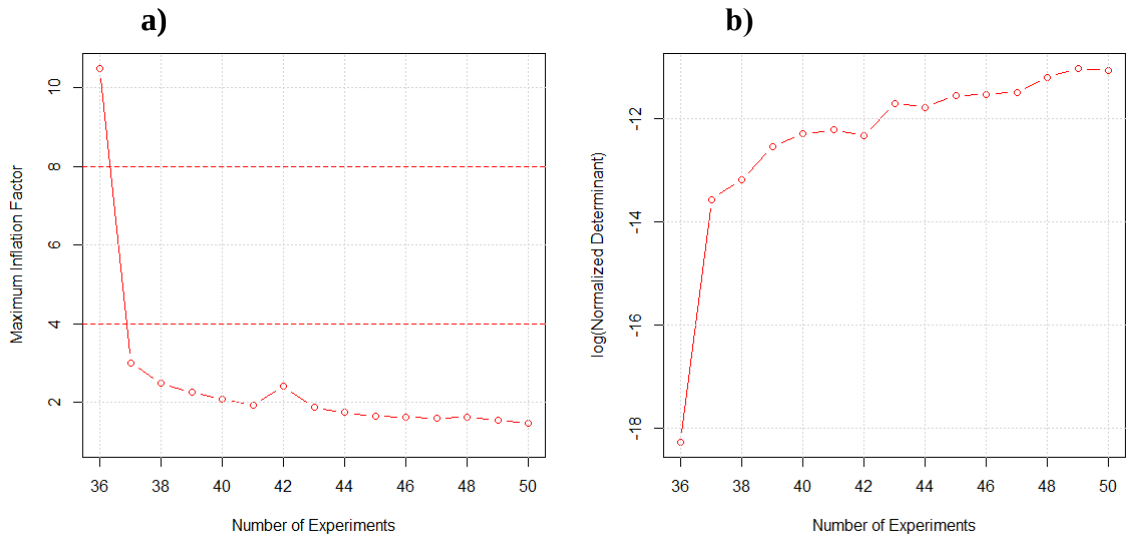

Figure 2-20. a) Maximum inflation factor versus number of experiments, and b) normalized determinant versus the number of experiments.

In this design, in order to a better understanding of the experimental domain, three extra points including two center points and one run with high levels of all factors were added to the experimental matrix. Thus, a system with 44 runs at 2 blocks was investigated. The relationship between the blue color intensity in the signal detection area and the factors (as coded values) are fitted with the Eq. 2-8. The Pareto chart of the D-optimal design is demonstrated in Fig 2-21.

$$\text{Color intensity} = 27.8043 - 1.23A + 5.38B - 5.23C - 2.64D + 1.60E + 1.80F - 1.84G + 0.44A^2 - 0.89AB - 1.12AC - 1.08AD + 2.02AE - 0.11AF + 1.50AG - 4.64B^2 - 1.7BC - 0.64BD - 0.10BE + 0.10BF + 0.29BG - 4.69C^2 - 1.84CD + 0.72CE - 0.32CF - 0.41CG + 0.84D^2 + 1.63DE - 0.59DF + 0.04DG - 0.14E^2 - 0.01EF + 0.30EG - 0.01F^2 - 0.50FG - 0.09G^2 \quad \text{Eq. 2-8}$$

It should be mentioned that the adjusted-R^2 and standard deviation of the residuals are 0.86 and 3.3, respectively.

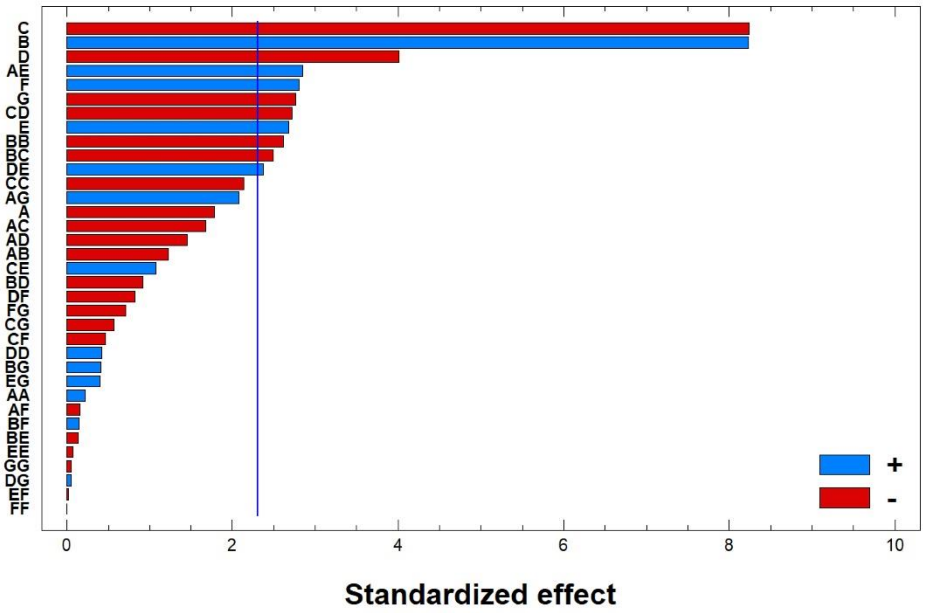

Figure 2-21. Pareto chart of the main effects obtained from the D-optimal design.

The response surface on the plane A–E (Fig. 2-22a) shows that lower levels of both factors is the best experimental condition. As the inlet area becomes smaller, the amount dead volume decreases. Also, by paying attention to the capacity of the device, high amount of sample is not required. Thus, lower values in both factors are the cost-effective choice.

Fig. 2-22b demonstrates that middle size of sensing zone and smaller indicator area can lead to higher response (plane B–C). As already discussed, big size of sensing area can spread the color, and therefore should be avoided. In the case of small size of indicator area, the dead volume of methyl orange will decrease. Hence, higher volume of indicator can reach to sensing zone and obtained color intensity increases.

The plane C–D (Fig. 2-22c) shows the interactions between the area of channel and sampling volume. It is clear that by having smaller sizes of indicator area and channel, the amount of transported sample to the sensing due to the lower dead volume will be higher. Thus, the response becomes higher.

In the case of response surface D-E (Fig. 2-22d), the capacity of the device is the main point. It means that by decreasing the value of D, the value of E must also be decreased.

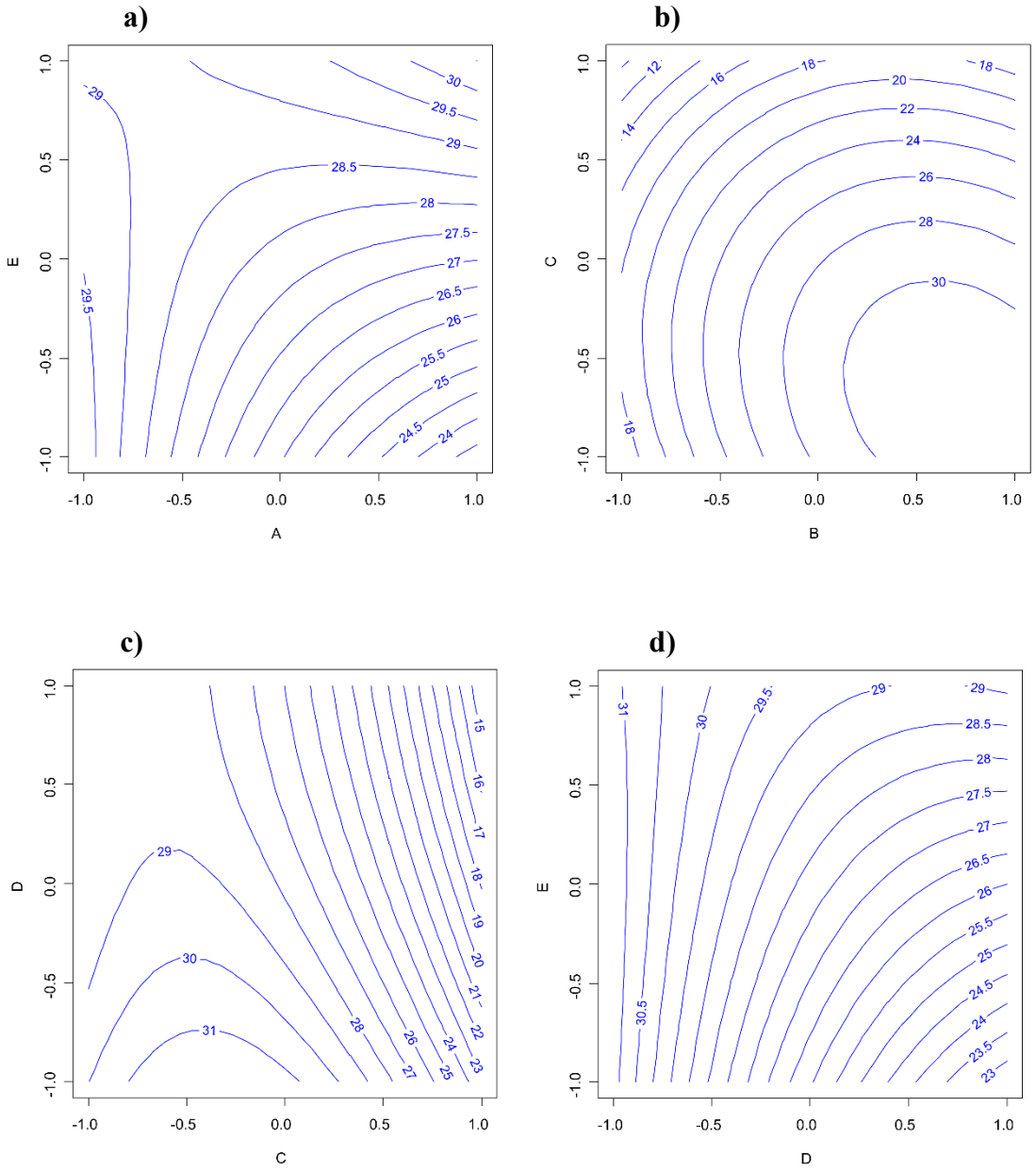

Figure 2-22. a) Response surface on the plane A–E (area of inlet area vs. sampling volume), b) response surface on the plane B–C (area of sensing zone vs. diameter of indicator area), c) response surface on the plane C–D (diameter of indicator area vs. area of channel), and d) response surface on the plane D–E (are of channel vs. sampling volume).

In D-optimal design, the conditions inside the experimental domain corresponding to the highest predicted response (45.0) are the following: diameter of inlet area 0.31 cm (-0.9), area

of sensing zone 0.56 cm^2 (0.7), diameter of indicator area 0.4 cm (-0.5), area of channel 0.05 cm^2 (-1), sampling volume 12.0 μL (-1), volume of methyl orange 20.0 μL (1), and volume of phosphate buffer 12.0 μL (-1).

As can be seen in all of three designs, linear terms including sensing area (coded as B), indicator area (C), thin wax area (D), and volumes of sample (E), and buffer (F) and quadratic effect of sensing area (BB), were similarly identified as significant terms. Also, the inlet area (A) in both FCCD and BBD, and volume of phosphate buffer (G) in both BBD and D-optimal were selected as effective factors. Table 2-3 demonstrates the optimal conditions for each design. According to this table, optimum volumes of methyl orange and phosphate buffer, which are the factors related to the sensing mechanism, are the same in all three designs. It proves that the ratio of two factor plays an important role and for having the highest response, it has to be +1 for methyl orange and -1 for phosphate buffer. Also, it can be seen that predicted response (blue color intensity) in D-optimal design, unlike the small number of the experiments, is higher. It means that performing more experiments does not always lead to the best results.

It has to be mentioned that the predicted responses are significantly higher than the best results obtained by the actually performed experiments within the design matrix of the models (for CCD, BBD, and D-optimal are 33.2, 37.9, and 36.7, respectively). This means that predicted models enable us to find the optimal condition even different and better than previously performed experiments. This response improvement is beneficial for low concentrations which mainly have low color intensities. Therefore, the increase of color value enables to work in lower concentrations with higher responses. In other words, in this way the detection limit (LoD) of the devices can be improved. The experimental matrix of three designs were reported in Appendix Chapter 2 Table 2-1.

Table 2-3. Obtained optimal levels (coded values) for CCD, BBD, and D-optimal.

Design	Inlet area (cm)	Sensing area (cm^2)	Indicator area (cm)	Channel area (cm^2)	Sampling volume (μL)	Methyl orange (μL)	Buffer (μL)	Predicted response
CCD	-1	0.5	0	-1	1	1	-1	39.7
BBD	-1	0.7	- 0.3	- 0.3	0	1	-1	38.0
D-optimal	- 0.9	0.7	-0.5	- 1	-1	1	-1	45.0

Table 2-4 shows the statistical parameters for all three designs. According to this table, the adjusted R-squared statistic is suitable for comparing models with different numbers of independent variables and the mean absolute error (MAE) is the average value of the residuals. The Durbin-Watson (DW) statistic evaluates the residuals to determine if there is any significant correlation based on the order in which they occur in data file.

Table 2-4. Comparison of the statistical parameters of the CCD, BBD, and D-optimal design.

Design	Runs	DF[1]	SD of residuals[2]	Adj-R^2 (%)[3]	MAE[4]	Durbin-Watson statistic
CCD	90	54	3.89	80.1	2.30	1.70 (p=0.1134)
BBD	62	26	2.12	89.7	1.10	1.91 (P=0.3348)
D-optimal	44	8	3.33	86.3	1.20	2.14 (p=0.6421)

[1]Degree of freedom [2]Standard deviation of residuals [3]Adjusted-R^2 [4]Mean absolute error

2.4. Conclusions

In spite of the long history of DoE approach, the application of statistical design at industrial and educational projects is still not extremely common, and using the traditional one-factor-at-time methodology leads to a suboptimal or optimal condition far from the ideal one. The rare application of DoE originates from lack of user-friendly statistical software and computing resources, and inadequate knowledge in fundamental of statistical concept and methods. The present work demonstrates the application of three common models of design of experiments (DoE) in the fabrication of µPADs. It also shows the great potential of DoE in emboldening of µPADs which makes it a step closer to commercialization. Beside these, it tries to represent the advantages of automatic image processing approach which can minimize the errors caused by manually area selection of detection zone and accelerates the color values analysis.

The obtained results show that the predictability of BBD, CCD, and D-optimal is case dependent. For example, BBD is suitable for systems with limitations or circumscribed CCD is difficult to utilize in the fabrication of µPADs. In conclusion, D-optimal design by having a better prediction and requiring a small number of the experiments rather than the other designs can be a suitable choice for next studies (Tables 2-3 and 2-4).

References

1. Martinez AW, Phillips ST, Butte MJ, Whitesides GM (2007) Patterned Paper as a Platform for Inexpensive, Low-Volume, Portable Bioassays. Angew Chem Int Ed. 46:1318–1320.

2. Avoundjian A, Jalali-Heravi M, Gomez FA (2017) Use of chemometrics to optimize a glucose assay on a paper microfluidic platform. Anal Bioanal Chem. 409:2697–2703.

3. Araujo PW, Brereton RG (1996) Experimental design III. Quantification. TrAC Trend Anal Chem. 15:156–163.

4. Asghar A, Abdul Raman AA, Daud WMAW (2014) A Comparison of Central Composite Design and Taguchi Method for Optimizing Fenton Process. The Scientific World J. 2014:1–14.

5. Longhi DA, Martins WF, da Silva NB, Carciofi BAM, de Aragão GMF, Laurindo JB (2017) Optimal experimental design for improving the estimation of growth parameters of Lactobacillus viridescens from data under non-isothermal conditions. Int J Food Microbiol. 240:57–62.

6. Dehghannasiri R, Xue D, Balachandran PV, Yousefi MR, Dalton LA, Lookman T, Dougherty ER (2017) Optimal experimental design for materials discovery. Comput Mater Sci. 129:311–322.

7. Umar S, Bakhary N, Abidin ARZ (2018) Response surface methodology for damage detection using frequency and mode shape. Measurement. 115:258–268.

8. Hamedpour V, Leardi R, Suzuki K, Citterio D (2018) Fabrication of paper-based analytical devices optimized by central composite design. Analyst. 143:2102-2108.

9. Hamedpour V, Postma GJ, van den Heuvel E, Jansen JJ, Suzuki K, Citterio D (2018) Chemometrics-assisted microfluidic paper-based analytical device for the determination of uric acid by silver nanoparticle plasmon resonance. Anal Bioanal Chem. 410:2305–2313.

10. Longhi DA, da Silva NB, Martins WF, Carciofi BAM, de Aragão GMF, Laurindo JB (2018) Optimal experimental design to model spoilage bacteria growth in vacuum-packaged ham. J Food Eng. 216:20–26.

11. Hamedpour V, Amjadi M Application of Box–Behnken Design in the Optimization of In Situ Surfactant-Based Solid Phase Extraction Method for Spectrophotometric Determination of Quinoline Yellow in Food and Water Samples. Food Anal Method. 6:1–7.

12. Montgomery DC, Fang X, Zhang C, Xu R, Xu B (2012) Design and Analysis of Experiments, 8th edition. John Wiley & Sons, Inc, Verlag GmbH & Co. KGaA.

13. Dejaegher B, Vander Heyden Y (2011) Experimental designs and their recent advances in set-up, data interpretation, and analytical applications. J Pharm Biomed Anal. 56:141–158.

14. Box GEP, Behnken DW (1960) Some New Three Level Designs for the Study of Quantitative Variables. Technometrics. 2:455–475.

15. Bezerra MA, Santelli RE, Oliveira EP, Villar LS, Escaleira LA (2008) Response surface methodology (RSM) as a tool for optimization in analytical chemistry. Talanta. 76:965–977.

16. Zolgharnein J, Shahmoradi A, Ghasemi JB (2013) Comparative study of Box-Behnken, central composite, and Doehlert matrix for multivariate optimization of Pb (II) adsorption onto *Robinia* tree leaves: Multivariate optimization. J Chemomet. 27:12–20.

17. Sarabia LA, Ortiz MC (2009) Response Surface Methodology. Comprehensive Chemometrics. Elsevier, pp 345–390.

18. Sahu PK, Ramisetti NR, Cecchi T, Swain S, Patro CS, Panda J (2018) An overview of experimental designs in HPLC method development and validation. J Pharm Biomed Anal. 147:590–611.

19. Reddaiah K, Madhusudana Reddy T, Raghu P (2012) Electrochemical investigation of L-dopa and simultaneous resolution in the presence of uric acid and ascorbic acid at a poly (methyl orange) film coated electrode: A voltammetric study. J Electroanal Chem. 682:164–171.

20. Yalgudre RS, Gokavi GS (2012) Mechanism of Oxidation of the Antituberculosis Drug Isoniazid by Bromate in Aqueous Hydrochloric Acid Medium. Ind Eng Chem Res. 51:5135–5140.

21. Wheate NJ, Vora V, Anthony NG, McInnes FJ (2010) Host–guest complexes of the antituberculosis drugs pyrazinamide and isoniazid with cucurbituril. J Inclusion Phenom Macro. 68:359–367.

22. Hong, J. I., Chang, B. Y. (2014) Development of the smartphone-based colorimetry for multi-analyte sensing arrays. Lab Chip. 14:1725−1732.

23. Otto M (2016) Chemometrics: Statistics and Computer Application in Analytical Chemistry, 3rd Edition. John Wiley & Sons, Inc, Verlag GmbH & Co. KGaA.

24. Aslan N, Cebeci Y (2007) Application of Box–Behnken design and response surface methodology for modeling of some Turkish coals. Fuel. 86:90–97.

25. Prakash Maran J, Manikandan S, Thirugnanasambandham K, Vigna Nivetha C, Dinesh R (2013) Box–Behnken design based statistical modeling for ultrasound-assisted extraction of corn silk polysaccharide. Carbohyd Polym. 92:604–611.

26. Cavazzuti M (2013) Design of Experiments. In: Optimization Methods. Springer Berlin Heidelberg, Berlin, Heidelberg, pp 13–42.

Chapter 3 A Box-Behnken design optimized μPAD for the determination of uric acid

This chapter is based on

"Chemometrics-assisted microfluidic paper-based analytical device for the determination of uric acid by silver nanoparticle plasmon resonance",

Vahid Hamedpour; Geert Postma; Edwin van den Heuvel; Jeroen Jansen; Koji Suzuki; Daniel Citterio, Analytical and Bioanalytical Chemistry, **2018**, 410, 2305-2313.

Summary

This manuscript reports on the application of chemometric methods for the development of an optimized microfluidic paper-based analytical device (μPAD). As an example, we applied chemometric methods for both device optimization and data processing of results of a colorimetric uric acid assay. Box–Behnken designs (BBD) were utilized for the optimization of the device geometry and the amount of thermal inkjet-deposited assay reagents, which affect the assay performance. Measurement outliers were detected in real time by partial least squares discriminant analysis (PLS-DA) of scanned images. The colorimetric assay mechanism is based on the on-device formation of silver nanoparticles (AgNPs) through the interaction of uric acid, ammonia, and poly(vinyl alcohol) with silver ions under mild basic conditions. The yellow color originating from visible light absorption by localized surface plasmon resonance of AgNPs can be detected by the naked eye or, more quantitatively, with a simple flat-bed scanner. Under optimized conditions, the linearity of the calibration curve ranges from 0.1–5 mmol L^{-1} of uric acid with a limit of detection of 33.9×10^{-6} mol L^{-1} and a relative standard of deviation 4.5% (n = 3 for determination of 5.0 mmol L^{-1} uric acid).

3.1. Introduction

Since their introduction in 2007, microfluidic paper-based analytical devices (μPADs) have increasingly gained-attention as low-cost health- and environmental-monitoring devices that are usable by untrained people [1–3]. They circumvent the need for sophisticated operating procedures or hardware and in general do not need any external instruments for signal readout or mechanical forces to drive flow. The wax printing method allows rapid and flexible patterning of filter paper substrates for the creation of microfluidic channels [4], whereas inkjet printing approaches can be applied to print required assay reagents in very small deposition volumes with accurate, reproducible, and high-resolution liquid placement [5].

By eliminating human error inevitability associated with manual reagent deposition, these instrumental fabrication methods contribute to the high reproducibility of the obtained devices. However, in order to achieve the best possible sensitivity with a μPAD assay, the optimization of device geometry and amounts of deposited reagents remains a challenge. Although chemometric approaches are promising tools for this purpose, their application to the optimization of μPADs is still relatively rare. Design of experiment (DoE) techniques are regarded as particularly useful, since in contrast to the traditional one-factor-at-a-time (OFAT) optimization method, they allow for the optimization of multiple factors with lower experimental effort and therefore require less time, resources, and materials [6].

DoE approaches include the study of interactions between factors, enabling evaluation of the impact of two or more factors on a final response and the prediction of optimum experimental conditions [7]. The most common designs applied for the determination of response surfaces are the central composite design (CCD), Doehlert design (DD), mixture designs, Box–Behnken design (BBD), D-optimal design, and full and fractional factorial designs [8]. There are some reports that demonstrate the application of chemometrics to paper-based substrates [9–11], but

only the application of CCD has been reported for the optimization of μPADs [12]. However, in order to simplify the optimization process, not all probable factors have been investigated. In particular, the effects of the amount of deposited assay reagents and the aspect ratio or size and shape of inlet and reservoir areas were not included in the optimization [12].

Here, a BBD was applied for optimization of the device geometry and the amount of deposited reagents, while considering all effective factors. According to a theoretical comparison, a BBD is more efficient than a CCD and the estimation of all linear effects, two-way interactions, and quadratic effects is possible by fewer experiments [13]. A BBD is a second-order rotatable (or nearly rotatable) three-level incomplete factorial design [14], which is composed of a center point, and points that are located on the middle of the cube edges [15]. This feature can be beneficial when it is not possible to check the points on the corners as a result of experimental constraints or cost. In the case of knowing experimental limits of factors, BBD can be especially useful. Star points (α) in CCD are usually located outside of the region of interest, where it is impossible to conduct experiments, because they are beyond the acceptable levels. Since star points are not included in BBD, all desired points will be within the defined levels [16].

The chemometrics-assisted μPAD optimization in the current study is demonstrated on a model device targeting the detection of uric acid (UA), which is the major metabolite of purines in human biofluids such as urine and blood. The normal concentration of UA in healthy human's urine is around 2 mM [17]. Altered concentrations can cause various abnormalities and diseases, among which are nephritis, gout, deposition of crystals of monosodium urate in cartilage, synovium, and synovial fluid of joints, Lesch–Nyhan syndrome, type 2 diabetes, kidney disorder, and hypertension [18].

Over the last few years, several detection methods including the use of nanoparticles (NPs) have been applied on μPADs. Metal nanostructures, particularly gold nanoparticles (AuNPs) and silver nanoparticles (AgNPs), have unique and favorable properties, such as the unique optical behavior used in localized surface plasmon resonance (LSPR) [19, 20]. This arises from the interaction of the oscillating light electromagnetism with the free electrons of metal NPs, which induces a collective coherent oscillation with respect to the positive metallic lattice that resonates at a specific frequency of visible light [19]. The particular wavelength of the LSPR depends on size, shape, and agglomeration state of the nanoparticles [21].

In recently published works, uric acid assay methods based on the LSPR absorption of nanoparticles[22, 23], enzymatic methods [24], and methods based on AgNPs in combination with enzymes have been reported [25]. However, enzymatic determination of UA involves the use of relatively costly and potentially unstable enzymes that might contribute to a decrease in analytical reproducibility. Non-enzymatic UA assay methods, where UA acts as a reducing agent for the generation of AgNPs [22], may be very well integrated into colorimetric paper-based microfluidic detection through the plasmon resonance of silver nanoparticles. Although the detection principle is known, its application to paper-based devices has not been reported to date, despite the favorable properties of enzyme-free μPADs in terms of cost-effectiveness and stability.

The aim of the present study is to demonstrate the application of chemometrics in the development of a colorimetric μPAD assay for uric acid in order to achieve an efficient device with a minimum number of optimization-related experiments and low consumption of reagents. Chemometric methods are applied to all relevant assay development steps ranging from device fabrication optimization, image, and data analysis, as well as an automatic procedure for outlier detection. To the best of our knowledge, this is the first report on the application of a Box–Behnken design for the optimization of a μPAD, which covers all probable effective factors

including device geometry and the amount of deposited assay reagents. Finally, the μPAD-based determination of uric acid in urine samples is demonstrated.

3.2. Experimental section

3.2.1. Standard solutions and reagents

All chemicals were used without any further purification. A stock standard solution of UA (5 mmol L^{-1}) was prepared by dissolving the appropriate amount of UA (Wako, Osaka, Japan) in a minimum volume of 0.1 mol L^{-1} NaOH and diluting with ultra-pure water. A stock solution of poly(vinyl alcohol) (PVA; 2.8 g L^{-1}) was prepared by dissolving 0.28 g of PVA (Kanto, Tokyo, Japan) in ultra-pure water and diluting to 100 mL. Also, 1.0% (w/v) NaOH (Wako) and 0.5 mol L^{-1} NH_3 (Wako) solutions were used. The stock solution of $AgNO_3$ (0.01 mol L^{-1}) was prepared by dissolving the required amount of $AgNO_3$ (Wako) in ultra-pure water.

3.2.2. Instrumentation

Ultra-pure water was prepared by a PURELAB flex set (Veolia, Paris, France). Microfluidic patterns were printed by a ColorQube 8570 wax printer (Xerox, Norwalk, CT, USA). Deposition of reagents (PVA, NaOH, NH_3, and $AgNO_3$) was done by using a thermal Canon ip2700 inkjet printer (Canon, Tokyo, Japan). For this purpose, the standard Canon printer's black cartridges were cut open and, after removing the inside sponges, the cartridge was washed with ultra-pure water and dried completely. Finally, 2 mL of each solution to deposit was placed into separate cartridges.

3.2.3. Device fabrication

A schematic outline of a single device consisting of three square areas for filtration (D), sample application (A), pH adjustment (B), and colorimetric signal detection (C) connected by two channels is shown in Fig. 3-1. First, filter paper (Whatman grade 1, GE Healthcare, Buckinghamshire, UK) was cut into A4 size, then fed into the wax printer to fabricate the microfluidic pattern. The pattern was designed with Microsoft PowerPoint and printed on the topside of the filter paper. After printing, the paper was heated at 150°C on a hot plate (NHS-450ND, Nissin Co., Tokyo, Japan) for 1min to let the wax diffuse into the thickness of the paper. Afterward by using a hot laminator (QHE325, Meikoshokai Co., Ltd., Tokyo, Japan), the backside of the paper was covered with a hot lamination film (150 μm thickness). Before the inkjet printing step, the laminated paper was cut to A4 size again to allow it to pass through the paper feeding mechanism of the inkjet printer. Then, PVA solution was deposited on the entire hydrophilic area in 19 printing cycles, followed by 11 printing cycles of NaOH solution into the second square area (B) and finally 11 and 19 printing cycles of NH_3 and $AgNO_3$ solutions, respectively, into sensing area (C). As the final step, the on-device titration unit (Fig. 3-1b) was mounted on top of the paper.

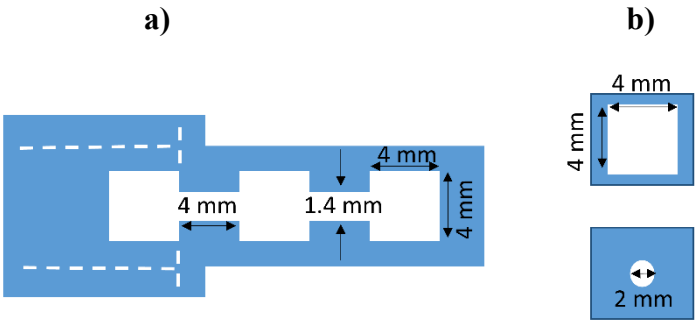

Figure 3-1. Schematic outline of a single printed device: a) microfluidic channel outline for colorimetric UA determination; b) separate wax-patterned paper for on-device chloride titration.

3.2.4. Uric acid determination in urine samples

A normal urine sample was collected from a healthy volunteer using a disposable polyethylene centrifuge tube (VIOLAMO, Sigma) and stored in a refrigerator until use. To prevent chloride interferences, an on-device titration step was performed. For this purpose, first 14.0 μL of urine sample was added to the filtration area (D) (No. 5C, ADVANTEC, Toyo Roshi Ltd., Japan), followed by an excess amount of AgNO3 (3.5 μL of 1.0 M solution), larger than the highest possible concentration of chloride reported for urine samples [26], to completely remove chloride from the sample. Finally, the excess amount of silver ions was precipitated by gradually adding 1.0% (w/v) NaOH solution, until the color of the titrated urine sample remained dark brown without any changes, indicating complete removal of silver ions. After this step, the on-device titration filter paper (D) was slid over to the sampling area (A), to let the sample flow through the device up to the signal detection area (C). The on-device titration procedure is schematically shown in Fig. 3-2, together with photographs of a device before sample application (Fig. 3-2a, bottom) and after titration and sliding to the sampling area (Fig. 3-2b, bottom).

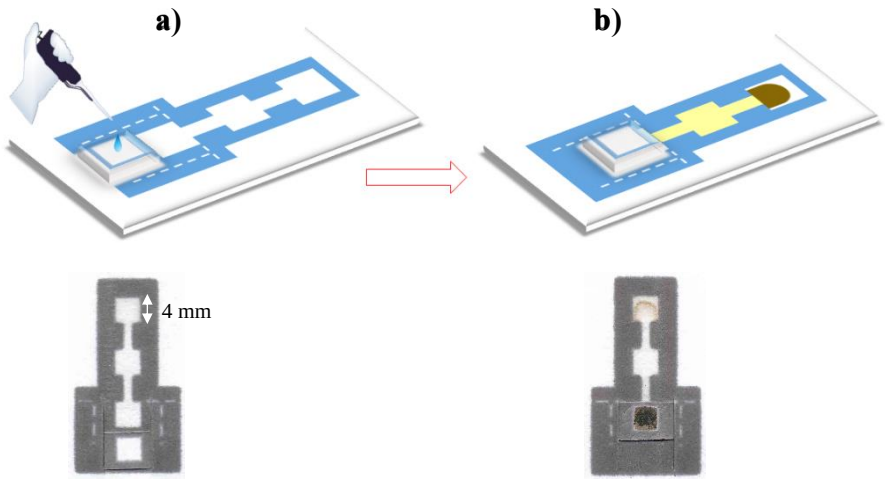

Figure 3-2. Outline of the on-device titration for chloride removal on a single microfluidic pattern: a before sample application; b after titration and sliding of filtration paper.

3.2.5. Experimental strategy

In the current work, a Box–Behnken design (BBD) was selected for optimization of the μPAD geometry and the amount of assay reagents deposited onto the paper substrate. The latter is reflected by the number of inkjet printing cycles of the various reagent solutions. For the current μPAD, a "three area" design was selected (indicated as areas A, B, and C in Fig. 3-1) because of the chemical incompatibility between different reagents. For example, in the case of printing NaOH and $AgNO_3$ in the same area of a μPAD, an undesired reaction between both reagents occurs, and the color changes to dark brown, so that the device is no longer usable. The first area (A) was required for overlaying with the additional titration area for on-device chloride removal (Fig. 3-1b). Two types of variables were optimized: (a) variables related to the μPAD geometry, i.e., fluidic channel length and width, area length and width, and sampling volume; (b) variables related to the chemistry, i.e., the numbers of inkjet printing cycles of PVA, NaOH, NH_3, and $AgNO_3$ reagent solutions.

On the basis of preliminary test results, it was identified that all nine selected factors have quantifiable impacts on maximizing the color intensity in the signal detection area. Therefore, a screening step, which is mostly used for reduction of the probable factors, was omitted and the response surface methodology (RSM) was applied for optimization of the experimental conditions directly. Since simultaneous optimization of all nine factors is a very complex procedure and requires a large number of experiments, the nine factors were divided into two groups. The first group includes the number of printing cycles of the reagents, and the second one consists of factors related to device geometry. The effect of interaction between those two groups of variables on the color intensity was assumed to be small. In the first step, the number of printing cycles of the reagents was optimized, while levels of the pattern geometry were fixed at the middle points. Then, by knowing the optimized levels of the first group of factors, the device geometry was optimized. Finally, verification experiments were carried out to check

the validity of the above assumption of limited interaction effects between the two groups of factors. For this purpose, at the optimal pattern geometry, the optimization step of the first group of factors was repeated, and the results of this step were compared with the previously obtained results. The experimental designs were set up and analyzed using Statgraphics centurion XVII Package (ver. 17.2.00) software.

3.2.6. Experimental strategy

The images of the device were scanned by a commercially available office scanner (CanoScan 9000F MARK II color scanner, Canon, Tokyo, Japan) 22 min after calibration sample application or sliding of the on-device titration paper area. Then, an image of the sensing area of each device with dimension of 81 × 81 pixels was selected and transferred to a MATLAB environment (MATLAB 9.2, The Mathworks Inc., Natick). The resulting RGB color values (red, green, and blue, respectively) may be arranged in 3 × 81 × 81 arrays. Each sample was corrected for the blank by subtracting the matrix of the blank image from the corresponding sample image (Fig. 3-3). The blue color coordinate value was most appropriate for use in the subsequent analyses, since it showed the largest dynamic range.

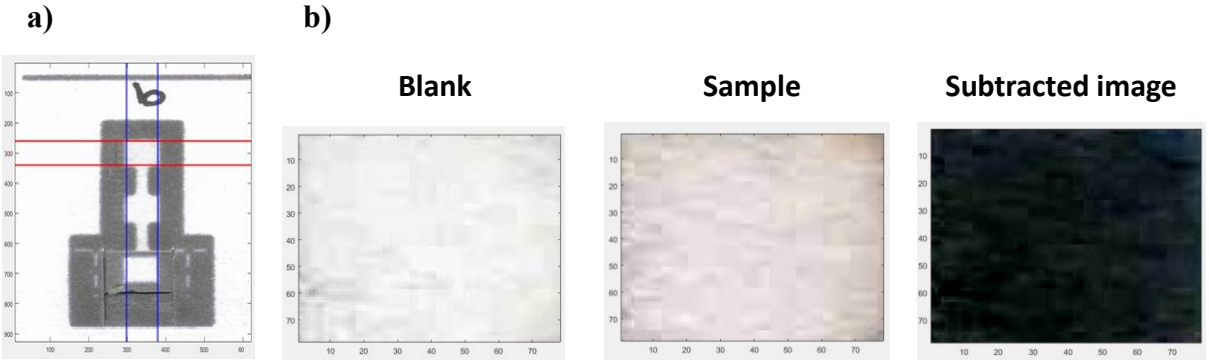

Figure 3-3. a) A manually selected area by MATLAB software for image processing; b) equally selected areas (81 × 81 pixels) for blank and sample, and accordingly subtracted image. According to the profile of the subtracted image, a boundary shape representing the response was not seen, and therefore it was selected as an outlier.

The main reason for using a scanner instead of, for example, a smartphone for signal readout is that smartphone-based approaches face challenges induced by environmental light conditions, which are not trivial to overcome [27]. Since in the current study, the focus was on the chemometrics to optimize device geometry and assay reagent amounts, reproducible acquisition of colorimetric data is of high importance to reliably reflect the effect of the variables of interest. This is guaranteed by the controlled lighting environment in an office scanner. An automated outlier detection procedure based on partial least squares discriminant analysis (PLS-DA) with manually executed double cross-validation was implemented (PLS Toolbox with MIA Toolbox 8.2.1 (2016) Eigenvector Research, Inc., Manson, WA USA 98831; http://www.eigenvector.com) to exclude obvious outliers. In this procedure, a classification model ($y = X \cdot b$) is built in PLS-DA, enabling the prediction and classification of a desired factor, such as the sample class (included in vector y) from measured variables (included in matrix X). In this work, the scanned blue color images of the device sensing areas are the measured variables. By mean scaling each image and applying PLS-DA on the obtained data, the focus was set on the image profile instead of the blue color intensity. Forty measurements were used to construct the PLS-DA model for outlier detection: ten replicate measurements of four urine samples with four different UA concentrations (Table 3-1).

Table 3-1. Determination of uric acid in human urine by μPAD.

Sample	UA added (mmol L^{-1})	UA found (mmol L^{-1})	Recovery(%)
Urine	-	1.55 ± 0.15	-
	0.5	2.14 ± 0.11	104.4
	1.0	2.41 ± 0.14	94.9
	1.5	2.76 ± 0.24	90.7

In order to validate the model, a four-step double cross-validation procedure was performed. In each step, the measurements of three groups of ten measurements (belonging to three

samples) were selected as a training set, and the remaining replicate measurements were selected as a test set. The training data were used for the determination of the number of latent variables by means of an embedded cross-validation. The number of latent variables was 12. Autoscaling was applied to the data each time.

3.3. Results and discussion

3.3.1. In-situ formation of silver nanoparticles

From previous studies, it is known that UA at relatively high concentrations can cause reduction of the $[Ag(NH_3)_2]^+$ complex ions to silver nanoparticles, similar to the Tollens process used for AgNPs synthesis [22]. In this process, it is not possible to obtain AgNPs from a silver salt like $AgNO_3$ by addition of NaOH alone, even after prolonged reaction time, but by using $[Ag(NH_3)_2]^+$ as the oxidant in the presence of NaOH, AgNPs are formed [28]. Moreover, the PVA used as a capping agent provides effective stabilization of formed AgNPs and increases the absorbance [29, 30]. The LSPR absorption resulting from in situ AgNPs formation appears as a yellowish color on the filter paper substrate (Fig. 3-4).

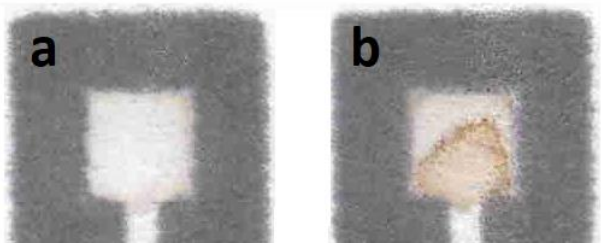

Figure 3-4. Detection zone of a device, after exposure to a) ultra-pure water, and b) uric acid (5 mM).

Similar to previously reported work, the formation of AgNPs inside the cellulosic fiber network of the filter paper was verified by scanning electron microscopy (SEM) [31]. Fig. 3-5 shows

SEM images of cellulosic fibers inside the colorimetric signal detection area of a paper-based device after application of pure water (Fig. 3-5a) or an aqueous uric acid standard sample (Fig. 3-5b). The reduction of Ag^+ by UA resulted in formation of AgNPs, as indicated by the changes in surface morphology and image contrast of the cellulose fibers (Fig. 3-5b, c).

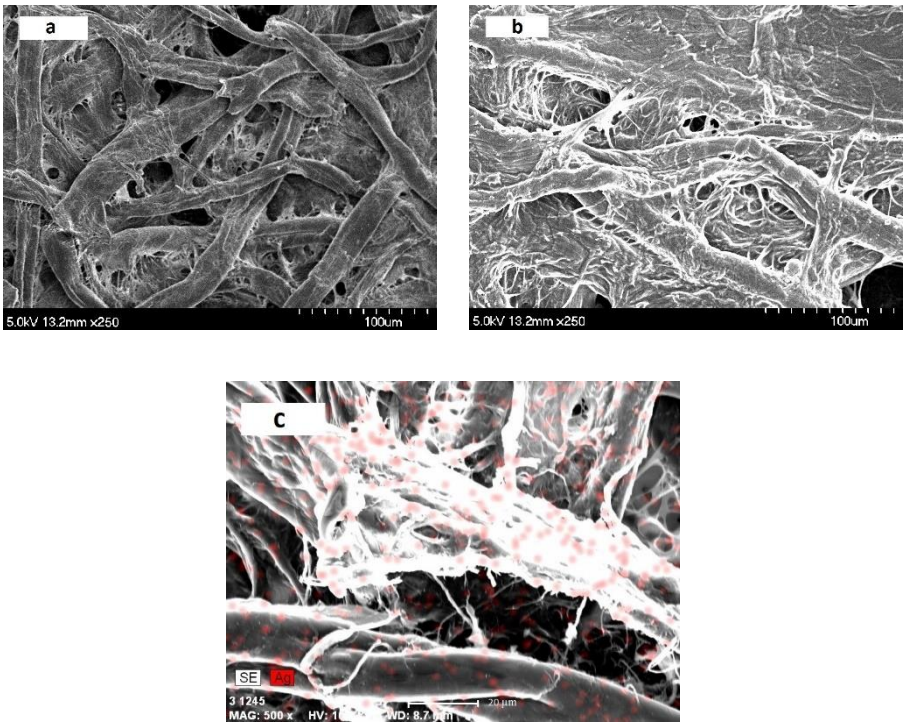

Figure 3-5. Representative SEM and EDX (energy dispersive X-ray analysis) images (×250 and ×500 magnification) of a the μPAD after exposure to ultra-pure water; b the μPAD after exposure to uric acid (5 mM); and c EDX image after exposure to uric acid.

Allantoin (a water-soluble compound) is the main product of the chemical, enzymatic, or electrochemical oxidation of uric acid in neutral and basic media [32, 33]. Thus, the overall reaction of the current system might be proposed as shown in Fig. 3-6 [22].

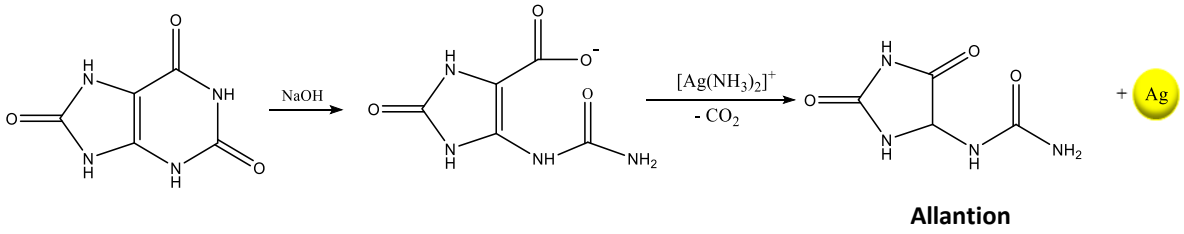

Figure 3-6. Overall reaction between uric acid and silver ions leading to formation of AgNPs.

3.3.2. Optimization strategy

In the current study, in order to select an appropriate optimization model and investigate the factors and their levels, initial experiments were carried out. According to the obtained results, working at very high or very low levels was not suitable. For example, working at very basic pH conditions, corresponding to a large number of NaOH printing cycles, uric acid concentration-independent color changes were obtained, whereas no colorimetric signal was observed at neutral pH values, corresponding to low number of printing cycles of NaOH. This problem arises from the chemistry behind the sensing mechanism, which does not proceed under the extremes of very basic or near-neutral pH conditions (e.g., amounts of NaOH and NH_3). Since in central composite design (CCD), not only corner points but also star points are problematic, some of the designated experiments are not possible from a chemistry viewpoint. Hence, for preventing these problems, Box–Behnken design (BBD) was the best choice, because it avoids combinations that are extreme. In the optimization of μPAD geometry, a BBD in two blocks consisting of 46 experiments with three center points in each block, and in the case of optimizing the number of printing cycles, a three block-BBD consisting of 27 experiments with a center point in each block were run in order to define the optimum conditions. The selected levels of each factor in both cases are shown in Tables 3-2 and 3-3.

Table 3-2 Experimental variables and levels of the BBD for optimizing the μPAD geometry.

Variable	symbols	Level		
		-1	0	+1
Channel length (mm)	A	4.0	5.0	6.0
Channel width (mm)	B	0.6	1.0	1.4
Area length (mm)	C	3.0	3.5	4.0
Area width (mm)	D	3.0	3.5	4.0
Sampling volume (μL)	E	5.0	10.0	15.0

Table 3-3. Experimental variables and levels of the BBD for optimizing the number of printing cycles of reagent solutions required for the UA detecting μPAD.

Variable	symbols	Level		
		-1	0	+1
PVA	A	5	12	19
NaOH	B	5	12	19
NH_3	C	5	8	11
$AgNO_3$	D	5	12	19

The relationship between the blue color intensity (CI) in the signal detection area and the factors (as coded values) are fitted with the following equations: Eq. 3-1 describes the results from the second μPAD geometry optimization, and Eq. 3-2 the optimization of number of printing cycles:

$$CI = -58.62 + 9.57(A) + 56.30(B) - 5.01\ (C) + 2.33(D) + 6.50\ (E) - 8.19(AB) - 0.55(AE) - 17.63\ (B)^2 + 8.75(BC) - 0.11\ (E)^2 \quad \text{Eq. 3-1}$$

$$CI = 26.84 - 4.20(A) + 1.04(B) + 2.42\ (C) + 0.37\ (D) + 0.30(AC) + 0.19\ (AD) - 0.0543367(B)^2 - 0.33(C)^2 - 0.06\ (D)^2 \quad \text{Eq. 3-2}$$

In this work, the equations together with the Pareto charts (Figs. 3-7 and 3-9) are used to find the effective variables, and in both equations non-significant variables were discarded. According to the Pareto chart (Fig. 3-7), it is obvious that the sampling volume (denoted as E) has the highest effect and shows a positive impact on color intensity. On the other hand, the channel length (B), area length (C), and area width (D) also show positive impact, whereas channel width (A) shows a negative impact (Fig. 3-8). In addition, the investigation of the quadratic effects and interactions showed that the quadratic effects of sampling volume (EE) and channel width (BB), the interactions between channel length and channel width (denoted as AB), channel length and sampling volume (AE), and channel width and area width (BC) are

important. A similar explanation about the order of the non-significant factors and their positive or negative impact can be given.

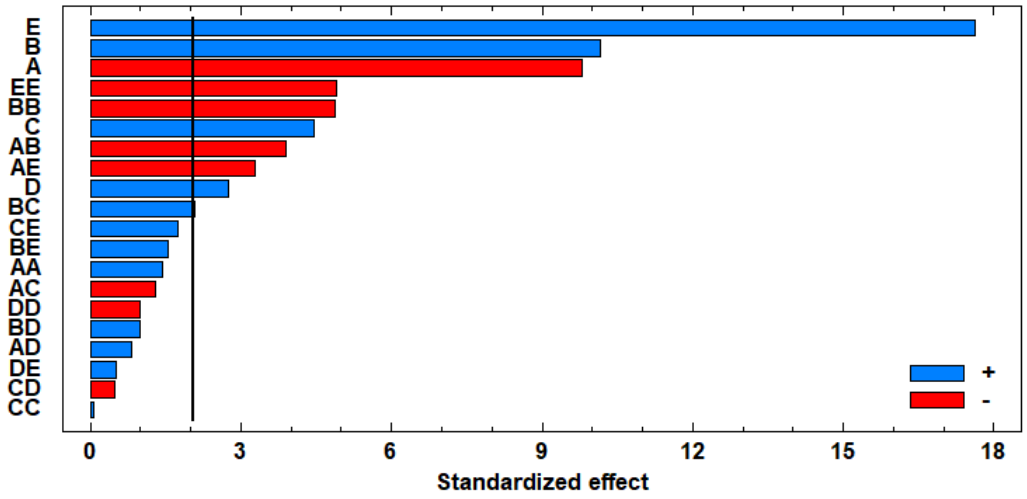

Figure 3-7. Pareto chart of the main effects obtained from optimizing µPAD geometry for UA detection devices. For meaning of the coded parameters, please refer to Table 3-2. AA, BB, CC, DD and EE are the quadratic effects of channel length, channel width, area length, area width and sampling volume. AB, AC, AD, AE, BC, BD, BE, CD and CE are the interaction effects.

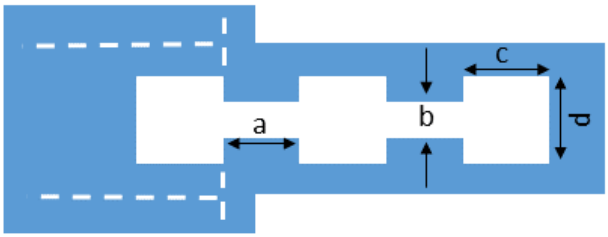

Figure 3-8. Representative µPAD with device geometry variables: a) channel length; b) channel width; c) area length; and d) area width.

According to the Pareto chart for the number of printing cycle's (Fig. 3-9), $AgNO_3$ (denoted as D) has the highest effect with a positive impact. As it is shown, PVA (A) and NH_3 (C) also have positive impacts, but NaOH (A) shows a negative impact. In addition, the evaluation of the quadratic and interaction effects showed that the quadratic effect of NH_3 (CC), $AgNO_3$ (DD), and NaOH (BB), and the interaction between PVA and $AgNO_3$ (denoted as AD), as well as PVA and NH_3 (AC), are effective.

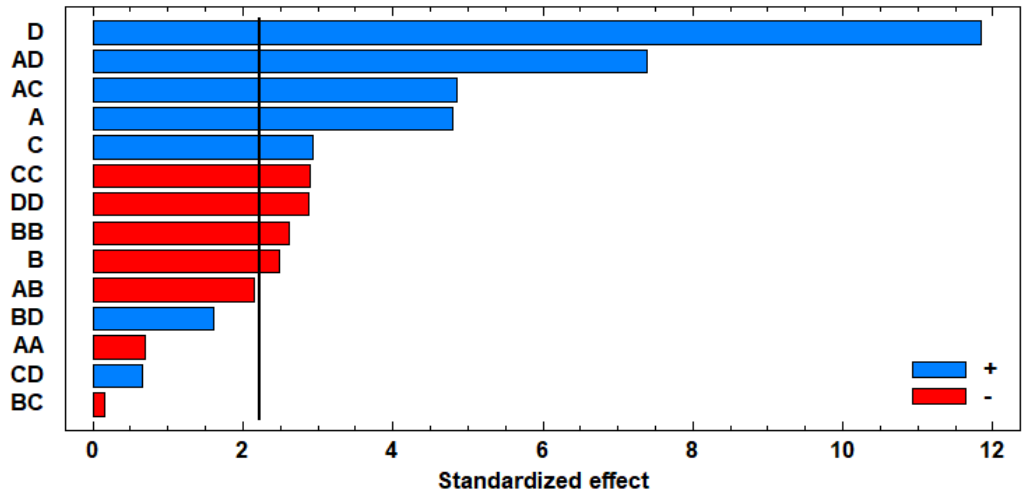

Figure 3-9. Pareto chart of the main effects obtained from optimizing the number of inkjet printing cycles of the reagent solutions for UA detection devices. For meaning of the coded parameters, please refer to Table 3-3. AA, BB, CC and DD are the quadratic effects of printing cycles of PVA, NaOH, NH_3 and $AgNO_3$. AB, AC, AD, BC, BD and CD are the interaction effects.

The verification experiments showed no drastic changes in recommended optimum experimental conditions or insignificance of the factors in the Pareto charts. All of these facts prove that neglecting the probable interactions between the first and second group of factors was a suitable strategy, and by doing so saved not only time and costs but avoided performing complex experiments. The experimental matrix of both groups were reported in Appendix Chapter 3 Tables 3-1and 3-2.

Finally, on the basis of the experimental designs and the resulting equations, the optimal settings of the factors were chosen as channel length 4.0 mm, channel width 1.4 mm, area length 4.0 mm, area width 4.0 mm, sampling volume 14.0 μL, PVA 19 printing cycles, NaOH 11 printing cycles, NH_3 11 printing cycles, and $AgNO_3$ 19 printing cycles.

3.3.3. Outlier classification by PLS-DA model

Some outliers, mostly originating from inappropriate reagent deposition by the printer, on-device titration step problems, sample leakage from the extra titration paper, fluidic channel

blockage or other causes, were inevitably observed. In practice, on average, each set of 10 replicate measurements contained three erroneous measurements (outliers). A PLS-DA classification model was built, based on the image profiles of the signal detection areas of the μPADs for automatically predicting successful measurements. Forty measurements were used to construct the PLS-DA model: ten replicate measurements of four urine samples with four different concentrations (Table 3-1). According to the binomial distribution calculations (Eq. 3-3), the probability of obtaining three reliable results per seven replications is around 96% and the probability of achieving six reliable results among ten replications is 99.7% (Table 3-4).

$$b(x; n, P) = {}_nC_x \times P^x \times (1 - P)^{n-x} \qquad \text{Eq. 3-3}$$

$${}_nC_x = \frac{n!}{(n-x)!x!} \qquad \text{Eq. 3-4}$$

where b is binomial probability, x represents total number of "successes" (pass or fail, heads or tails), P lies probability of a success on an individual trial, and n is total number of trials.

Therefore, to obtain more reliable results, ten replications were chosen. Double cross-validation (CV) showed that the PLS-DA model of the 40 urine measurements could detect the outliers in all cases correctly, which proves the validity of the built model and classification procedure (Fig. 3-10).

Table 3-4. Binomial distribution test results for probable conditions.

Observed reliable results	Probability of success on a single trial (P)	Total number of trials (n)	Cumulative probability P (X ≥ x)
1	0.675	5	0.80231
2	0.675	6	0.90789
3	0.675	7	0.95936
4	0.675	8	0.98277
5	0.675	9	0.99292
6	0.675	10	0.99716

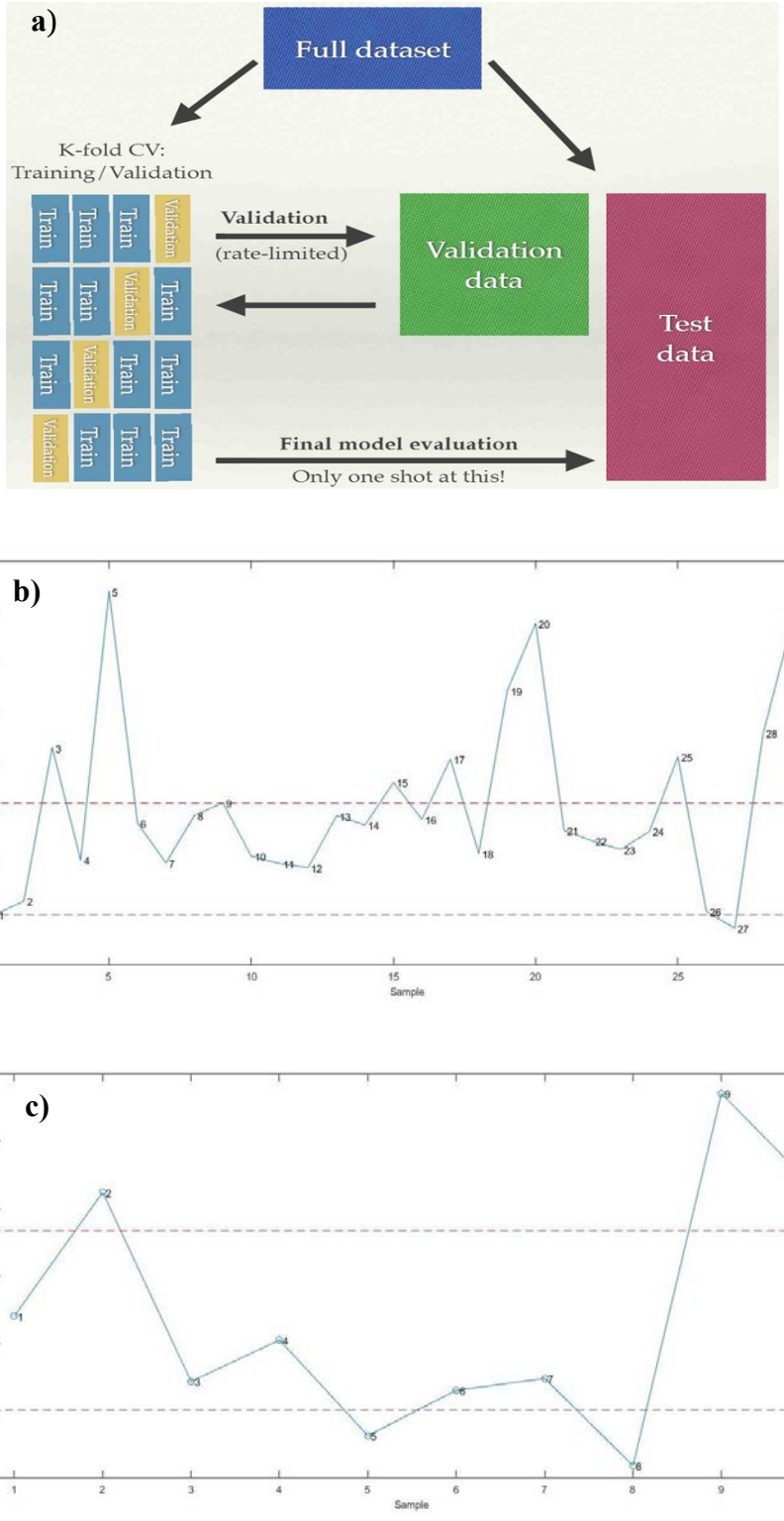

Figure 3-10. a) Schematic representation of double cross-validation (CV). In each step, three of four urine samples were selected as a train-set and prediction model was built on them, and the remained sample was used as a test set (validation set). By projection of test-set matrix to the prediction model, outliers were successfully detected. The class 1 representing the acceptable data (below the red line), and class 2 representing the outliers (upper the red line); b) prediction of the outliers inside the train-set; and c) prediction of the outliers inside the train-set after projection to the model.

3.3.4. Interference study

For this purpose, the determination of 5.0 mmol L^{-1} uric acid in the presence of some potentially interfering substances was examined. The tolerance limits for diverse ions and organic substances was determined as the interfering species concentration that causes less than ± 5% relative error on the UA concentration estimation. The tolerance limits for analyte ratios were over 500 for NO^{3-}, Na^{+}, and K^{+}; 100 for SO_4^{2-} and urea; 50 for Mg^{2+}, Ca^{2+}, and NH^{4+}; 10 for PO_4^{3-}, fructose, glucose, and sucrose; 5 for citric acid; and 1 for ascorbic acid and Cl^{-} (in absence of the on-device titration step). The presence of chloride results in the precipitation of silver ions and consequently UA concentration-dependent color changes no longer occur. The on-device removal of all chloride prior to the on-device colorimetric assay circumvents this influence.

3.3.5. Analytical figures of merit

The relation between the blue color intensity in the signal detection area and the UA concentration under the optimal conditions was evaluated by using UA standard solutions with a 200 mM background of NaCl. Under the optimum conditions, the linearity of the calibration curve is in the range of 0.1–5 mmol L^{-1} with a correlation coefficient of 0.994 (Fig. 3-11). The relative standard deviation (n = 3 for the determination of 5.0 mmol L^{-1} uric acid) and the detection limit were estimated to be 4.5% and 33.9×10^{-6} mol L^{-1}, respectively.

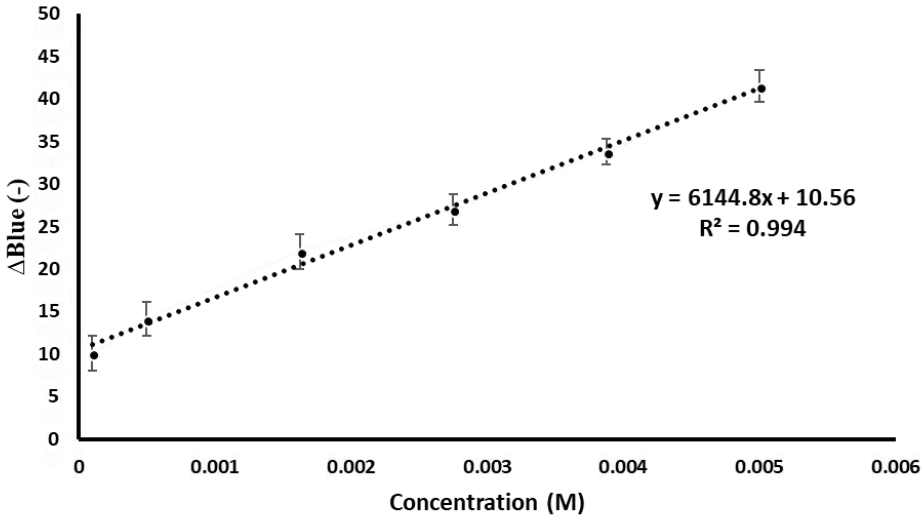

Figure 3-11. Calibration curve for uric acid determination on an optimized µPAD including on-device chloride removal (n=3); the aqueous uric acid standard samples include a background of 200 mM of NaCl.

3.3.6. Application to real sample

To demonstrate a simple model application, the optimized devices were employed for the determination of the UA levels in human urine samples. For evaluating the accuracy of the proposed method, recovery tests were performed with uric acid spiked human urine samples. The obtained results are shown in Table 3-1. The recoveries ranged from 104.4% to 90.7%, showing the capability of this device to determine uric acid in urine samples. The proposed method was compared to some earlier reported methods (Table 3-5). It should be mentioned that the method presented here, although representing a low-cost approach, is a simple and convenient way for determination of UA, since the linear response range encloses the clinically relevant range of UA, making a dilution step unnecessary.

Table 3-5. Figures of merits of other reported methods for determination of uric acid

Method	Linear range (mol L^{-1})	LOD (mol L^{-1})	Ref.
Colorimetric	NA	5.0×10^{-7}	[23]
Chemiluminescence	3.0×10^{-8}- 3.0×10^{-6}	3.0×10^{-8}	[34]
Electrochemical	10×10^{-6}- 26×10^{-6}	0.2×10^{-6}	[35]
HPLC	1.2×10^{-6}- 5.9×10^{-4}	NA	[36]
LC-MS	3.5×10^{-5}- 1.2×10^{-3}	9.5×10^{-8}	[37]
Fluorimetry	0.22×10^{-6}- 6.0×10^{-6}	0.10×10^{-6}	[38]
AgNPs-based	1.0×10^{-8}- 2.0×10^{-7}	3.3×10^{-9}	[22]
μPAD-AuNPs	NA	4.8×10^{-5}	[39]
PAD-SERS	0-0.35×10^{-3}	0.11×10^{-3}	[10]
μPAD-AgNPs	1.0×10^{-4}- 5.0×10^{-3}	33.1×10^{-6}	Present work

3.4. Conclusions

The present work aimed to demonstrate the possibility of applying chemometric methods to all steps of μPAD assay development, including device optimization, data analysis, and image processing. The design of experiment (DoE) approach contributed to a reduction of the total amount of required experiments and therefore savings in cost and time. Box–Behnken designs of a nine-factor system consisting of a total of 73 experiments were utilized for the optimization of both device geometry and assay reagent amounts. In the data analysis step, a partial least squares discriminant analysis (PLS-DA) based on image profiles was successfully implemented as an automatic procedure for outlier classification.

The μPAD developed in this study primarily served the purpose of a simple model to demonstrate the possibilities of the applied chemometric methods. Despite its simplicity, it allows the determination of uric acid without the requirement for sophisticated laboratory instruments and with low consumption of sample liquid and assay reagents, as has been demonstrated by the reasonable recovery of uric acid spiked into real urine samples.

References

1. Martinez AW, Phillips ST, Butte MJ, Whitesides GM (2007) Patterned Paper as a Platform for Inexpensive, Low-Volume, Portable Bioassays. Angew Chem Int Ed. 46:1318–1320.

2. Cate DM, Adkins JA, Mettakoonpitak J, Henry CS (2015) Recent Developments in Paper-Based Microfluidic Devices. Anal Chem. 87:19–41.

3. Yamada K, Shibata H, Suzuki K, Citterio D (2017) Toward practical application of paper-based microfluidics for medical diagnostics: state-of-the-art and challenges. Lab Chip. 17:1206–1249.

4. Carrilho E, Martinez AW, Whitesides GM (2009) Understanding Wax Printing: A Simple Micropatterning Process for Paper-Based Microfluidics. Anal Chem. 81:7091–7095.

5. Yamada K, Henares TG, Suzuki K, Citterio D (2015) Paper-Based Inkjet-Printed Microfluidic Analytical Devices. Angew Chem Int Ed. 54:5294–5310.

6. Czitrom V (1999) One-Factor-at-a-Time versus Designed Experiments. Ame Stat. 53:126–131.

7. Jalali-Heravi M, Arrastia M, Gomez FA (2015) How Can Chemometrics Improve Microfluidic Research? Analy Chem. 87:3544–3555.

8. Ferreira SLC, Bruns RE, da Silva EGP, dos Santos WNL, Quintella CM, David JM, de Andrade JB, Breitkreitz MC, Jardim ICSF, Neto BB (2007) Statistical designs and response surface techniques for the optimization of chromatographic systems. J Chromatogr A. 1158:2–14.

9. Pumtang S, Siripornnoppakhun W, Sukwattanasinitt M, Ajavakom A (2011) Solvent colorimetric paper-based polydiacetylene sensors from diacetylene lipids. J Colloid Interf Sci. 364:366–372.

10. Villa JEL, Poppi RJ (2016) A portable SERS method for the determination of uric acid using a paper-based substrate and multivariate curve resolution. Analyst. 141:1966–1972.

11. Shariati-Rad M, Irandoust M, Mohammadi S (2016) Multivariate analysis of digital images of a paper sensor by partial least squares for determination of nitrite. Chemometr Intell Lab. Systems 158:48–53.

12. Avoundjian A, Jalali-Heravi M, Gomez FA (2017) Use of chemometrics to optimize a glucose assay on a paper microfluidic platform. Anal Bioanal Chem. 409:2697–2703.

13. Zolgharnein J, Shahmoradi A, Ghasemi JB (2013) Comparative study of Box-Behnken, central composite, and Doehlert matrix for multivariate optimization of Pb (II) adsorption onto *Robinia* tree leaves: Multivariate optimization. J Chemometr. 27:12–20.

14. Box GEP, Behnken DW (1960) Some New Three Level Designs for the Study of Quantitative Variables. Technometrics. 2:455–475.

15. Bezerra MA, Santelli RE, Oliveira EP, Villar LS, Escaleira LA (2008) Response surface methodology (RSM) as a tool for optimization in analytical chemistry. Talanta. 76:965–977.

16. Jun S, Irudayaraj J, Demirci A, Geiser D (2003) Pulsed UV-light treatment of corn meal for inactivation of Aspergillus niger spores. Int J Food Sci Tech. 38:883–888.

17. Popa E, Kubota Y, Tryk DA, Fujishima A (2000) Selective Voltammetric and Amperometric Detection of Uric Acid with Oxidized Diamond Film Electrodes. Anal Chem. 72:1724–1727.

18. Pradhan T, Maiti S, Kumar R, Lee YH, Kim JW, Lee JH, Kim JS (2015) Rationally designed non-enzymatic fluorogenic 'turn-on' probe for uric acid. Dyes Pigments. 121:1–6.

19. Jain PK, Huang X, El-Sayed IH, El-Sayed MA (2008) Noble Metals on the Nanoscale: Optical and Photothermal Properties and Some Applications in Imaging, Sensing, Biology, and Medicine. Acc Chem Res 41:1578–1586.

20. Cobley CM, Skrabalak SE, Campbell DJ, Xia Y (2009) Shape-Controlled Synthesis of Silver Nanoparticles for Plasmonic and Sensing Applications. Plasmonics. 4:171–179.

21. Mock JJ, Barbic M, Smith DR, Schultz DA, Schultz S (2002) Shape effects in plasmon resonance of individual colloidal silver nanoparticles. J Chem Phys. 116:6755–6759.

22. Amjadi M, Rahimpour E (2012) Silver nanoparticles plasmon resonance-based method for the determination of uric acid in human plasma and urine samples. Microchim Acta. 178:373–379.

23. Bera RK, Anoop A, Raj CR (2011) Enzyme-free colorimetric assay of serum uric acid. Chem Commun. 47:11498–11500.

24. Li X, Liu X (2014) Fabrication of three-dimensional microfluidic channels in a single layer of cellulose paper. Microfluid Nanofluid. 16:819–827.

25. Zhao C, Thuo MM, Liu X (2013) A microfluidic paper-based electrochemical biosensor array for multiplexed detection of metabolic biomarkers. Sci Technol Ad Mat. 14:054402.

26. Heil W, Mahato Ranges for Adults and Children: Pre-Analytical Considerations. 9th Ed. Roche Diagnostics GmbH; 2008. https://www.rochediagnostics.fr/htdocs/media/pdf/actualites/2a_reference_ranges_2008.pdf (last accessed 08 May 2017)

27. Martinez AW, Phillips ST, Carrilho E, Thomas SW, Sindi H, Whitesides GM (2008) Simple Telemedicine for Developing Regions: Camera Phones and Paper-Based Microfluidic Devices for Real-Time, Off-Site Diagnosis. Anal Chem. 80:3699–3707.

28. Wu LP, Li YF, Huang CZ, Zhang Q (2006) Visual Detection of Sudan Dyes Based on the Plasmon Resonance Light Scattering Signals of Silver Nanoparticles. Anal Chem. 78:5570–5577.

29. Sharma VK, Yngard RA, Lin Y (2009) Silver nanoparticles: Green synthesis and their antimicrobial activities. Adv Colloid Interfac. 145:83–96.

30. Yin Y, Li Z-Y, Zhong Z, Gates B, Xia Y, Venkateswaran S (2002) Synthesis and characterization of stable aqueous dispersions of silver nanoparticles through the Tollens processElectronic supplementary information (ESI) available: photographs of silver mirror,

and of stable dispersions of silver nanoparticles from mixing diluted silvering solutions under sonication at various times. J Mater Chem. 12:522–527.

31. Pourreza N, Golmohammadi H, Naghdi T, Yousefi H (2015) Green in-situ synthesized silver nanoparticles embedded in bacterial cellulose nanopaper as a bionanocomposite plasmonic sensor. Biosens Bioelectron. 74:353–359.

32. Sampat R, Young S, Rosen A, Bernhard D, Millington D, Factor S, Jinnah HA (2016) Potential mechanisms for low uric acid in Parkinson disease. J Neural Transm. 123:365–370.

33. Cardoso VF, Martins P, Botelho G, Rebouta L, Lanceros-Méndez S, Minas G (2010) Degradation studies of transparent conductive electrodes on electroactive poly(vinylidene fluoride) for uric acid measurements. Sc Technol Adv Mat. 11:045006.

34. Song Z-H, Hou S (2002) Chemiluminescence assay for uric acid in human serum and urine using flow-injection with immobilized reagents technology. Anal Bioanal Chem. 372:327–332.

35. Cai W, Lai J, Lai T, Xie H, Ye J (2016) Controlled functionalization of flexible graphene fibers for the simultaneous determination of ascorbic acid, dopamine and uric acid. Sensor Actuat B Chem. 224:225–232.

36. Li X-L, Shi Q, Jin W, Li G, Todoroki K, Mizuno H, Toyo'oka T, Min JZ (2016) Uric acid quantification in fingernail of gout patients and healthy volunteers using HPLC-UV: Quantitative assessment of uric acid in fingernail of gout patients. Biomed Chromatogr. 30:1338-1342.

37. Dai X, Fang X, Zhang C, Xu R, Xu B (2007) Determination of serum uric acid using high-performance liquid chromatography (HPLC)/isotope dilution mass spectrometry (ID-MS) as a candidate reference method. J Chromatogr B. 857:287–295.

38. Jin D, Seo M-H, Huy BT, Pham Q-T, Conte ML, Thangadurai D, Lee Y-I (2016) Quantitative determination of uric acid using CdTe nanoparticles as fluorescence probes. Biosens Bioelectron. 77:359–365.

39. Kumar A, Hens A, Arun RK, Chatterjee M, Mahato K, Layek K, Chanda N (2015) A paper based microfluidic device for easy detection of uric acid using positively charged gold nanoparticles. Analyst. 140:1817–1821.

Chapter 4 A central composite design optimized PAD for the determination of isoniazid

This chapter is based on

"Fabrication of paper-based analytical devices optimized by central composite design",

Vahid Hamedpour; Riccardo Leardi; Koji Suzuki; Daniel Citterio,

Analyst, **2018**, 143, 2102-2108.

Summary

In this work, an application of a design of experiments approach for the optimization of an isoniazid assay on a single-area inkjet-printed paper-based analytical device (PAD) is described. For this purpose, a central composite design was used for evaluation of the effect of device geometry and amount of assay reagents on the efficiency of the proposed device. The variables of interest were printed length, width, and sampling volume as factors related to device geometry, and amounts of the assay reagents polyvinyl alcohol (PVA), NH_4OH, and $AgNO_3$. Deposition of the assay reagents was performed by a thermal inkjet printer. The colorimetric assay mechanism of this device is based on the chemical interaction of isoniazid, ammonium hyroxide, and PVA with silver ions to induce the formation of yellow silver nanoparticles (AgNPs). The in-situ-formed AgNPs can be easily detected by the naked eye or with a simple flat-bed scanner. Under optimal conditions, the calibration curve was linear in the isoniazid concentration range 0.03–10 mmol L^{-1} with a relative standard deviation of 3.4% (n = 5 for determination of 1.0 mmol L^{-1}). Finally, the application of the proposed device for isoniazid determination in pharmaceutical preparations produced satisfactory results.

4.1. Introduction

Paper-based analytical devices (PADs) can become inexpensive portable sensing platforms for various applications like food safety control, environmental monitoring, disease diagnostics, and water testing [1–5]. These devices, owing to features such as simple fabrication, low sample consumption, easy usage, and low cost, are mostly utilized for clinical, biological, or chemical analyses in developing countries or remote locations as well as in emergency situations [6, 7]. Making use of modern technologies, such as wax printing technology for substrate patterning and inkjet technology for printing the assay reagents in small amounts, as well as the combination of PADs with highly sensitive detection methods, can improve the sensitivity of the devices [8, 9]. However, investigation into the parameters that may affect the device performance, such as shape and size of device and assay reagent amounts, is still one of the challenges that needs to be overcome.

One of the aims of design of experiments (DoE) is to select the optimum experimental conditions with limited experimental effort [10]. This approach is therefore superior to traditional one-factor-at-time (OFAT) optimization strategies. Furthermore, DoE also allows to detect and to study interactions among experimental variables, which is not possible by changing just one variable at a time.

In the current study, a DoE approach is demonstrated on a model PAD targeting the detection of isoniazid, which is one of the common first-line therapies for drug-susceptible tuberculosis (Fig. 4-1a). Tuberculosis is a fatal disease caused by Mycobacterium tuberculosis and mainly affects the lungs and easily spread through tiny droplets released into the air via sneezes and coughs (Fig. 4-1b) [11, 12]. According to these, the dosage control of the active compounds in the pharmaceutical preparations is a necessary task because drugs must be marketed as safe and therapeutically active principals whose performance should be predictable and consistent

[13]. The importance and widespread use of this drug has encouraged researchers to devise novel analytical methods for the rapid and sensitive determination of isoniazid.

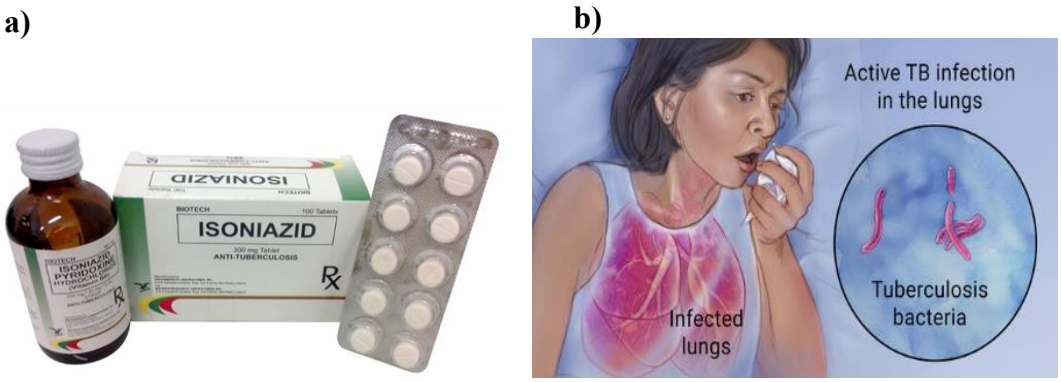

Figure 4-1. a) Isoniazid in tablet and syrup forms, and b) the effect of Mycobacterium tuberculosis on lunges.

During recent decades, several analytical methods have been reported for the determination of isoniazid and some attempts to integrate proposed methods with sensors have gained attention [13]. To the best of our knowledge, this is the first report on the application of PADs for isoniazid determination and the proposed device can be used as a portable platform for online dosage control for process quality control by pharmaceutical companies.

The detection method of this device is based on the plasmon resonance of in-situ-formed silver nanoparticles (AgNPs) [14]. Since the color intensity observed in the detection zone is highly dependent on several features of device design, attention should be given to them. For this purpose, an experimental design, and more specifically a central composite design (CCD), was employed for evaluating the impact of device geometry and amounts of assay reagents on the proposed device's sensitivity. CCD is a second order model (rotatable and orthogonal) experimental design which provides information on linear, interaction, and quadratic terms and is widely used for formulation or process optimization by pharmaceutical companies [15]. The matrix of a CCD consists of an embedded full factorial or fractional factorial design, a star

design, and n replicates of the central point [16]. Star points have a distance α from the centre point, and their values determine the type of design, make it flexible, and allow estimation of curvature [17]. Since the star points (α) represent new extreme values (low and high) for each factor in the design, all factors will be studied in five levels (−α, −1, 0, +1, +α).

Although the DoE approach may contribute to PADs becoming powerful devices, only a few studies have used this optimization method. Moreover, in these studies, simplified optimization procedures lacking the investigation of all effective factors such as size and shape of inlet area and the amount of required assay reagents, have been applied [18, 19].

We have previously reported the application of a Box-Behnken Design (BBD) on a PAD, where, because of chemistry-related experimental constraints, carrying out the experiments including all factors simultaneously at their highest or lowest levels had to be avoided [20]. Thus, the investigation of all mentioned conditions, corner points, and star points was not possible. According to the practical applications and compared to BBD, CCD is more efficient and able to estimate new data points more reliably [17, 21]. In the present work, due to the features of isoniazid, the experimental restrictions mentioned above are no longer encountered. Therefore, a CCD with the ability to study extreme conditions and better prediction quality was applied. Finally, studies on the determination of isoniazid in tablet and injectable formulations were carried out to illustrate the feasibility of the proposed device.

4.2. Experimental section

4.2.1. Reagents and materials

All chemicals were used as obtained without further purification. A stock standard solution of isoniazid (0.1 mol L^{-1}) was prepared by dissolving the appropriate amount of isoniazid (Sigma Aldrich, Germany) in ultra-pure water. A stock solution of polyvinyl alcohol (PVA, 2.8 g L^{-1}) was prepared by dissolving 0.14 g of PVA (Kanto, Tokyo, Japan) in ultra-pure water and diluting to 50 mL. A solution containing 0.5 mol L^{-1} NH_4OH (Wako) was used. A stock solution of $AgNO_3$ (0.01 mol L^{-1}) was prepared by dissolving the proper amount of $AgNO_3$ (Wako) in ultra-pure water.

4.2.2. Instrumentation

Ultra-pure water was prepared by a PURELAB flex set (Veolia, Paris, France). A ColorQube 8570 wax printer (Xerox, Norwalk, CT, USA) was used for printing the wax barrier. A thermal Canon ip2700 inkjet printer (Canon, Tokyo, Japan) was used for the deposition of the assay reagents (PVA, NH_4OH, and $AgNO_3$). For this purpose, the standard Canon printer's black cartridge was cut open and the inside sponge removed, and then the cartridge was washed completely with ultra-pure water and dried. Finally, each cartridge was fed with about 2 mL of different assay solutions, separately. Colour intensity was analyzed by ImageJ version 1.50f.

4.2.3. Device fabrication

First, filter paper (Whatman grade 1, GE Healthcare, Buckinghamshire, U.K.) was cut and adjusted to A4 size; then, the designated pattern was printed by a wax printer. The pattern was designed with Microsoft PowerPoint and printed only on the top side of the filter paper. For complete diffusion of the wax into the thickness of the paper, the paper was heated on a hot plate (NHS-450ND, NISSIN Co., Tokyo, Japan) for 90 s.

Afterward, the back of the paper was pouched at 150°C with an adhesive lamination film (thickness = 150 µm) using a hot laminator (QHE325, Meikoshokai Co., Ltd., Tokyo, Japan). Finally, 11 printing cycles of PVA 2.8 g L^{-1}, 8 printing cycles of NH_4OH 0.5 mol L^{-1} and 12 printing cycles of $AgNO_3$ 0.01 mol L^{-1} were deposited consecutively on the same area (Fig. 4-2).

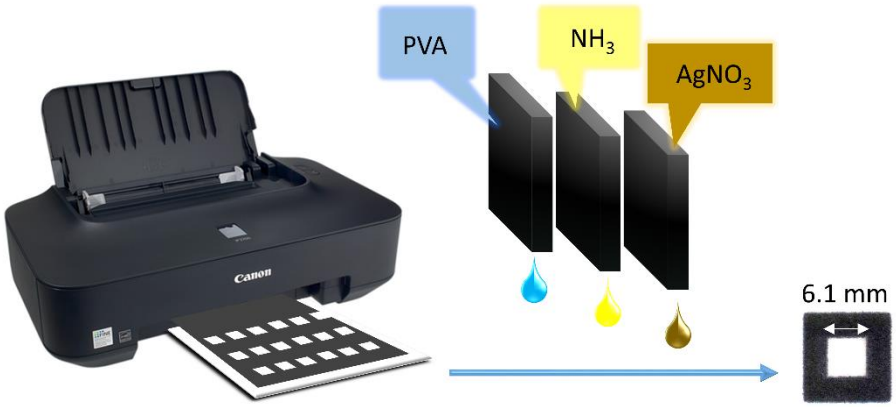

Figure 4-2. Schematic of PAD fabrication for the determination of isoniazid.

4.2.4. Real sample preparation

For the evaluation of the proposed method's accuracy, the concentration of isoniazid in both tablets (100 and 300 mg) and injection (100 mg mL^{-1}) were determined using the fabricated PAD and compared with results obtained using the standard method [22]. The samples were assayed by the international pharmacopeia method, which describes the titration of the

isoniazid sample with potassium bromate in the presence of potassium bromide using methyl red as an indicator. For this purpose, five tablets were weighed accurately, and the average weight of each tablet was found. Then, the tablets were finely powdered and carefully mixed. A portion of the mixture containing about 13.78 mg of isoniazid, was weighed accurately and put in a glass vessel; about 70 mL of ultra-pure water was added and stirred for 15 min. Then, after filtering, the solution was transferred to a 100-mL volumetric flask using ultra-pure water for dilution up to the mark, resulting in a nominal 1.0 mmol L^{-1} solution. In the case of the injection type, solutions of five samples were mixed. Then, the appropriate volume to result in a nominal 1.0 mmol L^{-1} solution of isoniazid was transferred to a 20 mL volumetric flask and diluted to the mark by ultra-pure water. It should be mentioned that in all cases 9.2 µL of the samples were deposited on the paper device (Fig. 4-3).

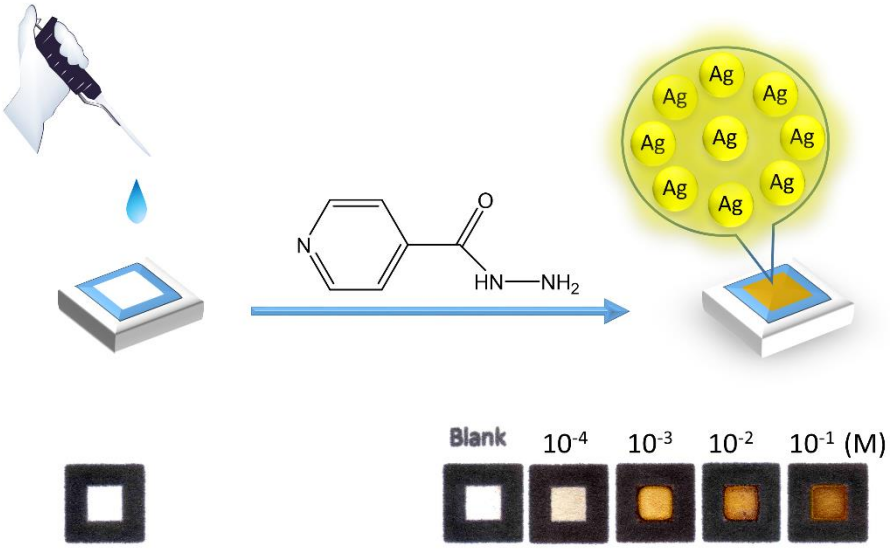

Figure 4-3. Schematic procedure for the determination of isoniazid using the PADs and representative color scans of devices after exposure to different concentrations of isoniazid.

4.3. Results and discussion

4.3.1. In-situ formation of silver nanoparticles

According to previous studies [14, 23], $[Ag(NH_3)_2]^+$ complex ions can be reduced to silver nanoparticles at relatively high concentrations of a reducing agent such as isoniazid. The proposed method is fundamentally similar to the Tollens process, which was already reported for the synthesis of AgNPs [23]. In this process, by having $[Ag(NH_3)_2]^+$ as an oxidant and isoniazid as a reductant, AgNPs giving rise to a yellowish color can be obtained [24, 25] (Fig. 4-4).

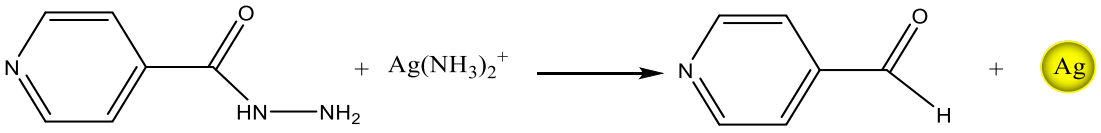

Figure 4-4. The overall reaction between isoniazid and silver ions leading to formation of AgNPs.

Compared to a uric acid study [20], basic conditions are not required because isoniazid possesses higher reducing strength. It is worth mentioning that in this method, PVA acts as a capping agent and effectively stabilizes formed AgNPs [26, 27]. Due to the formation of AgNPs, a change from colorless to yellow occurs. The in-situ formation of AgNPs was verified by scanning electron microscopy (SEM) [28] as can be confirmed by comparing the SEM images recorded of the paper surface before and after application of an isoniazid sample (Fig. 4-5). The observed changes can be ascribed to a redox reaction between isoniazid and $[Ag(NH_3)_2]^+$.

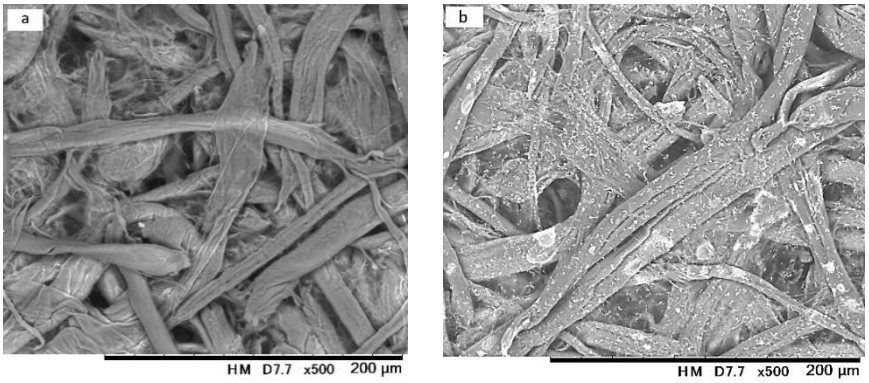

Figure 4-5. Representative SEM images (500×magnification) of a) the PAD after exposure to ultra-pure water b) the PAD after exposure to isoniazid.

4.3.2. Structure of the experimental design

The factors influencing the device efficiency, including area length, area width, sampling amount, and amount of inkjet-deposited assay reagents like PVA, NH_4OH, and $AgNO_3$, were evaluated by performing an adequate DoE. In CCD, the total number of required experiments is determined by the following equation [29]:

$$N = 2^f + 2f + n_0 \qquad \text{Eq. 4-1}$$

where, f and n_0 represent the number of factors and centre points (f= 6, n_0 =2), respectively. In this equation, the factorial part, star points and centre points are demonstrated respectively. In this work, instead of the full factorial (2^f), a fractional factorial (2^{f-1}) design has been utilized in order to reduce the number of experiments [30]. Accordingly, For this purpose, a CCD (2^{6-1} + 12 star points + 2 centre points) with 46 experiments, which enabled the estimation of the linear effects, the interactions between pairs of variables and the quadratic terms, was applied. Fig. 4-6 demonstrates some of the fabricated devices according to experimental matrix.

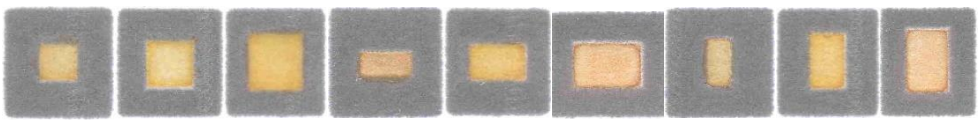

Figure 4-6. Some of fabricated devices according to experimental matrix.

The value of α was set to 2.4 for variables A, B and C and to 2.33 for variables D, E and F. The factors and their ranges were selected according to preliminary experiments. Fig. 4-7a demonstrates some of fabricated devices with different shapes and sizes. It can be seen that at the similar condition the response of single box is better than the others. Therefore, single box design was selected for the determination of isoniazid. Fig. 4-7b depicts the necessity of presence of PVA. The reason is that in this sensing mechanism, the formed AgNPs are in a high free energy state and because of Van der Waals forces tend to aggregate and lower their energies. This phenomenon can be avoided by rising the repulsive contribution to the potential energy. Therefore, attaching a capping layer such as PVA to the free coordination sites of the nanoparticles can block their vacant coordination sits and support the stabilization process (steric stabilization).

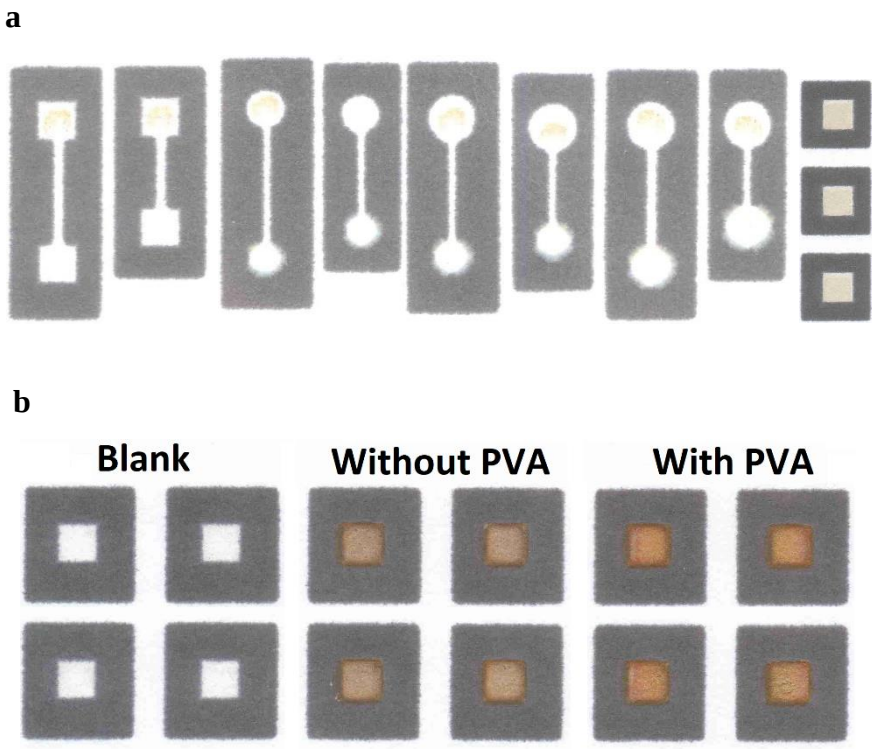

Figure 4-7. a) Preliminary tests for selection of device shape (in all cases 3, and 5 cycles of PVA, $AgNO_3$ and NH_3 were printed, respectively), and b) preliminary tests for evaluation of the necessaty of assay reagents. Colorimetric response observed on paper upon exposure to water (blank) or 0.1 M isoniazid solution in absence and presence of PVA.

The examined factors and their levels, both coded values and actual values, are shown in Table 4-1. In all experiments, the calculated response (ΔB) is the blue color intensity of the sample, which is corrected for the corresponding blank.

Table 4-1. Variables and their investigated levels in CCD.

Variable	symbols	Levels				
		-α	-1	0	+1	+α
Area length (mm)	A	4.6	6.0	7.0	8.0	9.4
Area width (mm)	B	4.6	6.0	7.0	8.0	9.4
Sampling volume (μL)	C	1.2	4.0	6.0	8.0	10.8
PVA	D	2.0	6.0	9.0	12.0	16.0
NH_3	E	2.0	6.0	9.0	12.0	16.0
$AgNO_3$	F	2.0	6.0	9.0	12.0	16.0

4.3.3. Study of independent factors impact on the color intensity

As mentioned before, with a DoE it is possible to estimate the coefficients of a quadratic model with interactions [31]. The relationship between the color intensity (CI) and the factors (as coded values) is explained by the model reported in Eq. 4-2, in which the variables are coded according to Table 4-1. The Pareto chart is also shown in Fig. 4-8.

$$CI = 112.7 - 3.5\,A - 1.4\,B + 10.6\,C + 4.5\,D + 6.6\,E + 20.2\,F + 9.7\,AB + 2.2\,AC - 1.9\,AD + 0.5\,AE - 2.7\,AF - 0.8\,BC - 1.0\,BD + 2.9\,BE - 0.2\,BF + 3.6\,CD - 4.2\,CE + 6.3\,CF + 2.4\,DE + 3.8\,DF - 2.6\,EF - 0.9\,A^2 - 2.4\,B^2 + 3.8\,C^2 - 2.8\,D^2 - 4.6\,E^2 - 6.3\,F^2 \quad \text{Eq. 4-2}$$

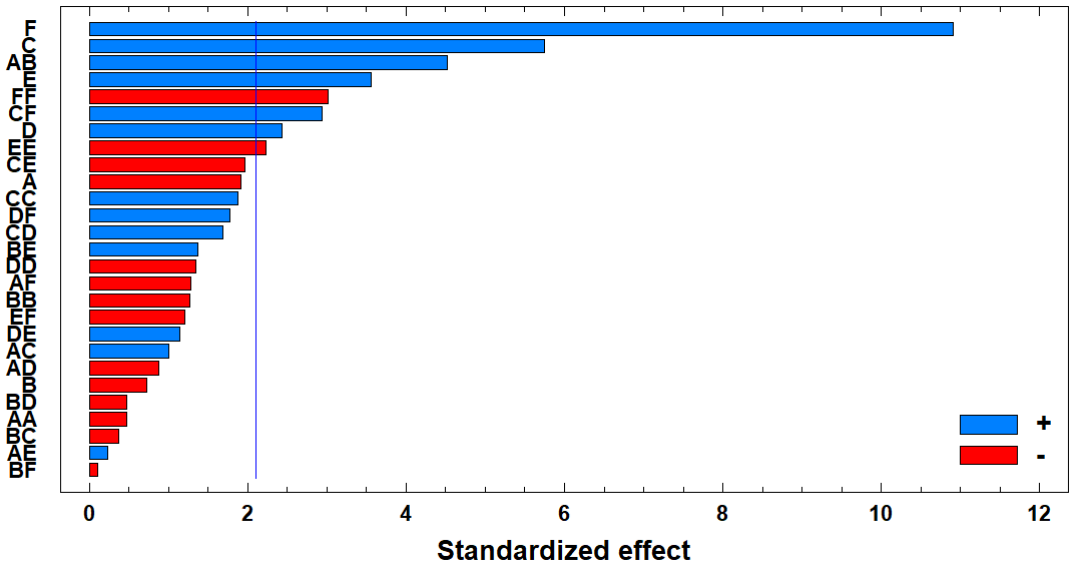

Figure 4-8. Pareto chart of the main effects obtained from optimizing the experimental condition of isoniazid detection devices. For meaning of the coded parameters, please refer to Table 4-1.

A is area length, B is area width, C is sampling volume, D, E and F are the amounts of deposited assay reagents consisting of PVA, NH_4OH and $AgNO_3$, respectively. It should be noted that these amounts are expressed as number of printing cycles used for the inkjet-based deposition onto the PADs. The adjusted R^2 is 0.83 and the standard deviation of the residuals is 12.2.

The significant coefficients are the linear terms for C, D, E and F, plus the interactions AB and CF and the quadratic terms for E and F. This means that all variables have a significant effect on the response. Two factors—sampling volume (coded as C) and printing cycles of $AgNO_3$ (F)—are by far the most relevant, with the largest linear effects and a significant interaction (CF). Factor F also shows a large quadratic effect (FF). Other factors, which are related to assay reagents, such as printing cycles of NH_4OH (E) and PVA (D) have a significant linear effect, and factor E also has a significant quadratic effect (EE). Device geometry factors, including box length (A) and box width (B), do not have a significant linear effect; however, their interaction is highly significant (AB).

Except for D, having only a linear significant effect (positive, meaning that the higher, the better), all the other variables are involved in significantly higher terms (interactions or quadratic terms). Therefore, to obtain a better understanding of the phenomenon, response surfaces must be drawn. In each plot, the effect of two factors can be studied while the remaining four factors were set at the centre levels.

The impact of area length and area width (AB) on the obtained color intensity is shown in Fig. 4-9a. In this figure, the circle defines the experimental domain. From this plot, the strong interaction between the two variables can be easily interpreted. The fact that the best response is obtained on the diagonal of the plot means that the ratio of the variables is crucial. It means that by increasing the value of A, the value of B must also be increased. Since the values of the responses on that direction are very similar, it can be concluded that the relevant parameter is the shape, and not the size of the area. In the case of unequal area length and width, the observed "coffee ring" phenomenon, a pattern caused by solute left on a substrate after evaporation of the solvent droplet, was more pronounced than in the case of equal length and width, corresponding to a square reaction area. Hence, a smaller device with a square shape, which also requires lower consumption of the assay reagents, is preferred.

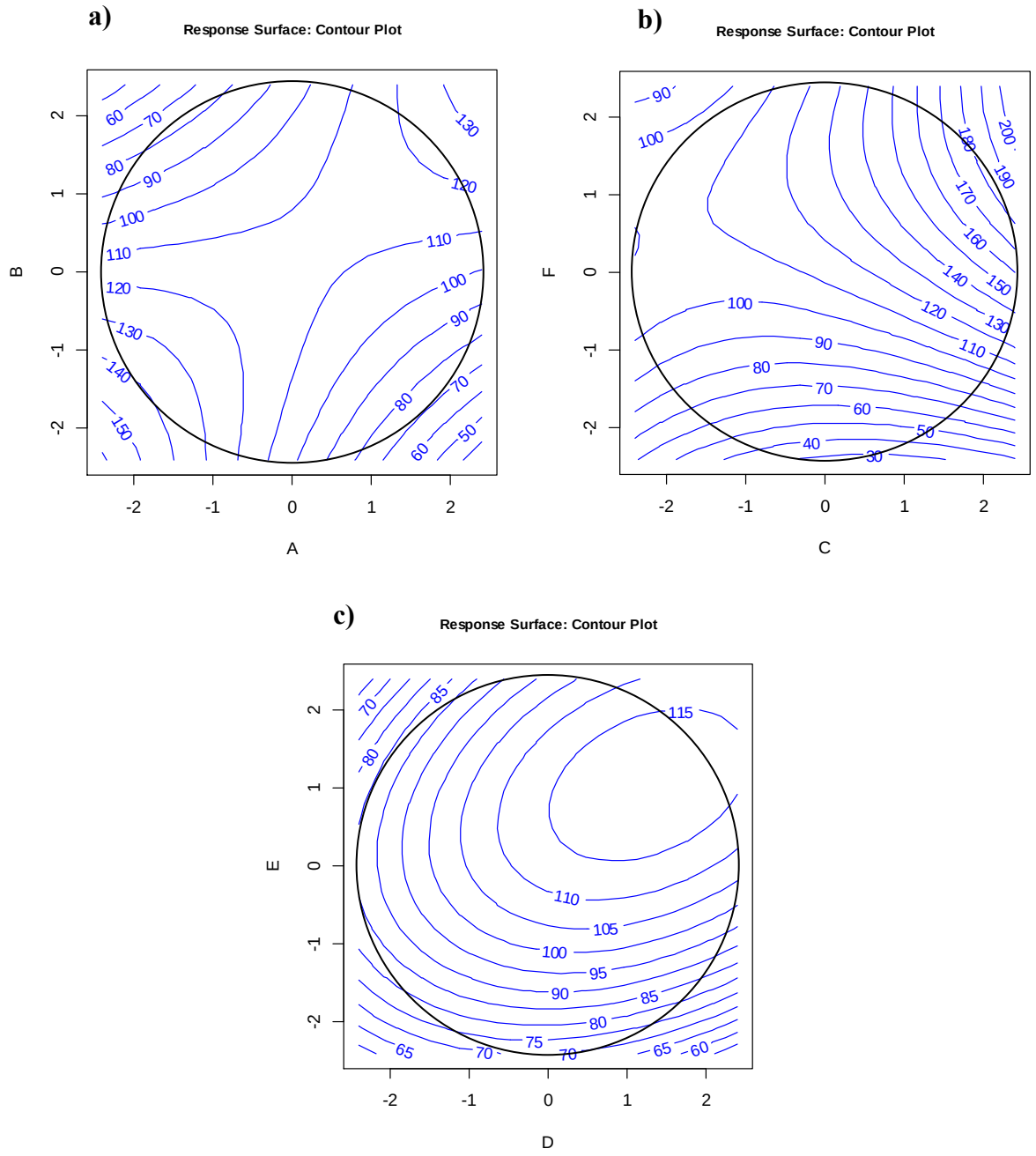

Figure 4-9. Response surface on the planes of a) A – B (area length vs. area width), b) C – F (sampling volume vs. printing cycles of $AgNO_3$); and c) D – E (printing cycles of PVA vs. printing cycles of NH_4OH).

The response surface on the plane C – F (Fig. 4-9b) shows that an increase of the sampling volume only produces an effect while the number of printing cycles of $AgNO_3$ is high. From a chemical viewpoint, by increasing the amount of $AgNO_3$ and sample volume, the amount of available silver ions that can participate in the redox reaction and available isoniazid to act as reducing agents will be increased. Therefore, the obtained color intensity will be higher.

A similar explanation can be given for the amounts of ammonia (E) and PVA (D). From the plot, it can be seen that low values of both variables should be avoided (Fig. 4-9c).

When trying to keep A and B as small as possible, the conditions inside the experimental domain corresponding to the highest predicted response (184) are the following: area length 6.1 mm (coded value −0.9), area width 6.1 mm (−0.9), sampling volume 9.2 μL (1.6), PVA 11 printing cycles (0.67), NH_4OH 8 printing cycles (−0.33), and $AgNO_3$ 12 printing cycles (1). Performing replicated experiments (n=8) at these conditions produced an average response of 179 ± 1.5 in good agreement with the predicted value.

It has to be noticed that this result is significantly higher than the best result obtained by the actually performed experiments within the design matrix (165; see Appendix Chapter 4 Table 4-1). This clearly shows that the possibility of building a predictive model allows the detection of the real optimum inside the experimental domain. Owing to the presence of several significant interactions and quadratic terms, the OFAT approach would not have been able to find an acceptable solution.

4.3.4. Study of interferences

For this purpose, the determination of 1.0 mmol L^{-1} isoniazid in the presence of potentially interfering substances was examined. The tolerance limits of various ions and organic substances were selected as the concentrations of the interfering species that cause less than ±5% relative error. The tolerance limits for analyte ratios were over 500 for NO^{3-}, Na^{+}, K^{+}, fructose, glucose, and sucrose; 100 for SO_4^{2-} and urea; 75 for Mg^{2+}, Ca^{2+}; 50 for NH^{4+}; 35 for Cl^{-}; 10 for PO_4^{3-}; 5 for citric acid and 1 for ascorbic acid.

4.3.5. Analytical figures of merit

The relation between the color intensity and isoniazid concentration, under the optimal conditions, was determined by using different standard solutions. Under the optimum conditions, the linearity of the calibration graph ranged between 0.03 and 1 mmol L^{-1} with a correlation coefficient of 0.991 (Fig. 4-10), which shows a good linear regression between the colour intensity and the concentrations. The calibration equation was Y=72.6 C + 347.4, where Y is the colour intensity, and C is the isoniazid concentration. The relative standard deviation (n=5 for the determination of 1.0 mmol L^{-1}) was estimated to be 3.4%.

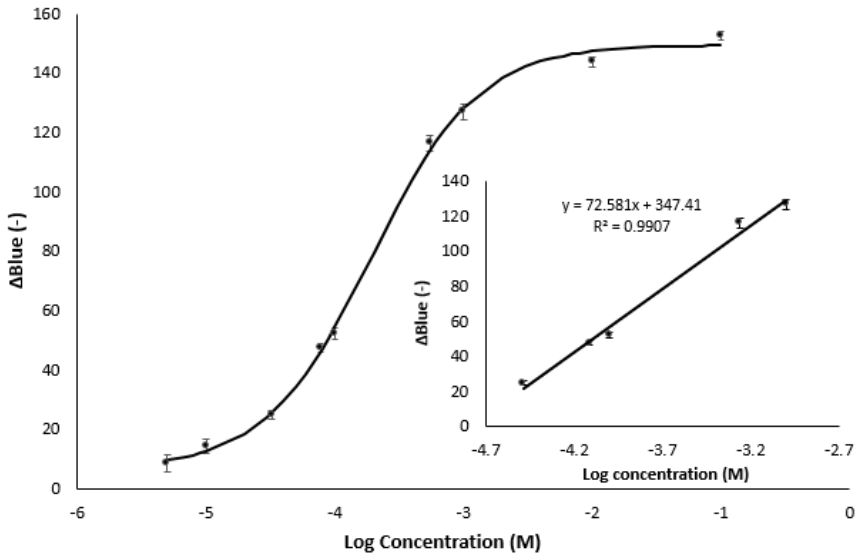

Figure 4-10. Calibration curve for isoniazid (n=5).

4.3.6. Application to real samples

The optimized method was employed for the quantification of isoniazid in real samples. For evaluating the accuracy of the proposed method, the obtained results were compared with the reference method (Table 4-2). The obtained results show the capability of the device in determination of isoniazid in pharmaceutical samples.

Table 4-2. Determination of isoniazid in real samples by PAD

Sample	Sample taken (mmol L^{-1})	Found (mmol L^{-1})	Reference method [22] (mmol L^{-1})
Tablet (300 mg)	1.0	0.99 ± 0.06	1.01 ± 0.03
Tablet (100 mg)	1.0	0.98 ± 0.08	1.00 ± 0.03
Injection (100 mg ml^{-1})	1.0	1.02 ± 0.15	0.99 ± 0.05

4.4. Conclusions

In most reports on the development of PADs, the focus is on the implementation of a particular sensing mechanism on a paper substrate, while the optimization of device geometry and amounts of deposited reagents remains a challenge. In other words, although the mentioned factors are often optimized, this is mostly done using the traditional OFAT approach, which cannot provide any information about interactions and quadratic effects. Therefore, it often happens that an "optimal condition" far from the ideal one is selected. In the current work, after performing only 46 experiments, the colorimetric response obtained at the optimum conditions detected by the model was significantly higher than any of the responses experimentally obtained and not significantly different from the predicted value. According to these results, it can be concluded that the application of design of experiments on PADs can lead to low cost but sensitive devices, which are the main goal of fabrication of PADs.

The proposed device primarily served as a simple model to demonstrate the possibilities of the design of experiments approach. Nevertheless, due to its simplicity, it provides a rapid and user-friendly method for on-site isoniazid quantification in pharmaceutical preparations.

References

1. Martinez AW, Phillips ST, Butte MJ, Whitesides GM (2007) Patterned Paper as a Platform for Inexpensive, Low-Volume, Portable Bioassays. Angew Chem Int Ed. 46:1318–1320.

2. Kraly JR, Holcomb RE, Guan Q, Henry CS (2009) Review: Microfluidic applications in metabolomics and metabolic profiling. Anal Chim Acta. 653:23–35.

3. Nery EW, Kubota LT (2013) Sensing approaches on paper-based devices: a review. Anal Bioanal Chem. 405:7573–7595.

4. Sharma N, Barstis T, Giri B (2018) Advances in paper-analytical methods for pharmaceutical analysis. Eur J Pharm Sci. 111:46–56.

5. Sher M, Zhuang R, Demirci U, Asghar W (2017) Paper-based analytical devices for clinical diagnosis: recent advances in the fabrication techniques and sensing mechanisms. Expert Rev Mol Diagn. 17:351–366.

6. de Oliveira RAG, Camargo F, Pesquero NC, Faria RC (2017) A simple method to produce 2D and 3D microfluidic paper-based analytical devices for clinical analysis. Anal Chim Acta. 957:40–46.

7. Morbioli GG, Mazzu-Nascimento T, Stockton AM, Carrilho E (2017) Technical aspects and challenges of colorimetric detection with microfluidic paper-based analytical devices (μPADs) - A review. Anal Chim Acta. 970:1–22.

8. Yamada K, Henares TG, Suzuki K, Citterio D (2015) Paper-Based Inkjet-Printed Microfluidic Analytical Devices. Angew Chem Int Ed. 54:5294–5310.

9. Yamada K, Shibata H, Suzuki K, Citterio D (2017) Toward practical application of paper-based microfluidics for medical diagnostics: state-of-the-art and challenges. Lab Chip 17:1206–1249.

10. Leardi R (2009) Experimental design in chemistry: A tutorial. Anal Chim Acta. 652:161–172.

11. Haghighi B, Bozorgzadeh S (2010) Flow injection chemiluminescence determination of isoniazid using luminol and silver nanoparticles. Microchem J. 95:192–197.

12. Chen C, Ortega F, Alameda L, Ferrer S, Simonsson USH (2016) Population pharmacokinetics, optimised design and sample size determination for rifampicin, isoniazid, ethambutol and pyrazinamide in the mouse. Eur J Pharm Sci. 93:319–333.

13. Lima KCMS, Santos ACF, Fernandes RN, Damos FS, de Cássia Silva Luz R (2016) Development of a novel sensor for isoniazid based on 2,3-dichloro-5,6-dicyano-p-benzoquinone and graphene: Application in drug samples utilized in the treatment of tuberculosis. Microch J. 128:226–234.

14. Amirjani A, Bagheri M, Heydari M, Hesaraki S (2016) Label-free surface plasmon resonance detection of hydrogen peroxide; a bio-inspired approach. Sens Actuat B Chem. 227:373–382.

15. Singh G, Pai R, Devi K (2012) Response surface methodology and process optimization of sustained release pellets using Taguchi orthogonal array design and central composite design. J Adv Pharm Technol Res. 3:30–40.

16. Bezerra MA, Santelli RE, Oliveira EP, Villar LS, Escaleira LA (2008) Response surface methodology (RSM) as a tool for optimization in analytical chemistry. Talanta 76:965–977.

17. Zolgharnein J, Shahmoradi A, Ghasemi JB (2013) Comparative study of Box-Behnken, central composite, and Doehlert matrix for multivariate optimization of Pb (II) adsorption onto *Robinia* tree leaves: Multivariate optimization. J Chemometr. 27:12–20.

18. Shariati-Rad M, Irandoust M, Mohammadi S (2016) Multivariate analysis of digital images of a paper sensor by partial least squares for determination of nitrite. Chemomtr Intell Lab. 158:48–53.

19. Avoundjian A, Jalali-Heravi M, Gomez FA (2017) Use of chemometrics to optimize a glucose assay on a paper microfluidic platform. Anal Bioanal Chem. 409:2697–2703.

20. Hamedpour V, Postma GJ, van den Heuvel E, Jansen JJ, Suzuki K, Citterio D (2018) Chemometrics-assisted microfluidic paper-based analytical device for the determination of uric acid by silver nanoparticle plasmon resonance. Anal Bioanal Chem. 410:2305-2313.

21. Rakić T, Kasagić-Vujanović I, Jovanović M, Jančić-Stojanović B, Ivanović D (2014) Comparison of Full Factorial Design, Central Composite Design, and Box-Behnken Design in Chromatographic Method Development for the Determination of Fluconazole and Its Impurities. Anal Lett. 47:1334–1347.

22. The International Pharmacopoeia (Ph. Int.), Seventh Edition, 2017, Isoniazid tablets. In: World Health Organization. http://apps.who.int/phint/pdf/b/6.1.194.Isoniazid-(Isoniazidum).pdf or http://apps.who.int/phint/pdf/b/6.2.2.65.Isoniazid-tablets-(Isoniazidi-compressi).pdf, Accessed March 22, 2018.

23. Amjadi M, Rahimpour E (2012) Silver nanoparticles plasmon resonance-based method for the determination of uric acid in human plasma and urine samples. Microchim Acta. 178:373–379.

24. Wu LP, Li YF, Huang CZ, Zhang Q (2006) Visual Detection of Sudan Dyes Based on the Plasmon Resonance Light Scattering Signals of Silver Nanoparticles. Anal Chem. 78:5570–5577.

25. He J, Kunitake T, Nakao A (2003) Facile In Situ Synthesis of Noble Metal Nanoparticles in Porous Cellulose Fibers. Chem Mater. 15:4401–4406.

26. Sharma VK, Yngard RA, Lin Y (2009) Silver nanoparticles: Green synthesis and their antimicrobial activities. Adv Colloid Interface Sci. 145:83–96.

27. Yin Y, Li Z-Y, Zhong Z, Gates B, Xia Y, Venkateswaran S (2002) Synthesis and characterization of stable aqueous dispersions of silver nanoparticles through the Tollens

process Electronic supplementary information (ESI) available: photographs of silver mirror, and of stable dispersions of silver nanoparticles from mixing diluted silvering solutions under sonication at various times. J Mater Chem. 12:522–527.

28. Pourreza N, Golmohammadi H, Naghdi T, Yousefi H (2015) Green in-situ synthesized silver nanoparticles embedded in bacterial cellulose nanopaper as a bionanocomposite plasmonic sensor. Biosens Bioelectron. 74:353–359.

29. Arslan FN, Azak H (2018) Application of Central Composite Design for the Optimization of Reverse-Phase HPLC/DAD Separation of the cis- and trans- Isomers of Long-Chain Unsaturated Fatty Acids. Food Anal Method. 11:1163–1179.

30. Sanchez SM, Sanchez PJ (2005) Very large fractional factorial and central composite designs. ACM T Model Comput S. 15:362–377.

31. Baş D, Boyacı İH (2007) Modeling and optimization I: Usability of response surface methodology. J Food Eng. 78:836–845.

Chapter 5 General conclusion

5.1. Summary of the results

The ideology of fabrication of paper-based analytical devices (PADs) originates from human being dream which is the production of low-cost, robust, and user-friendly devices for untrained people. Therefore, PADs can be an alternative to the frequently used techniques which are requiring experts and higher prices. In this regard, various studies on applicable sensing mechanisms, patterning techniques, assay reagent deposition methods, and signal readout approaches have been performed, but researchers rarely paid attention to potential of chemometrics in device fabrication and data presentation. Therefore, in spite of their high potential for practical application, PADs have not been commercialized. Chemometrics as a chemical discipline has the ability to overcome the remaining weak points such as device optimization, data analysis, and image processing. In other words, chemometrics is able to embolden the PADs and facilitate their commercialization process.

In chapter 2 a comparative study of three common experimental designs in optimization of paper-based analytical devices was introduced. These designs were employed to optimize a single device and advantages and disadvantages of each design have been practically investigated. The developed detection technique was based on the protonation and deprotonation of methyl orange, which leads to a color change in the absence and presence of isoniazid. In this work, in order to minimize the errors caused by manual detection zone selection and to accelerate the color values analysis, a MATLAB-based algorithm was developed and employed.

Chapter 3 describes a chemometrics-assisted colorimetric uric acid assay on inkjet-printed microfluidic paper-based analytical devices (μPADs). For this purpose, design of experiments, data analysis, and image processing were employed in development of μPAD. In the optimization step, due to experimental constraints, a Box–Behnken design was utilized. Then, the device was exposed to four urine samples with four different uric acid concentration, and the outliers were successfully detected in real time by a partial least squares discriminant analysis (PLS-DA) of scanned images.

Chapter 4 describes fabrication of a paper-based isoniazid assaying analytical device optimized by central composite design. The design of experiment approach contributed to reduce the total amount of required experiments and therefore, to time and cost savings. For this purpose, a seven-factor experimental design consisting of a total of 46 experiments was used for investigation of the impact of all probable factors on the device efficiency, simultaneously. Finally, the comparison of results of proposed device and standard method verified the analytical accuracy of the proposed technique.

To summarize, this research thesis aimed to address the potential of chemometrics in fabrication of reliable and sensitive PADs for point-of-care diagnosis. The main focus of this research is on the development of PADs assisted by design of experiments, along with an investigation on image processing and data analysis. The practical applications of these techniques were exhibited in uric acid and isoniazid devices.

5.2. Future outlook

Fig. 5-1 demonstrates the pathway toward the commercialization of the paper-based analytical devices. Up to date, most of the required parts have been studied, but the two less paid attention steps, which are experimental design and data analysis, are still the remained obstacles for bulk production. The design of experiment approach by the ability to save time and cost, and increase the efficiency, is a step toward real-world application. Among the investigated statistical models, D-optimal design by having higher capability and requiring smaller number of the experiments can be an appropriate alternative for other designs. The other barrier is data analysis which is not only suitable for better data presentation in academic researches but also can be useful in negotiation with industrial partners. The obtained results of this approach can be utilized in validation step and facilitate the marketing process. In conclusion, by overcoming these challenges, and fabricating long term stable and reusable devices investing in PADs will be a priority for companies.

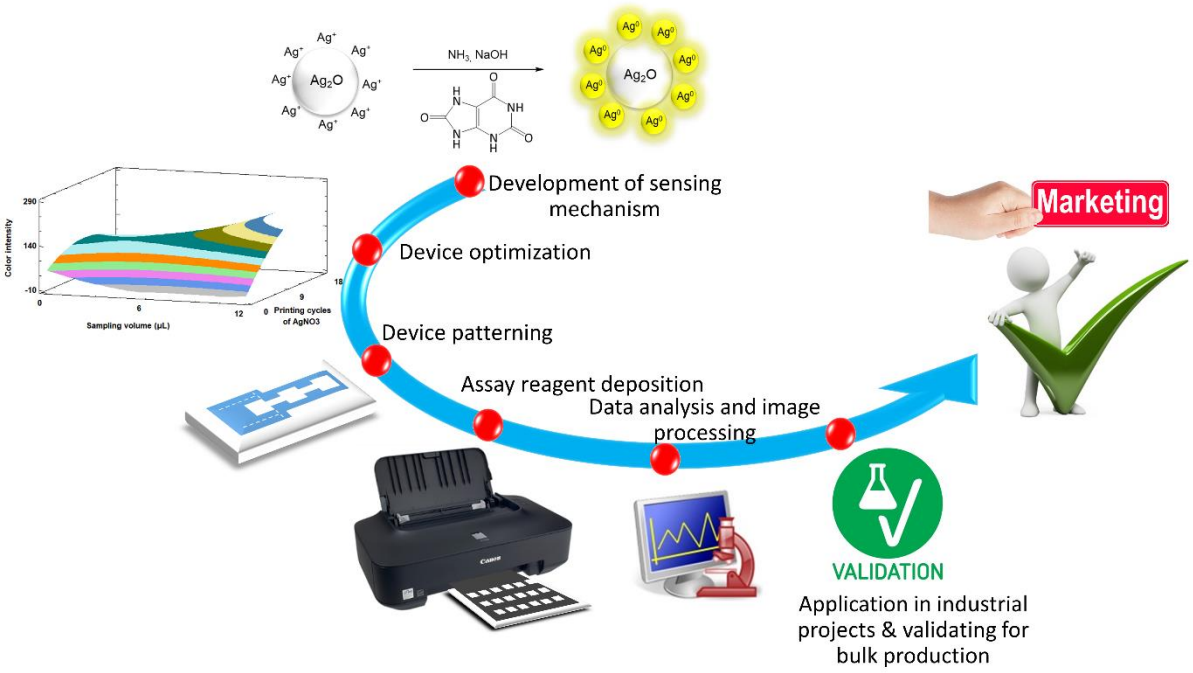

Figure 5-1. Required steps for commercialization of PADs.

Appendix

Chapter 2

Developed script for rectangle detection of isoniazid device:

```
detection of function [meandiff,crops]=sqdetect(imagefile,n)

% [md,crops] = sqdetect('imagefile.jpg',n);
%
% n = number of rectangles to be detected (samples + blanks)
% md = means of the R, G and B channels for differences of pairs of coupled
images
% crops = structure containing the cropped images
%
% Version 1.1 - 25/11/2017 (R and G channels implemented)

warning off

a=imread(imagefile);
%aa=mean(double(a),3);
aa=a(:,:,1);
k=find(aa<185);
b=255*ones(size(a,1),size(a,2));
b(k)=0;

%blinding the upper part of the image:
b(1:round(size(b,1)/2),:)=0;

%morphological analysis:
Ibw=logical(b);
stat=regionprops(Ibw,'boundingbox');
for i=1:numel(stat)
    bb(i,:)=stat(i).BoundingBox;
end

%evaluation of areas of detected rectangles:
area=bb(:,3).*bb(:,4);

%sorting and retention of the n biggest rectangles:
[~,ks]=sort(area);
bb=bb(ks,:);
bb=bb(end-n:end-1,:);

[~,kb]=sort(bb(:,1));
bb=bb(kb,:);

for i=1:2:n
    m=min(bb(i:i+1,3:4));
    bb(i,3:4)=m;
    bb(i+1,3:4)=m;
end
```

```
%visualisation:
figure
hold on
imshow(a)
axis off
axis image

for i=1:size(bb,1)
    rectangle('position',bb(i,:),'edgecolor','g','linewidth',2);

text(bb(i,1)+fix(bb(i,3)/2),bb(i,2)+fix(bb(i,4)/2),int2str(i),'HorizontalAl
ignment','center','VerticalAlignment','middle','FontSize',12,'Color','g')

crops(i).image=a(round(bb(i,2)):round(bb(i,2))+round(bb(i,4)),round(bb(i,1)
):round(bb(i,1))+round(bb(i,3)),:);
end

%computation of mean values (for the R, G and B channels) of differences
between paired images:
meandiffR=[];
meandiffG=[];
meandiffB=[];
for i=1:2:size(bb,1)-1
        diffR=crops(i).image(:,:,1)-crops(i+1).image(:,:,1);    %difference
between paired images for the RED channel
    meandiffR=[meandiffR;mean(mean(diffR))]; %mean computation
        diffG=crops(i).image(:,:,2)-crops(i+1).image(:,:,2);    %difference
between paired images for the GREEN channel
    meandiffG=[meandiffG;mean(mean(diffG))]; %mean computation
        diffB=crops(i).image(:,:,3)-crops(i+1).image(:,:,3);    %difference
between paired images for the BLUE channel
    meandiffB=[meandiffB;mean(mean(diffB))]; %mean computation
end

meandiff=[meandiffR meandiffG meandiffB];


disp(' ')
disp('Mean values of differences between paired images for R, G and B
channels')
disp('From left to right:')
disp(' ')
disp(['n.' '    ' 'R' '         ' 'G' '         ' 'B'])

for i=1:size(meandiff,1)
    disp([int2str(i) ') ' num2str(meandiff(i,:))])
end

disp(' ')

warning on
```

Table 2-1. Design matrix and the responses for central composite design (CCD). The following is a list of the codes used to describe the relevant parameters:
A: Diameter of inlet area (cm)
B: Area of sensing zone (cm^2)
C: Diameter of indicator area (cm)
D: Area of channel (cm^2)
E, F, G: Volumes of sample, methyl orange, and phosphate buffer (μL)
Response: Difference of blue color intensity between respective sample and a blank

Run order	A	B	C	D	E	F	G	Response (ΔB)
1	-1	1	-1	-1	-1	-1	-1	10.46
2	-1	-1	-1	-1	-1	-1	1	13.29
3	1	1	-1	1	1	1	-1	13.54
4	-1	-1	1	-1	1	1	-1	21.44
5	1	1	-1	-1	-1	1	-1	30.37
6	-1	1	1	-1	1	1	1	32.85
7	-1	1	1	1	-1	1	1	8.87
8	-1	-1	-1	1	1	-1	1	12.33
9	1	1	1	-1	1	-1	1	13.04
10	0	0	0	0	0	0	0	27.54
11	1	1	1	1	-1	-1	1	6.4
12	1	-1	1	1	-1	-1	-1	7.1
13	1	-1	-1	-1	-1	1	1	9.08
14	-1	1	-1	1	1	-1	-1	13.4
15	0	0	0	0	0	0	0	28.25
16	1	-1	-1	1	1	1	1	8.51
17	1	-1	1	-1	1	-1	-1	17.89
18	-1	-1	1	1	-1	1	-1	3.86
19	0	0	0	1	0	0	0	25.4
20	0	0	0	0	0	0	0	31.71
21	0	0	0	0	0	-1	0	25.58
22	1	0	0	0	0	0	0	27.04
23	0	0	0	0	0	0	1	26.35
24	0	-1	0	0	0	0	0	17.78
25	0	0	0	0	0	1	0	29.11
26	0	0	0	0	0	0	0	28.25
27	0	0	0	0	0	0	-1	29.61

28	0	0	1	0	0	0	0	17.25
29	0	0	0	0	1	0	0	29.33
30	0	1	0	0	0	0	0	27.31
31	0	0	-1	0	0	0	0	28.94
32	-1	0	0	0	0	0	0	29.66
33	0	0	0	0	-1	0	0	24.98
34	0	0	0	0	0	0	0	26.34
35	0	0	0	-1	0	0	0	30.95
36	0	0	0	0	0	0	0	29.32
37	-1	1	1	1	1	-1	1	16.16
38	1	1	-1	1	-1	-1	-1	8.85
39	0	0	0	0	0	0	0	30.8
40	1	-1	1	-1	-1	1	-1	14.15
41	1	1	1	1	1	1	1	11.72
42	1	1	-1	-1	1	-1	-1	26.74
43	-1	-1	1	-1	-1	-1	-1	11.04
44	1	-1	-1	-1	1	-1	1	19.52
45	1	1	1	-1	-1	1	1	18.46
46	-1	-1	-1	-1	1	1	1	10.33
47	-1	-1	-1	1	-1	1	1	12.55
48	-1	1	-1	1	-1	1	-1	18.9
49	1	-1	1	1	1	1	-1	11.39
50	-1	1	1	-1	-1	-1	1	8.38
51	-1	1	-1	-1	1	1	-1	33.21
52	1	-1	-1	1	-1	-1	1	12.67
53	0	0	0	0	0	0	0	27.15
54	-1	-1	1	1	1	-1	-1	17.93
55	-1	1	-1	1	-1	-1	1	22.54
56	-1	-1	-1	-1	1	-1	-1	22.75
57	1	1	-1	-1	1	1	1	26.36
58	1	-1	-1	1	-1	1	-1	11.35
59	0	0	0	0	0	0	0	27.86
60	-1	-1	1	-1	-1	1	1	6.62
61	1	1	-1	1	-1	1	1	15.73
62	-1	1	1	-1	-1	1	-1	24.26

63	-1	1	1	1	1	1	-1	20.03
64	1	1	1	1	1	-1	-1	9.2
65	1	1	1	-1	-1	-1	-1	12.53
66	-1	-1	-1	1	-1	-1	-1	14.9
67	1	-1	1	-1	-1	-1	1	8.65
68	-1	-1	1	1	1	1	1	16.1
69	0	0	0	0	0	0	0	30.68
70	1	-1	1	1	1	-1	1	11.78
71	-1	1	-1	-1	1	-1	1	32.37
72	1	-1	-1	-1	1	1	-1	13.59
73	1	-1	1	1	-1	1	1	11.08
74	-1	-1	1	1	-1	-1	1	8.12
75	-1	1	-1	-1	-1	1	1	31.14
76	1	1	1	1	-1	1	-1	6.37
77	1	-1	-1	-1	-1	-1	-1	13.83
78	-1	1	1	1	-1	-1	-1	7.73
79	-1	-1	1	-1	1	-1	1	14.11
80	1	-1	-1	1	1	-1	-1	13.12
81	0	0	0	0	0	0	0	30.16
82	-1	1	-1	1	1	1	1	29.5
83	1	1	-1	1	1	-1	1	28.66
84	-1	-1	-1	-1	-1	1	-1	19.07
85	0	0	0	0	0	0	0	33.24
86	1	-1	1	-1	1	1	1	8.86
87	1	1	-1	-1	-1	-1	1	32.06
88	1	1	1	-1	1	1	-1	30.74
89	-1	1	1	-1	1	-1	-1	15.18
90	-1	-1	-1	1	1	1	-1	24.32

Table 2-2. Design matrix and the responses for Box-Behnken design (BBD). The following is a list of the codes used to describe the relevant parameters:
A: Diameter of inlet area (cm)
B: Area of sensing zone (cm^2)
C: Diameter of indicator area (cm)
D: Area of channel (cm^2)
E, F, G: Volumes of sample, methyl orange, and phosphate buffer (μL)
Response: Difference of blue color intensity between respective sample and a blank

Run order	A	B	C	D	E	F	G	Response (ΔB)
1	0	1	0	0	-1	0	1	24.47
2	0	0	0	1	1	-1	0	26.82
3	1	0	0	0	0	1	-1	29.91
4	0	0	0	-1	1	1	0	31.49
5	0	0	0	1	-1	1	0	19.84
6	0	-1	1	0	0	1	0	11.69
7	-1	0	-1	0	-1	0	0	29.13
8	0	0	-1	-1	0	0	-1	27.92
9	1	0	1	0	-1	0	0	9.62
10	0	0	-1	1	0	0	1	27.42
11	-1	-1	0	-1	0	0	0	19.5
12	0	-1	0	0	1	0	1	14.58
13	0	0	0	0	0	0	0	27.79
14	1	0	0	0	0	-1	1	23.57
15	-1	0	0	0	0	-1	-1	30.37
16	-1	1	0	1	0	0	0	28.9
17	1	-1	0	1	0	0	0	14.45
18	0	0	0	0	0	0	0	28.7
19	0	1	1	0	0	-1	0	16.5
20	0	-1	0	0	-1	0	-1	20.49
21	0	0	1	1	0	0	-1	19.35
22	1	1	0	-1	0	0	0	31.23
23	0	1	-1	0	0	1	0	30.13
24	0	0	1	-1	0	0	1	19.95
25	0	0	0	-1	-1	-1	0	29.85
26	0	-1	-1	0	0	-1	0	16.77
27	-1	0	0	0	0	1	1	27.44

28	1	0	-1	0	1	0	0	31.3
29	0	0	0	0	0	0	0	29.05
30	-1	0	1	0	1	0	0	18.54
31	0	1	0	0	1	0	-1	31.14
32	0	0	1	1	0	0	1	12.72
33	0	0	0	-1	1	-1	0	27.57
34	0	0	0	1	1	1	0	30.4
35	0	0	0	1	-1	-1	0	18.87
36	-1	-1	0	1	0	0	0	16.95
37	0	-1	1	0	0	-1	0	9.55
38	0	-1	0	0	-1	0	1	11.61
39	0	-1	-1	0	0	1	0	17.95
40	-1	1	0	-1	0	0	0	33.3
41	1	0	0	0	0	1	1	25.38
42	0	0	0	0	0	0	0	27.72
43	1	1	0	1	0	0	0	19.08
44	0	1	1	0	0	1	0	17.89
45	0	1	0	0	1	0	1	28.74
46	1	0	0	0	0	-1	-1	26.04
47	0	1	0	0	-1	0	-1	28.82
48	0	0	1	-1	0	0	-1	23.84
49	-1	0	1	0	-1	0	0	18.77
50	0	0	-1	1	0	0	-1	28.62
51	0	0	-1	-1	0	0	1	31.65
52	1	0	1	0	1	0	0	21.23
53	-1	0	0	0	0	1	-1	37.92
54	-1	0	-1	0	1	0	0	30.77
55	-1	0	0	0	0	-1	1	22.37
56	0	0	0	0	0	0	0	28.87
57	1	-1	0	-1	0	0	0	20.76
58	0	0	0	-1	-1	1	0	28.94
59	0	-1	0	0	1	0	-1	18.58
60	0	1	-1	0	0	-1	0	26.53
61	1	0	-1	0	-1	0	0	30.89
62	0	0	0	0	0	0	0	27.35

Table 2-3. Design matrix and the responses for D-optimal design (Dopt). The following is a list of the codes used to describe the relevant parameters:
A: Diameter of inlet area (cm)
B: Area of sensing zone (cm^2)
C: Diameter of indicator area (cm)
D: Area of channel (cm^2)
E, F, G: Volumes of sample, methyl orange, and phosphate buffer (μL)
Response: Difference of blue color intensity between respective sample and a blank

Run order	A	B	C	D	E	F	G	Response (ΔB)
1	0	0	0	0	0	0	0	31.21
2	-1	-1	-1	-1	-1	-1	-1	18.33
3	1	1	1	0	-1	-1	-1	9.14
4	-1	1	-1	1	-1	-1	-1	32.43
5	1	1	0	-1	0	-1	-1	27.91
6	0	-1	1	1	0	-1	-1	7.37
7	-1	0	1	-1	1	-1	-1	25.83
8	1	0	-1	1	1	-1	-1	29.49
9	-1	-1	1	1	-1	0	-1	11.77
10	-1	0	-1	0	0	0	-1	32.39
11	0	1	-1	-1	1	0	-1	33.53
12	-1	1	1	-1	-1	1	-1	32.00
13	-1	0	0	0	-1	1	-1	36.66
14	1	-1	-1	1	-1	1	-1	15.97
15	1	-1	1	-1	1	1	-1	18.85
16	-1	-1	-1	1	1	1	-1	21.40
17	0	1	1	1	1	1	-1	20.33
18	0	1	1	-1	-1	-1	0	21.06
19	1	0	1	1	-1	-1	0	2.500
20	0	-1	0	0	1	-1	0	16.54
21	-1	-1	0	-1	1	0	0	20.97
22	-1	1	1	0	1	0	0	17.71
23	1	1	-1	-1	-1	1	0	34.63
24	-1	-1	1	-1	0	1	0	16.32
25	1	-1	1	1	1	1	0	12.55
26	1	1	-1	-1	-1	-1	1	31.55
27	-1	-1	1	-1	-1	-1	1	10.36

28	1	-1	-1	1	-1	-1	1	11.93
29	-1	1	-1	-1	1	-1	1	23.75
30	1	-1	1	-1	1	-1	1	13.96
31	-1	-1	-1	1	1	-1	1	15.17
32	1	1	1	1	1	-1	1	15.32
33	0	0	0	-1	-1	0	1	25.86
34	-1	1	-1	-1	-1	1	1	36.39
35	1	-1	1	-1	-1	1	1	12.26
36	-1	-1	-1	1	-1	1	1	14.03
37	1	1	-1	1	-1	1	1	23.35
38	-1	1	1	1	-1	1	1	13.49
39	1	-1	-1	-1	1	1	1	22.76
40	1	1	1	-1	1	1	1	26.31
41	-1	1	-1	1	1	1	1	33.23
42	-1	-1	1	1	1	1	1	7.53
43	1	1	1	1	1	1	1	12.74
44	0	0	0	0	0	0	0	26.13

Chapter 3

Table 3-1. Design matrix and the responses for Box-Behnken design (BBD). The following is a list of the codes used to describe the geometry relevant parameters:
A: Channel length (mm) of the device
B: Channel width (mm) of the device
C: Area length (mm) of the device
D: Area width (mm) of the device
E: Sampling volume (µL)
Response: Difference of blue color intensity between respective sample and a blank

Run order	A	B	C	D	E	Response (ΔB)
1	0.0	0.0	0.0	0.0	0.0	36.1
2	-1.0	-1.0	0.0	0.0	0.0	28.9
3	1.0	-1.0	0.0	0.0	0.0	25.0
4	-1.0	1.0	0.0	0.0	0.0	45.2
5	1.0	1.0	0.0	0.0	0.0	28.2
6	0.0	0.0	-1.0	-1.0	0.0	30.1
7	0.0	0.0	1.0	-1.0	0.0	36.3
8	0.0	0.0	-1.0	1.0	0.0	34.4
9	0.0	0.0	1.0	1.0	0.0	39.0
10	0.0	-1.0	0.0	0.0	-1.0	20.2
11	0.0	1.0	0.0	0.0	-1.0	24.3
12	0.0	0.0	0.0	0.0	0.0	33.6
13	0.0	-1.0	0.0	0.0	1.0	31.2
14	0.0	1.0	0.0	0.0	1.0	40.5
15	-1.0	0.0	-1.0	0.0	0.0	35.1
16	1.0	0.0	-1.0	0.0	0.0	28.9
17	-1.0	0.0	1.0	0.0	0.0	41.8
18	1.0	0.0	1.0	0.0	0.0	31.2
19	0.0	0.0	0.0	-1.0	-1.0	22.3
20	0.0	0.0	0.0	1.0	-1.0	23.1
21	0.0	0.0	0.0	-1.0	1.0	35.2
22	0.0	0.0	0.0	1.0	1.0	37.7
23	0.0	0.0	0.0	0.0	0.0	34.5
24	0.0	0.0	0.0	0.0	0.0	33.6

25	0.0	-1.0	-1.0	0.0	0.0	28.4
26	0.0	1.0	-1.0	0.0	0.0	33.2
27	0.0	-1.0	1.0	0.0	0.0	26.1
28	0.0	1.0	1.0	0.0	0.0	37.9
29	-1.0	0.0	0.0	-1.0	0.0	38.1
30	1.0	0.0	0.0	-1.0	0.0	30.0
31	-1.0	0.0	0.0	1.0	0.0	37.3
32	1.0	0.0	0.0	1.0	0.0	32.0
33	0.0	0.0	-1.0	0.0	-1.0	21.9
34	0.0	0.0	1.0	0.0	-1.0	22.8
35	0.0	0.0	0.0	0.0	0.0	34.0
36	0.0	0.0	-1.0	0.0	1.0	36.2
37	0.0	0.0	1.0	0.0	1.0	43.0
38	-1.0	0.0	0.0	0.0	-1.0	27.1
39	1.0	0.0	0.0	0.0	-1.0	25.2
40	-1.0	0.0	0.0	0.0	1.0	47.3
41	1.0	0.0	0.0	0.0	1.0	34.4
42	0.0	-1.0	0.0	-1.0	0.0	25.2
43	0.0	1.0	0.0	-1.0	0.0	33.0
44	0.0	-1.0	0.0	1.0	0.0	27.1
45	0.0	1.0	0.0	1.0	0.0	38.2
46	0.0	0.0	0.0	0.0	0.0	33.3

Table 3-2. Design matrix and the responses for Box-Behnken design (BBD). The following is a list of the codes used to describe the assay reagent relevant parameters:
A: Printing cycles of PVA
B: Printing cycles of NaOH
C: Printing cycles of NH_3
D: Printing cycles of $AgNO_3$
Response: Difference of blue color intensity between respective sample and a blank

Run order	A	B	C	D	Response (ΔB)
1	-1.0	-1.0	0.0	0.0	26.3
2	1.0	-1.0	0.0	0.0	36.1
3	-1.0	1.0	0.0	0.0	28.6
4	1.0	1.0	0.0	0.0	27.3
5	0.0	0.0	0.0	0.0	32.1
6	0.0	0.0	-1.0	-1.0	16.1
7	0.0	0.0	1.0	-1.0	20.2
8	0.0	0.0	-1.0	1.0	31.8
9	0.0	0.0	1.0	1.0	39.3
10	-1.0	0.0	0.0	-1.0	24.2
11	1.0	0.0	0.0	-1.0	16.9
12	-1.0	0.0	0.0	1.0	25.1
13	1.0	0.0	0.0	1.0	55.8
14	0.0	0.0	0.0	0.0	33.2
15	0.0	-1.0	-1.0	0.0	28.0
16	0.0	1.0	-1.0	0.0	26.5
17	0.0	-1.0	1.0	0.0	30.6
18	0.0	1.0	1.0	0.0	28.3
19	-1.0	0.0	-1.0	0.0	26.5
20	1.0	0.0	-1.0	0.0	19.4
21	-1.0	0.0	1.0	0.0	19.1
22	1.0	0.0	1.0	0.0	37.0
23	0.0	0.0	0.0	0.0	32.0
24	0.0	-1.0	0.0	-1.0	20.7
25	0.0	1.0	0.0	-1.0	10.6
26	0.0	-1.0	0.0	1.0	32.0
27	0.0	1.0	0.0	1.0	30.2

Chapter 4

Developed script for rectangle detection of isoniazid device:

```
function [meandiff,crops]=sqdetect_one(imagefile,n)

% [md,crops] = sqdetect_one('imagefile.jpg',n);
%
% n = number of rectangles to be detected (samples + blanks)
% md = means of the R, G and B channels for differences of pairs of coupled
images
% crops = structure containing the cropped images
%
% Version 1.1 - 25/11/2017 (R and G channels implemented)
%

warning off

a=imread(imagefile);
%aa=mean(double(a),3);
%aa=double(a(:,:,2))./double(a(:,:,3));
aa=sum(double(a),3);
k=find(aa<150);
b=255*ones(size(a,1),size(a,2));
b(k)=0;

%blinding the upper part of the image:
b(1:round(size(b,1)/2),:)=0;

%morphological analysis:
Ibw=logical(b);
stat=regionprops(Ibw,'boundingbox');
for i=1:numel(stat)
    bb(i,:)=stat(i).BoundingBox;
end

%evaluation of areas of detected rectangles:
area=bb(:,3).*bb(:,4);

%sorting and retention of the n biggest rectangles:
[~,ks]=sort(area);
bb=bb(ks,:);
bb=bb(end-n:end-1,:);

[~,kb]=sort(bb(:,1));
bb=bb(kb,:);

% for i=1:2:n
%     m=min(bb(i:i+1,3:4));
%     bb(i,3:4)=m;
%     bb(i+1,3:4)=m;
% end

m=min(bb(1:n,3:4));
for i=1:n
bb(i,3:4)=m;
end
```

```
%visualisation:
figure
hold on
imshow(a)
axis off
axis image

for i=1:2
    rectangle('position',bb(i,:),'edgecolor','r','linewidth',2);
    text(bb(i,1)+fix(bb(i,3)/2),bb(i,2)+fix(bb(i,4)/2),['B'
int2str(i)],'HorizontalAlignment','center','VerticalAlignment','middle','Fo
ntSize',12,'Color','r')

crops(i).image=a(round(bb(i,2)):round(bb(i,2))+round(bb(i,4)),round(bb(i,1)
):round(bb(i,1))+round(bb(i,3)),:);
end
for i=3:size(bb,1)
    rectangle('position',bb(i,:),'edgecolor','g','linewidth',2);
    text(bb(i,1)+fix(bb(i,3)/2),bb(i,2)+fix(bb(i,4)/2),int2str(i-
2),'HorizontalAlignment','center','VerticalAlignment','middle','FontSize',1
2,'Color','g')

crops(i).image=a(round(bb(i,2)):round(bb(i,2))+round(bb(i,4)),round(bb(i,1)
):round(bb(i,1))+round(bb(i,3)),:);
end

%computation of mean values of blanks:

W=(crops(1).image+crops(1).image(2))/2;


%computation of mean values (for the R, G and B channels) after blanks
subctraction:

meandiffR=[];
meandiffG=[];
meandiffB=[];
for i=3:size(bb,1)
        diffR=W(:,:,1)-crops(i).image(:,:,1);  %difference between paired
images for the RED channel
    meandiffR=[meandiffR;mean(mean(diffR))]; %mean computation
        diffG=W(:,:,2)-crops(i).image(:,:,2);  %difference between paired
images for the GREEN channel
    meandiffG=[meandiffG;mean(mean(diffG))]; %mean computation
        diffB=W(:,:,3)-crops(i).image(:,:,3);  %difference between paired
images for the BLUE channel
    meandiffB=[meandiffB;mean(mean(diffB))]; %mean computation
end

meandiff=[meandiffR meandiffG meandiffB];


disp(' ')
disp('Mean values of differences between paired images for R, G and B
channels')
disp('From left to right:')
disp(' ')
disp(['n.' '    ' 'R' '         ' 'G' '         ' 'B'])
```

```
for i=1:size(meandiff,1)
    disp([int2str(i) ') ' num2str(meandiff(i,:))])
end

disp(' ')

warning on
```

Table 4-1. Design matrix and the responses for central composite design (CCD). The following is a list of the codes used to describe the relevant parameters:
A: Area length (mm) of the device
B: Area width (mm) of the device
C: Sampling volume (μL)
D, E, F: Printing cycles of assay reagents PVA, NH_4OH, and $AgNO_3$
Response: Difference of blue color intensity between respective sample and a blank

Run order	A	B	C	D	E	F	Response (ΔB)
1	2.4	0	0	0	0	0	95.7
2	1	-1	-1	-1	-1	1	89.4
3	-1	1	1	-1	1	1	104.9
4	0	0	0	-2.33	0	0	75.5
5	-1	-1	1	-1	-1	1	150.7
6	-1	1	1	1	1	-1	73.5
7	1	1	-1	-1	1	1	115.4
8	1	1	1	-1	-1	1	136
9	0	-2.4	0	0	0	0	109.7
10	1	-1	-1	1	-1	-1	55.2
11	-1	1	-1	1	-1	-1	55.6
12	1	1	-1	1	-1	1	80
13	0	0	0	0	0	2.33	137.8
14	1	-1	1	1	-1	1	132
15	-1	1	1	1	-1	1	130.3
16	1	1	1	1	-1	-1	88.7
17	0	2.4	0	0	0	0	90.3
18	1	-1	-1	-1	1	-1	80.4
19	-1	1	-1	1	1	1	129.6
20	1	1	-1	1	1	-1	87.3
21	-1	-1	1	-1	1	-1	95.7
22	-1	-1	-1	1	1	-1	93.3
23	-1	1	1	-1	-1	-1	69.6
24	0	0	0	0	2.33	0	107.6
25	0	0	-2.4	0	0	0	110.1
26	1	-1	-1	1	1	1	87.5
27	-1	1	-1	-1	-1	1	83.4

28	-1	1	-1	-1	1	-1	86.9
29	0	0	0	0	-2.33	0	70.2
30	1	-1	1	1	1	-1	88.3
31	1	-1	1	-1	-1	-1	62.5
32	0	0	2.4	0	0	0	161.7
33	0	0	0	0	0	-2.33	22.1
34	-1	-1	-1	-1	-1	-1	77.7
35	1	1	-1	-1	1	-1	73.2
36	-1	-1	-1	-1	1	1	110
37	1	-1	1	-1	1	1	100
38	1	1	1	1	1	1	156.2
39	-1	-1	-1	1	-1	1	111.1
40	0	0	0	2.33	0	0	122.6
41	-1	-1	1	1	1	1	165
42	1	1	1	-1	1	-1	107.3
43	-2.4	0	0	0	0	0	122.3
44	-1	-1	1	1	-1	-1	91.4
45	0	0	0	0	0	0	113.4
46	0	0	0	0	0	0	110.8

Achievement list

Published original papers related to this thesis:

(1) **Vahid Hamedpour**, Geert J. Postma, Edwin van den Heuvel, Jeroen J. Jansen, Koji Suzuki and Daniel Citterio, Chemometrics-assisted microfluidic paper-based analytical device for the determination of uric acid by silver nanoparticle plasmon resonance, Analytical and bioanalytical chemistry, **2018**, 410:2305-2313.

(2) **Vahid Hamedpour**, Riccardo Leardi, Koji Suzuki and Daniel Citterio, Fabrication of paper-based analytical devices optimized by central composite design, Analyst, **2018,** 143:2102-2108.

Other publications:

(1) Mohammad Amjadi, Jamshid Manzoori, **Vahid Hamedpour**, Optimized Ultrasound-Assisted Temperature-Controlled Ionic Liquid Microextraction Coupled with FAAS for Determination of Tin in Canned Foods. Food Analytical Methods, **2013**, 6:1657–1664.

(2) **Vahid Hamedpour**, Mohammad Amjadi, Application of Box–Behnken Design in the Optimization of In Situ Surfactant-Based Solid Phase Extraction Method for Spectrophotometric Determination of Quinoline Yellow in Food and Water Samples. Food Analytical Methods, **2014**, 7:1123–1129.

Presentations:

(1) **Vahid Hamedpour**, Koji Suzuki, Daniel Citterio, Chemometrics Assisted Microfluidic Paper-Based Analytical Device for the Determination of Uric Acid by Silver Nanoparticles Plasmon Resonance, poster presentation, Royal Society of Chemistry Tokyo International Conference **2016**, September 8-9, Makuhari Messe, Chiba, Japan.

(2) **Vahid Hamedpour**, Koji Suzuki, Daniel Citterio, Chemometrics Assisted Microfluidic Paper-Based Analytical Device for the Determination of Uric Acid by Silver Nanoparticles Plasmon Resonance, Poster presentation, 65th Annual Meeting of the Japan Society for Analytical Chemistry **2016**, September 14-16, Hokkaido University, Sapporo, Japan.

(3) **Vahid Hamedpour**, Koji Suzuki, Daniel Citterio, A central composite design optimized microfluidic paper-based analytical device for the determination of isoniazid by in-situ formed silver nanoparticles plasmon resonance, Oral presentation, The 13th Asian Conference on Analytical Sciences (ASIANALYSIS XIII) **2016**, December 8-11, Chiang Mai University, Chiang Mai, Thailand.

(4) **Vahid Hamedpour**, Koji Suzuki, Daniel Citterio, Microfluidic paper-based analytical device for the determination of uric acid and isoniazid by silver nanoparticles plasmon resonance, Poster presentation, XIX EUROANALYSIS **2017**, 28 August 28- 1 September, Stockholm University, Sweden.

(5) **Vahid Hamedpour**, Koji Suzuki, Daniel Citterio, Application of chemometrics to paper-based colorimetric devices for the determination of isoniazid and uric acid, Royal Society of Chemistry Tokyo International Conference **2017**, September 7-8, Makuhari Messe, Chiba, Japan.

Awards:

(1) Japanese Government scholarship (Monbukagakushu, 文部科学省奨学金), September 2015-September 2018.

(2) **Vahid Hamedpour**, Koji Suzuki, Daniel Citterio, Microfluidic paper-based analytical device for the determination of uric acid and isoniazid by silver nanoparticles plasmon resonance, Poster presentation, XIX EUROANALYSIS **2017**, August 28-1 September, Stockholm University, Sweden (Poster award).

(3) **Vahid Hamedpour**, Geert J. Postma, Edwin van den Heuvel, Jeroen J. Jansen, Koji Suzuki and Daniel Citterio, Chemometrics-assisted microfluidic paper-based analytical device for the determination of uric acid by silver nanoparticle plasmon resonance, Analytical and bioanalytical chemistry, **2018** 410:2305-2313 (Paper in Forefront).

Acknowledgements

First and foremost, I would like to express my deepest gratitude to my supervisor Prof. Daniel Citterio for motivating me to carry out research in this field with his inspiring lectures. He always showed me the right way, reviewed countless revisions carefully and more importantly taught me how to perform research. This thesis would not have been possible without his valuable guidance.

I would also like to express my great gratitude to my thesis committee, Prof. Seimei Shiratori, Prof. Takaki Ishigure, and Prof. Hideo Suzuki for their precious reviews. Also, I gratefully acknowledge Prof. koji Suzuki as a co-supervisor, and Prof. Yuki Hiruta for their kind support and encouragement.

I wishe to thank Prof. Lutgarde Buydens, Prof. Riccardo Leardi, Prof. Paolo Oliveri, Prof. Edwin van den Heuvel, Dr. Jeroen Jonson, and Dr. Geert Postma for giving me the opportunity to be a member of their groups, being always open to teach me chemometrics and involving me in other interesting activities.

I would like to acknowledge a research scholarship from the Ministry of Education, Culture, Sports, Science, and Technology (MEXT, 文部科学省奨学金), Japan.

I am grateful to Dr. Med. Ursula Nagel for her help with isoniazid tablets. I would also like to express my heartfelt appreciation to my labmates for their help and cooperation. They have given me tons of support, encouragement, and patience. I would not be able to do all of this without them during my PhD course.

No words are enough to describe my love and gratitude to my family for their understanding and continued support during my research life. I'm deeply grateful to my father, mother and brother for trusting me and believing in my success. It is not possible to express my feeling for them adequately.